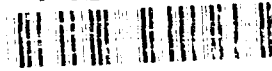


AD-A237 425



REPORT R89-957707

**EXPERIMENTAL AND ANALYTICAL STUDY OF
RIPPLED TRAILING EDGE AIRFOILS FOR
COMPRESSOR APPLICATION**

**Bruce L. Morin and Thomas J. Barber
United Technologies Research Center**

May 1991

**Final Report
Contract N00014-86-C-0663**

**Prepared for
Department of the Navy
Office of Naval Research
Arlington, CA 2217-5000**

**Naval Postgraduate School
Monterey, CA 93942-5100**

Approved for public release; distribution is unlimited

Approved for public release; distribution is unlimited

91-04516



***Experimental and Analytical Study of Rippled Trailing
Edge Airfoils for Compressor Application***

TABLE OF CONTENTS

	<u>Page</u>
SUMMARY	i
ACKNOWLEDGEMENTS	iii
LIST OF FIGURES	iv
NOMENCLATURE	vi
INTRODUCTION	1
EXPERIMENTAL DESCRIPTION	4
<i>Wind Tunnel Description</i>	<i>4</i>
Model Description	7
Experimental Procedure	14
ANALYSIS DESCRIPTION	18
RESULTS AND DISCUSSION	22
High Loading Configuration	22
Low Loading Configurations	45
SUMMARY OF RESULTS	74
CONCLUDING REMARKS	76
RECOMMENDATIONS	78
REFERENCES	79
APPENDIX A	A-1

SUMMARY

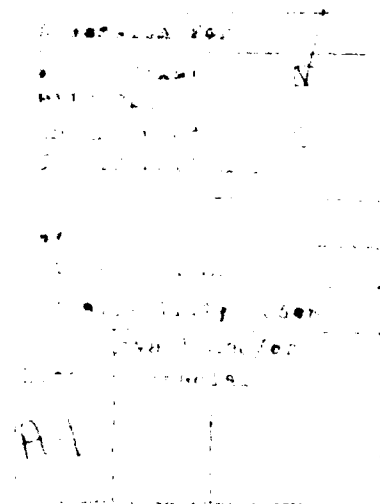
A research program was conducted to assess the potential benefits of using the Rippled Trailing Edge (RTE) concept on compressor airfoils for separation alleviation and wake mixing enhancement. An empirically designed Rippled Trailing Edge (RTE) was tested in a highly loaded, simulated compressor cascade that had demonstrated large scale suction side separation with a baseline circular trailing edge. The original RTE design resulted in a 50% increase of the chordwise extent of the separated flow compared to the baseline trailing edge. Extensive modifications to the RTE resulted in a fairing that eliminated separation, indicating that Rippled Trailing Edges have potential for separation alleviation on compressor trailing edges. However, the failure of the first design shows the weaknesses of the empirical RTE design procedure that was employed, and that many unknowns still exist regarding the three-dimensional boundary layer relief concept. Further testing of ripples on more basic, isolated airfoils is suggested in order to develop further understanding of the three-dimensional boundary layer relief mechanism, without having to consider the inherent problems associated with the cascade testing described herein. After developing such a data base, Rippled Trailing Edges can then be evaluated for application to the more complex case of a cascade where curvature and three-dimensional effects are significant.

Regarding wake mixing enhancement for a lower loading condition less radical trailing edge ripples were employed. These designs consisted of cutting grooves of varying depth and angle into the baseline circular trailing edge. Grooving the trailing edge of the simulated compressor airfoil eliminated vortex shedding and increased base pressure recovery. As a result, losses were reduced compared to the baseline circular trailing edge. Downstream wake surveys showed that the grooved trailing edge created a smaller wake defect out to seven trailing edge diameters from the airfoil. However, farther downstream, where the next blade row would be located, the grooved trailing edge demonstrated a larger wake defect (though smaller wake width), and slower mixing than the circular trailing edge. This effect was attributed to the thick trailing edge boundary layers which are a characteristic of current technology compressor airfoils. Since the objective was to reduce rotor/stator interaction by reducing the wake defect, the conclusion is that trailing edge grooves are not effective for application to current technology compressor airfoils. However, for thinner boundary layer

applications (or likewise thicker trailing edges), the grooved trailing edges showed enhanced wake mixing beyond 11 trailing edge diameters downstream of the airfoil, in addition to a significant reduction in mixing loss.

ACKNOWLEDGEMENTS

The authors wish to acknowledge Michael J. Worle (UTC), and Robert W. Paterson (UTRC) for formulating this research program. Appreciation is also expressed to William P. Patrick (UTRC) for supervision of the experimental portion of the program. The authors also want to thank Duane C. McCormick (UTRC), Walter M. Presz (Western New England College), Stanley A. Skebe (UTRC), and Robert H. Schlinker (UTRC) for helpful discussions during the course of the program, and also for review of the final report. Finally, the authors want to thank Joseph E. Bibisi, Francis J. Boser, and Richard C. Adamonis, all from UTRC, for their assistance in conducting the experiments.



R89-957707

LIST OF FIGURES

- Figure 1. The Rippled Trailing Edge Concept
- Figure 2. Wind Tunnel Arrangement
- Figure 3. Overall View of Loaded Trailing Edge Experiment
- Figure 4. Simulated Cascade Geometry
- Figure 5. Schematic of Curved Plate Controlled Diffusion Airfoil Cascade Simulation
- Figure 6. Approximate Streamline Patterns Observed in Reference [3]
- Figure 7. RTE Cross Sections
- Figure 8. RTE End View Showing Instrumentation Locations
- Figure 9. Low Loading Trailing Edge Configurations
- Figure 10. Four View Projection of RTE Spanwise Segment
- Figure 11. Coarse Mesh Model of RTE Lobe Surface
- Figure 12. Comparison of Present Baseline to Results of Reference [3]
- Figure 13. Surface Flow Visualization of Baseline Trailing Edge
- Figure 14. RTE Pressure Distributions Compared to Baseline – Section A-A
- Figure 15. RTE Pressure Distributions Compared to Baseline – Section B-B
- Figure 16. Surface Flow Visualization of RTE
- Figure 17. Wind Tunnel Blockage Effect Due to Change in Wake Convection Angle
- Figure 18. Modifications Performed to Obtain RTE 2
- Figure 19. Surface Flow Visualization of RTE 2
- Figure 20. Comparison Between RTE Configurations
- Figure 21. RTE 2 Pressure Distribution Compared to Baseline – Section A-A
- Figure 22. Model of Baseline High Loaded Vane/Wind Tunnel Using VSAERO
- Figure 23. VSAERO Predicted Surface Pressure Loading Compared to High Loaded Vane Data
- Figure 24. Model of Symmetric Unloaded Vane with RTE in Wind Tunnel Using VSAERO
- Figure 25. VSAERO Predicted Surface Pressure Loading for Unloaded Vane with RTE

- Figure 26. Model of High Loaded Vane With RTE/Wind Tunnel Using VSAERO
- Figure 27. VSAERO Predicted Surface Pressure Loading for High Loaded Vane With RTE
- Figure 28. VSAERO Predicted Loading Contours for High Loaded Vane With RTE
- Figure 29. Model 2 Pressure Distribution Compared to Baseline
- Figure 30. Model 3 Pressure Distribution Compared to Baseline
- Figure 31. Model 4 Pressure Distribution Compared to Baseline
- Figure 32. Hot Film Spectra Downstream of Model 1 and Model 2
- Figure 33. Total Pressure Profiles Downstream of Model 1
- Figure 34. Total Pressure Profiles Downstream of Model 2
- Figure 35. Total Pressure Profiles Downstream of Model 3
- Figure 36. Total Pressure Profiles Downstream of Model 4
- Figure 37. Velocity Profiles Downstream of Model 1
- Figure 38. Velocity Profiles Downstream of Model 2
- Figure 39. Velocity Profiles Downstream of Model 3
- Figure 40. Velocity Profiles Downstream of Model 4
- Figure 41. Average Total Pressure Profiles at $x'/t = 11.25$
- Figure 42. Average Velocity Profiles at $x'/t = 11.25$
- Figure 43. Boundary Layer Profiles Approaching Trailing Edge
- Figure 44. Total Pressure Distributions Downstream of Model 1
- Figure 45. Total Pressure Distributions Downstream of Model 2
- Figure 46. Comparison of Wake Decay
- Figure 47. Boundary Layer Profiles Approaching Trailing Edge With Flat Plate Removed
- Figure 48. Downstream Total Pressure Distributions - Thin Boundary Layers
- Figure 49. Comparison of Wake Decay - Thin Boundary Layer

NOMENCLATURE

C_p	Pressure Coefficient
H	Suction side stream tube height
L	Axial chord length
P	Static pressure
P_t	Total pressure
Q	Dynamic pressure
t	Baseline trailing edge diameter
V	Total Velocity
x	Coordinate axis measured axially from leading edge
x'	Coordinate axis measured from trailing edge along metal angle
y	Transverse coordinate axis perpendicular to x
y'	Transverse coordinate axis perpendicular to x'
z	Coordinate axis measured spanwise from airfoil centerline
α	Lobe inclination from mean camber line
β	Wake Convection Angle
δ^*	Displacement Thickness
ϕ	Cascade mean turning angle
θ	Momentum Thickness

Subscripts

b	Base
e	Cascade exit condition
p	Pressure side
s	Suction side
ref	Upstream reference conditions
min	Minimum

INTRODUCTION

State of the art controlled diffusion airfoils are designed with thick trailing edges in order to reduce airfoil suction side diffusion and hence minimize the possibility of full boundary layer separation prior to the trailing edge (Reference [1]). Preventing separation from occurring upstream of the trailing edge maximizes cascade turning and minimizes profile losses; however, the thick trailing edges which are required introduce a performance penalty known as base drag. At design point operation, extreme surface curvature at the trailing edge causes a high diffusion rate which results in local separation (References [2], [3] and [4]). This local separation reduces the static pressure behind the trailing edge thereby increasing the mixing loss. Under higher loading conditions, typical of off-design operation, the separation point can move several trailing edge thicknesses upstream along the suction side (References [2] and [3]). This large scale separation results in a loss of cascade turning which significantly reduces airfoil loading. In addition, the resulting large viscous wake interacts with subsequent blade rows to produce unsteady loading, which reduces durability and increases noise. At design point operation, the wake is much smaller compared to that of the fully separated airfoil (References [2] and [3]), but it still persists to the next blade row.

Several techniques for eliminating separation by energizing the boundary layer have been attempted in the past including axial vortex generators and secondary air injection (see References [5], [6], [7], and [8]). The present research effort employed a novel concept, that of using three-dimensional boundary layer relief near the airfoil trailing edge to locally reduce the adverse pressure gradient imposed on the suction side boundary layer. This concept, known as the Rippled Trailing Edge (RTE), is shown on an isolated airfoil in Figure 1. In Reference [9], the RTE surface contouring is said to set up a lateral pressure gradient that drives the boundary layer fluid toward a clashing line between the peak and trough of the ripples. This three-dimensional boundary layer relief alleviates the strong streamwise pressure gradient, thereby producing an attached flow to the airfoil trailing edge. Results from Reference [9] have shown that "through the use of controlled lateral surface contouring, one can provide a mechanism for alleviation of boundary layer separation effects and thereby produce aerodynamic shapes that yield higher maximum lift and/or lower drag at high lift".

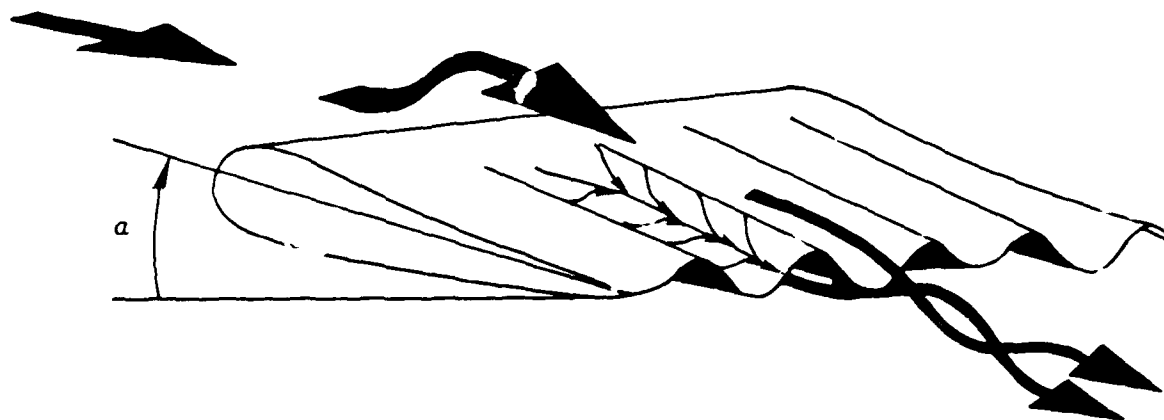


Figure 1. The Rippled Trailing Edge (RTE) Concept

Convolutd surfaces, such as those on an RTE, are also very effective from a mixing viewpoint. Convolutd surfaces (mixers) have long been used in turbofan engines to rapidly mix the fan and engine streams to create a nearly uniform velocity profile at the engine exhaust. Paterson has shown in Reference [10] that such lobed mixers generate large scale streamwise vortices which control the rate of mixing within a turbofan nozzle. These stirring vortices are set up by the inviscid pressure field created by the convolutions. Paterson observed that the mixing rate downstream of mixers is significantly greater than that developed by the small scale turbulent eddy interactions which emanate from a straight trailing edge. Similar results are described in Reference [11]. As a result of those studies, three-dimensional contouring is being examined in the present effort as a means of increasing the mixing rate in the wake region of a compressor airfoil.

A combined experimental/analytical approach was undertaken for this research effort. Experimentally, a simulated compressor cascade study, similar to that of McCormick et al. in References [2] and [3], was performed. In that experiment, a benchmark study of the flow field in the vicinity of a simulated circular compressor trailing edge with local separation at the trailing edge (low loading configuration), and with intermittent full boundary layer separation prior to the trailing edge (high loading configuration) was conducted. The objective of the present study was to apply the RTE concept to eliminate the separation described in References [2] and [3] for the high loading configuration, in addition to enhancing wake mixing for the low loading configuration.

Analytically, a three-dimensional singularity superposition method was constructed to simulate the compressor cascade studied in the experimental phase of this program. The inviscid "panel" method predicts the surface pressure distribution over the airfoil surface. A boundary layer analysis is then used to analytically examine the tendency of the airfoil to separate.

EXPERIMENTAL DESCRIPTION

Wind Tunnel Description

The experiment was conducted in a closed loop UTRC Boundary Layer Wind Tunnel nearly identical to the one used in a previous cascade simulation described in Reference [3]. A schematic of the tunnel is shown in Figure 2 along with a photograph in Figure 3.

Air was supplied by a centrifugal blower whose flow rate could be changed by means of a vortex valve at the blower inlet, in addition to a variable pulley system to control the blower speed. The blower exhausted into a large settling chamber (see Figure 2) in which a series of partial span baffles, screens, perforated plates, and honeycomb were used to create nearly uniform, swirl-free flow exiting the chamber. The freestream turbulence level of the tunnel is roughly 0.25% of the tunnel freestream velocity. A detailed description of the blower and settling chamber can be found in Reference [12].

Just downstream of the settling chamber, a 2-to-1 contraction accelerated the flow into a 41.7 cm (16.4 in.) high by 78.7 cm (31 in.) wide by 30.5 cm (12 in.) long straight rectangular duct. The combination of the contraction and straight section was designed in Reference [3] to provide uniform flow to the entrance of the test section. The boundary layers on the four walls were tripped with a 0.31 cm (0.125 in.) square bar located approximately 15.2 cm (6 in.) upstream of the test section. The tunnel's reference total pressure, dynamic pressure, and total temperature were measured in this straight section.

The test section is described in detail in Reference [3] and will be discussed only briefly in this report. The test section consisted of a 55.9 cm (22 in.) long straight rectangular duct followed by a variable geometry turning duct. The top and bottom walls of the test section were used to simulate the midgap streamlines (corrected for boundary layer growth) between two compressor blades. Both walls were instrumented with static pressure taps and terminated in the downstream dump. The side walls of the test section were rigid and had Plexiglas windows in the vicinity of the trailing edge for flow visualization purposes. If needed, endwall suction was available in the trailing edge region to obtain two-dimensional flow. After the dump, the flow entered a filter system and heat exchanger and was then ducted back into the blower.

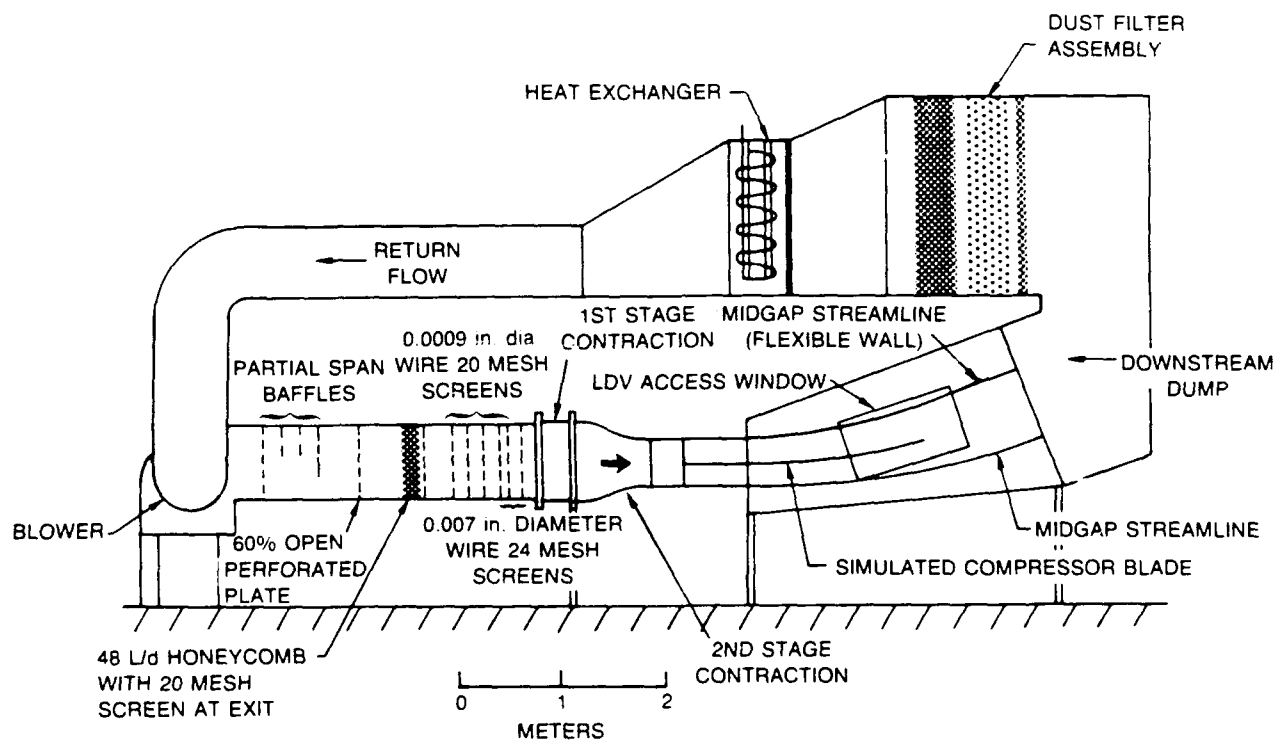


Figure 2. Wind Tunnel Arrangement

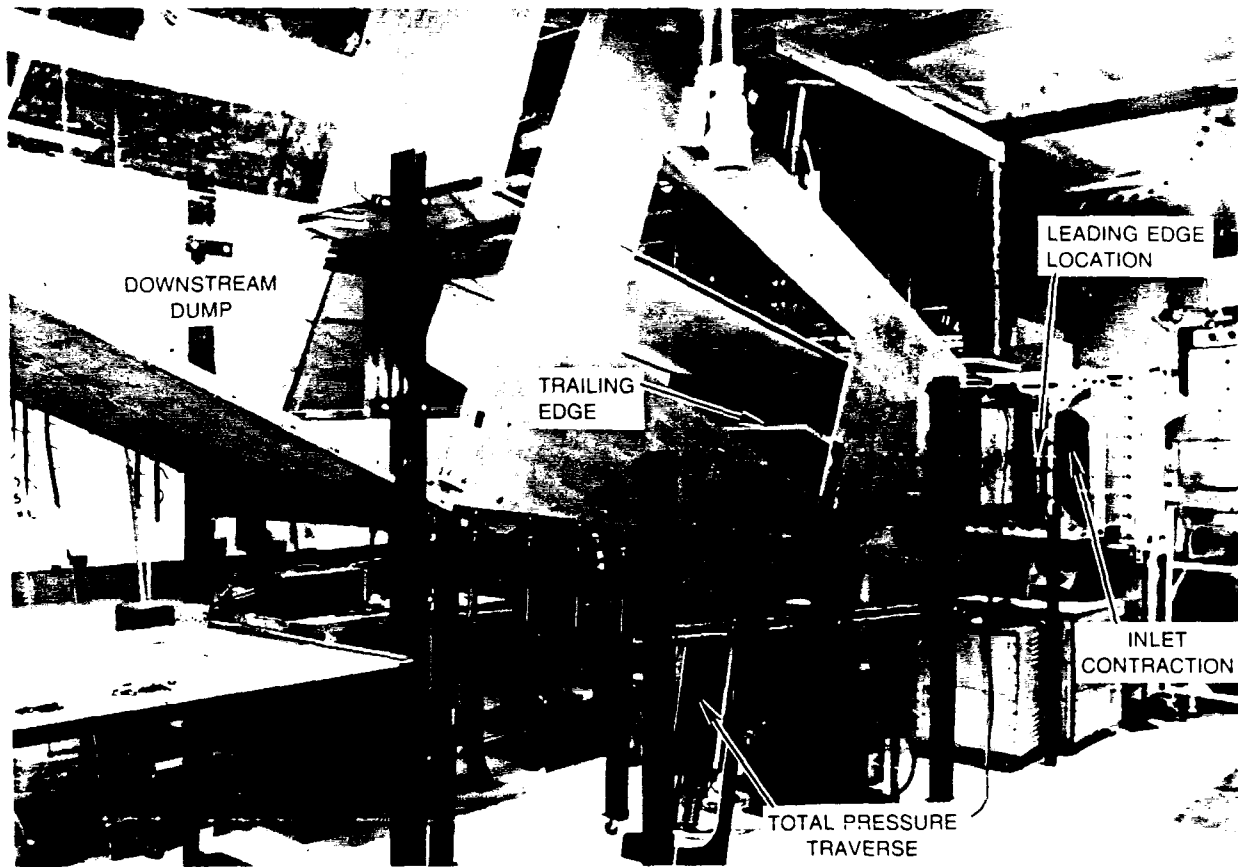


Figure 3. Overall View of Loaded Trailing Edge Experiment

Model Description

The cascade model consisted of two sections: a flat plate that was used to obtain realistic compressor boundary layer characteristics (δ^*/t and θ/t), and a turning section required to simulate loading effects. Both sections were instrumented with static pressure taps on the suction side and pressure side. Figure 4 presents a schematic of the simulated cascade model, and Figure 5 shows the relationship of the original cascade (dashed lines) to the simulated cascade. The method used to design the model geometry and obtain the midgap streamlines is described in detail in Reference [3].

The flat plate, which was constructed of ribbed aluminum with an aluminum skin, was 119 cm (47 in.) long and 2.54 cm (1 in.) thick. The leading edge (a 3-to-1 ellipse) was located at the exit of the 30.5 cm (12 in.) straight section. It was positioned in the middle of the straight part of the test section parallel to the top and bottom walls. Both the pressure side and suction side boundary layers were tripped approximately 15.2 cm (6 in.) downstream of the leading edge with a Hama trip (Reference [13]).

The turning section was composed of several circular arc plates and a trailing edge piece. The 2.54 cm (1 in.) thick turning plates and baseline trailing edge were constructed of ribbed aluminum with aluminum skin. The turning section had a centerline radius of curvature of 175 cm (69 in.), and could be configured to provide turning angles of 20, 30, 34, and 40 degrees. The baseline trailing edge was semi-circular, with a 2.54 cm (1 in.) diameter.

Note that two coordinate systems are shown in Figure 4. The origin of the x, y coordinate system is located at the leading edge of the flat plate, with the x -coordinate being measured parallel to the flat plate section. The origin of the x', y' coordinate system is located at the trailing edge of the model, with the x' -coordinate being measured parallel to the tangent of the metal angle.

Results from Reference [3] showed the 30 degree, high loading configuration to be intermittently separated over a large extent of the suction surface near the trailing edge, while the 20 degree, low loading configuration was separated only near the trailing edge circle. Schematics of the approximate *streamline patterns* observed in that study are shown in Figure 6.

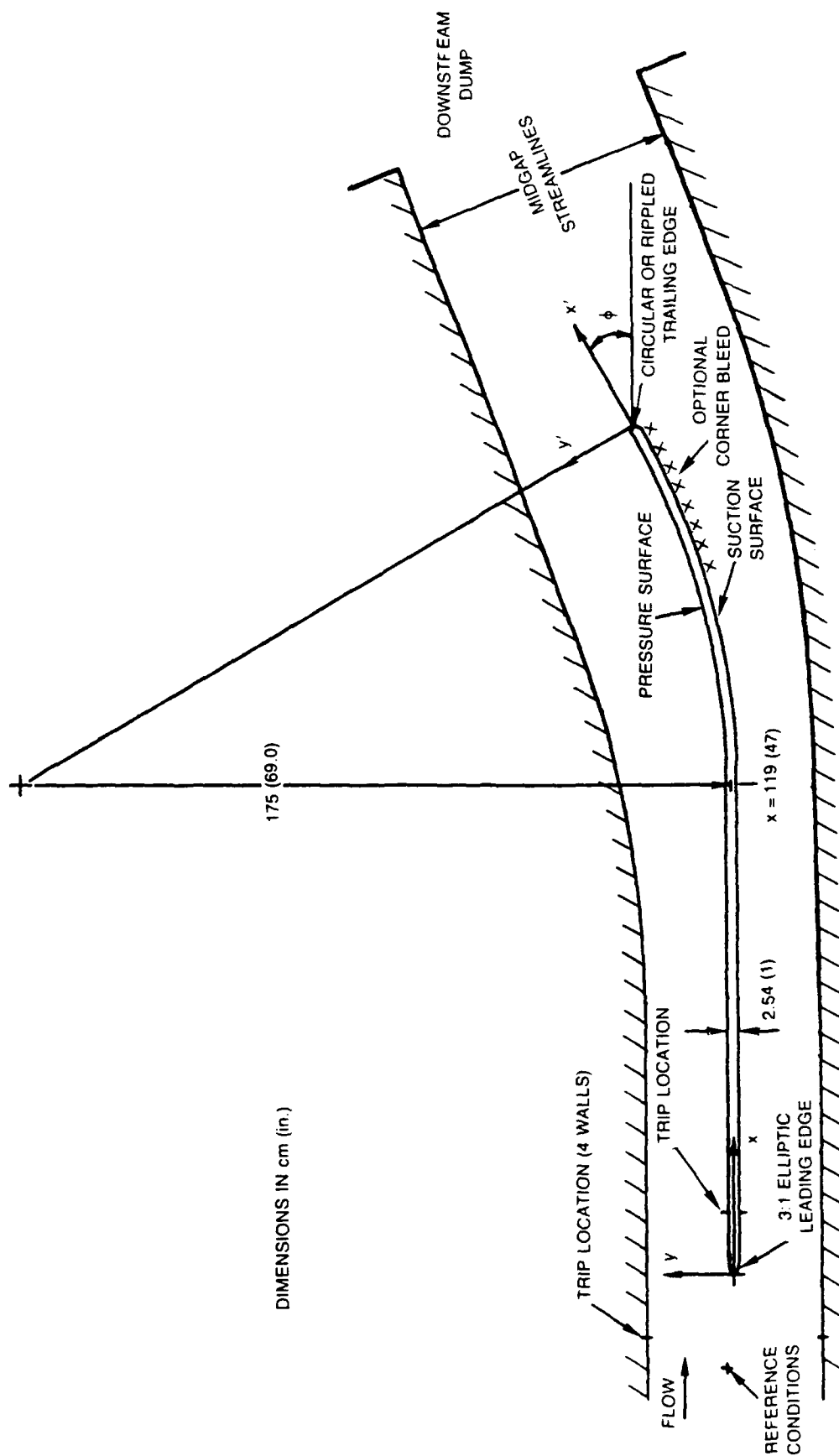


Figure 4. Simulated Cascade Geometry

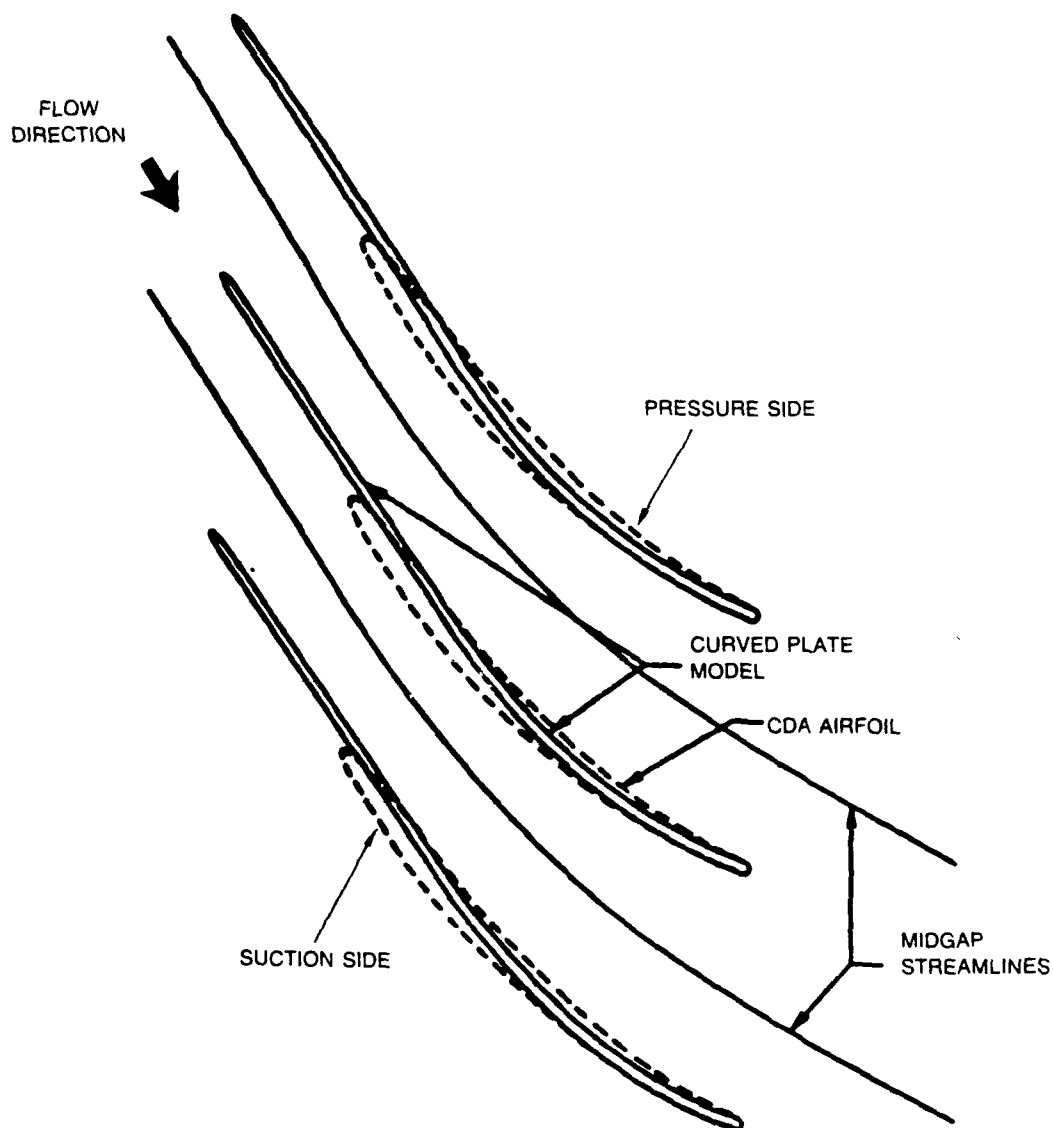


Figure 5. Schematic of Curved Plate Controlled Diffusion Airfoil Cascade Simulation

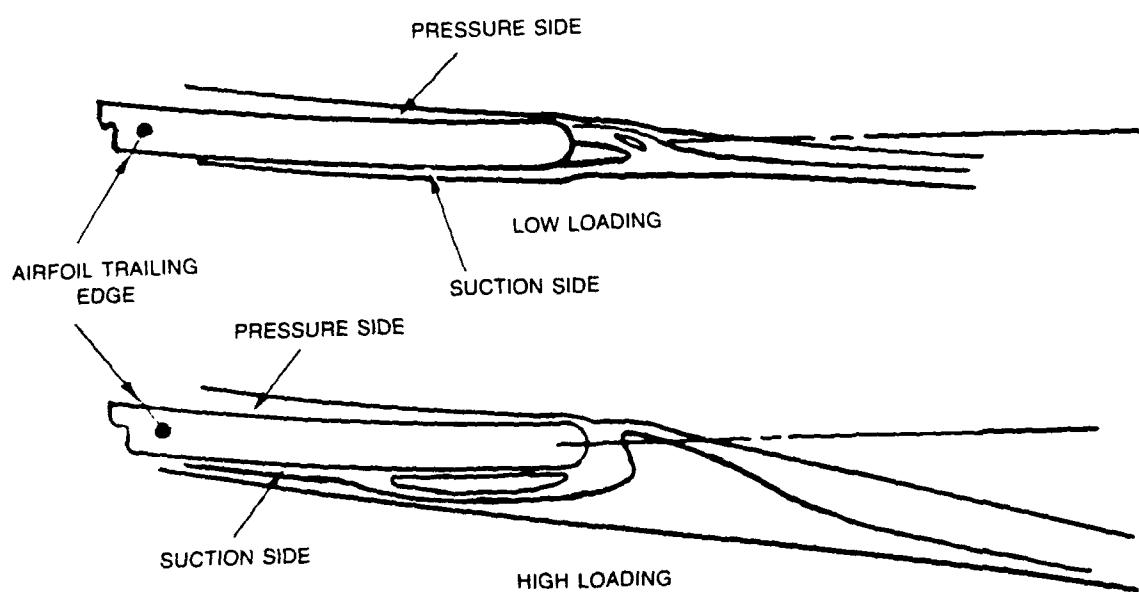


Figure 6. Approximate Streamline Patterns Observed in Reference [3]

In Reference [3], flow detachment on the suction side of the highly loaded, baseline airfoil was observed to occur between 12.7 (5 in.) and 15.2 cm (6 in.) upstream of the trailing edge. It was felt that starting the lobe contour 5.08 cm (2 in.) to 7.62 cm (3 in.) upstream of the separation point would be sufficient to initiate secondary lobe flows to energize the low momentum near surface fluid and thereby prevent separation. Therefore, the starting point of the lobes was chosen to be 20.3 cm (8 in.) upstream of the trailing edge. Cross sections presented in Figure 7 show the details of the RTE development.

Note that the trailing edge of the RTE was nominally 0.16 cm (0.063 in.) thick while the baseline trailing edge was 2.54 cm (1 in.) thick. As a result, the boundary layer integral quantities normalized by trailing edge thickness (δ^*/t and θ/t) are much larger for the RTE configuration. It is believed that this difference is irrelevant since the more important quantities in terms of boundary layer relief are the ratio of the lobe height to the boundary layer displacement thickness, and the ratio of the lobe width to the boundary layer displacement thickness.

The RTE cross sections shown in Figure 7 were derived empirically from previous work with convoluted (rippled) surfaces where they were used for mixing and drag reduction (References [9], [10], [11], [14], [15], [16], [17], and [18]). Unsymmetrical mixers (or ripples) have been shown to provide very efficient mixing in ejectors and turbofan engines, in addition to significant drag reduction on cars and other bluff bodies due to the large scale secondary flows they create. The RTE design was unsymmetrical with a nominal suction side to pressure side lobe width ratio of 2.0 and a pressure side angle, α_p , of 15 degrees (refer to Figure 7). The suction side angle, α_s , was determined by equating the area enclosed by the pressure side penetration below the model centerline to that enclosed by the suction side penetration above the model centerline thereby maintaining the same geometric centerline as the baseline trailing edge. The result of this approach was a suction side angle, α_s , of 10 degrees. The centerline radius of curvature of the RTE was 175 cm (69 in.), the same as that of the baseline trailing edge. Due to its complex geometry, the RTE was constructed of fiberglass molded around an aluminum spar.

Due to the shape of the RTE and its thickness, the RTE was instrumented as shown in Figure 8. The pressure side taps were located on the peak and trough of the second lobe to the left of the

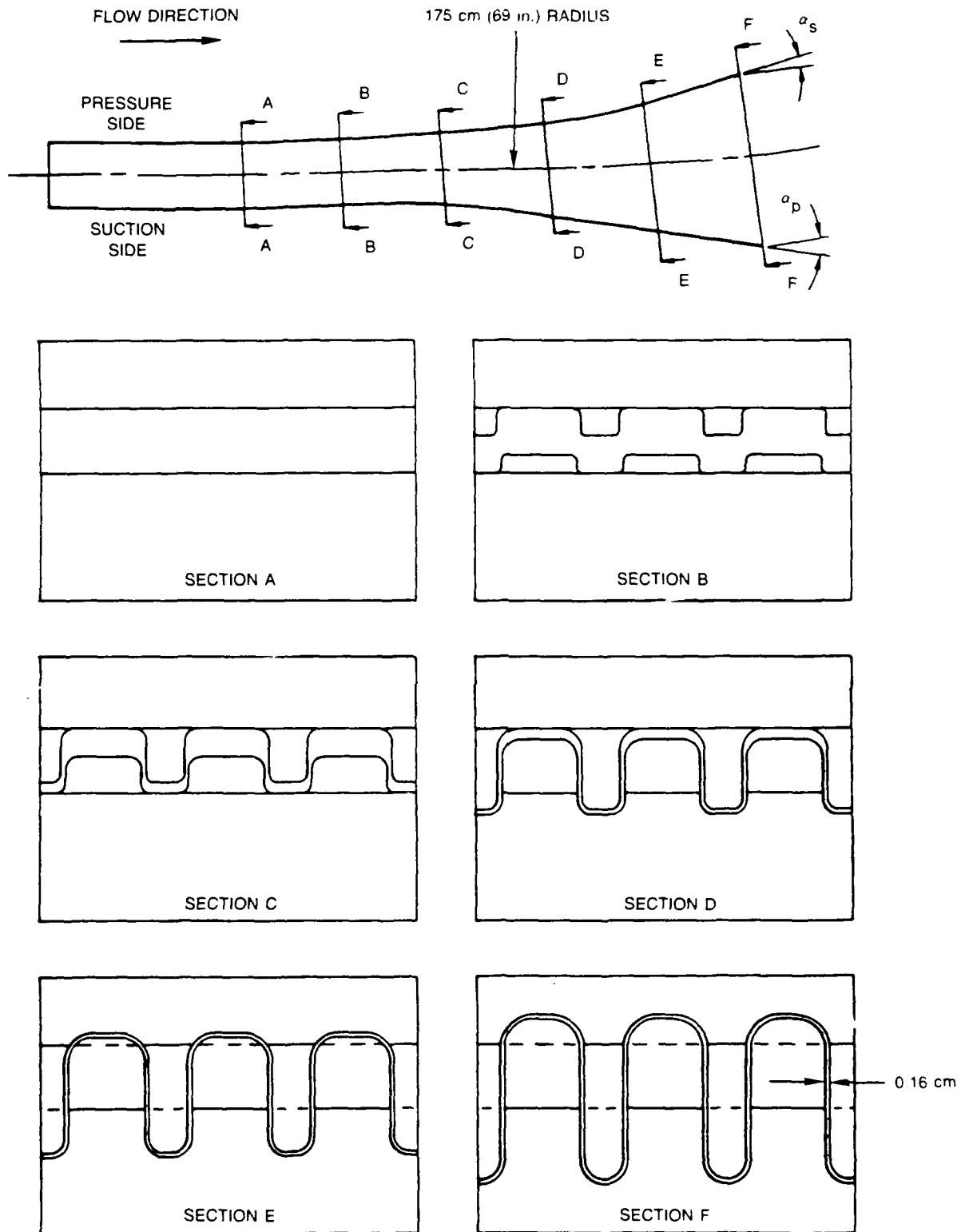


Figure 7. RTE Cross Sections

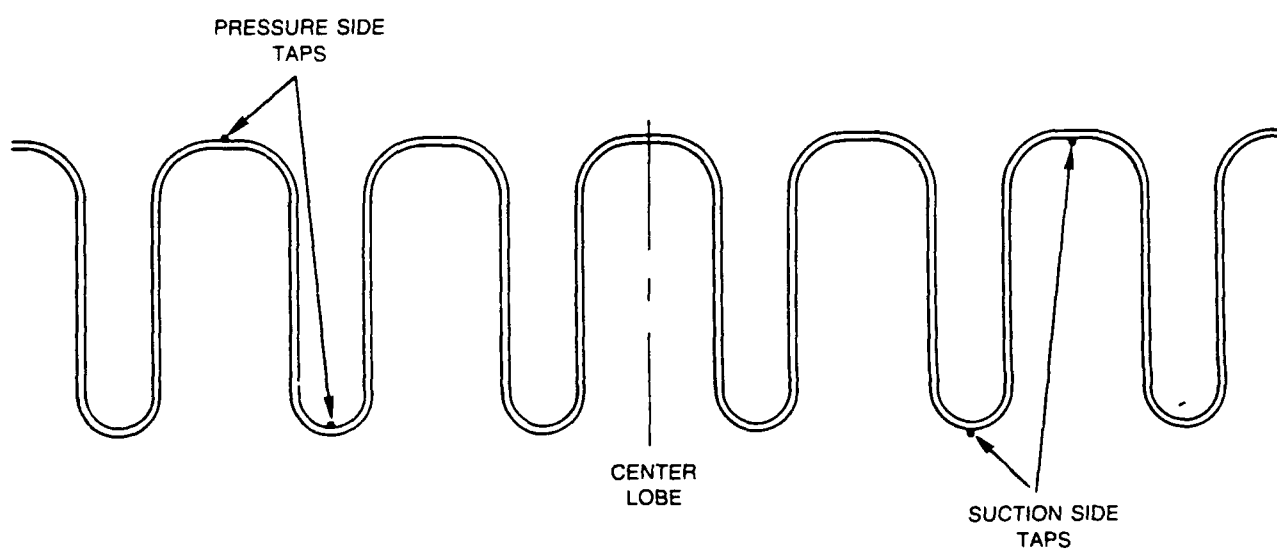


Figure 8. RTE End View Showing Instrumentation Locations

center lobe relative to Figure 8. The suction side peak and trough were instrumented on the second lobe to the right of center. This setup was required because the thickness of the lobes forced the pressure lines to be run along the surface opposite to that on which the measurements were being taken.

Regarding wake mixing for the low loading configuration, less radical rippled trailing edges were employed. These configurations consisted of grooves cut in the trailing edge as shown in Figure 9. Grooving the trailing edge reduces its effective thickness, thus reducing the airfoil's overall loss (see Reference [19]). The postulated advantage of the grooves over an equivalent straight trailing edge is the mixing that occurs from the streamwise vortices created by the trailing edge convolutions. These stirring vortices should mix the wake faster than a two-dimensional shear layer. The postulated result is that at the same distance downstream of the airfoil, the grooved trailing edge will have a smaller wake defect than an equivalent circular straight trailing edge.

Models 1 through 5 were constructed of wood with a 2.54 cm (1 in.) diameter circular trailing edge. Various depth grooves inclined at angles of 20 degrees (Models 2 through 4) and 25 degrees (Model 5) were cut into the circular trailing edges. For manufacturing ease, the mean camber line of these wooden models had no curvature. As a result, the total turning of the low loading configuration was 15.6 degrees compared to 20 degrees in Reference [3]. Models 1 through 4 were instrumented as shown in Figure 9, but Model 5 was not instrumented. Model 1, which was not grooved, was used as the baseline.

Experimental Procedure

For the high loading configurations, surface static pressure distributions and trailing edge surface flow visualization were used to determine if separation had been alleviated. For the low loading configurations, surface static pressure and downstream total pressure distributions were used to evaluate mixing enhancement. Hot film anemometry was used to obtain the characteristics of the boundary layers approaching the trailing edge. During all experiments, the tunnel reference conditions were monitored in the straight duct preceding the test section with a pitot-static pressure probe for measuring the reference dynamic pressure, and a thermocouple for measuring the reference total temperature. The nominal operating conditions were:

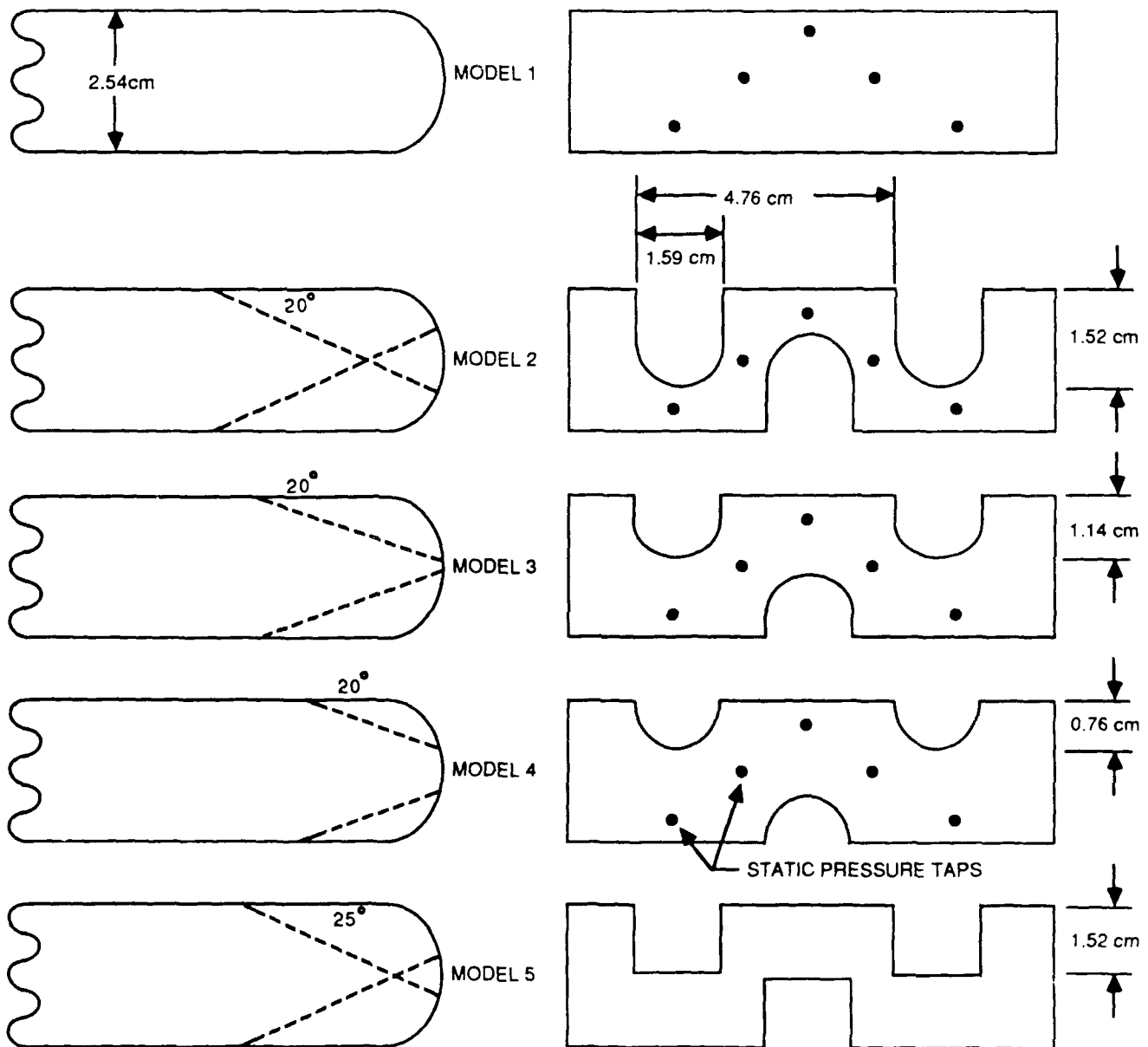


Figure 9. Low Loading Trailing Edge Configurations

Inlet dynamic pressure	3.43 cm (1.35 in.) H ₂ O
Total pressure	12.4 cm (4.9 in.) H ₂ O
Total temperature	32 C (90 F)
Inlet velocity	24 m/s (78.8 ft/s)

The Reynolds number based on the nominal operating conditions and the axial chord length was $2.7(10^6)$ for the low loading configuration, and $3.0(10^6)$ for the high loading configuration.

The surface static pressures were measured with a PSI (Pressure Systems Inc.) Model 780B/T pressure scanner which is a fully integrated pressure measurement device controlled by an IBM PC/AT microcomputer through a single IEEE interface. The pressure range of the sensors was ± 71 cm (28 in.) H₂O differential with an accuracy of approximately ± 0.03 cm (0.01 in.) H₂O differential. The pressure sensors were referenced to the upstream static pressure, P_{ref} , to minimize errors in the calculations of the surface static pressure coefficients.

The downstream total pressure surveys were obtained by traversing a 0.32 cm (0.125 in.) diameter Kiel probe with two Daedal Inc. Model 44000 series linear tables in an x-y arrangement. The tables were controlled remotely through the IEEE interface of an IBM PC/AT minicomputer via a Computomotor Model 3000 closed loop stepping motor controller. A ± 0.98 cm (2.5 in.) H₂O transducer referenced to P_{ref} was used to measure the total pressure sensed by the Kiel probe, and another ± 0.98 cm (2.5 in.) H₂O transducer was used to measure Q_{ref} . The accuracy of both transducers was estimated to be ± 0.013 cm (0.005 in.) H₂O differential. Data from both transducers were acquired through a Data Translation Model DT2805/5716, 16 bit A/D board installed on an IBM PC/AT minicomputer.

The hot film surveys were obtained by traversing a TSI Model 1218-20 boundary layer probe with the y-traverse table described in the previous paragraph. The anemometer that was used was a TSI Model 1050 general purpose unit operating in the constant temperature mode. The time mean bridge voltage was found by the averaging circuit of a TSI Model 1076 meter. The time constant was selected such that there were negligible temporal variations in the output. The output of the averaging circuit was recorded through the A/D board described previously.

Surface flow visualization was obtained using an ammonia/ozalid technique in which either ozalid paper was attached to the surface or ozalid chemical sprayed onto the surface and ammonia then injected into the near surface air stream to develop the ozalid paper or chemical. In regions of stall, ammonia streaks are directed upstream, while in unseparated flow the streaks are directed downstream. This technique was used to define flow field two-dimensionality in addition to trailing edge separation.

ANALYSIS DESCRIPTION

The low speed flow field over a single airfoil or a cascade of airfoils that is operating near its design point is typically not dominated by viscous flow effects and therefore can be determined in terms of solutions to Laplace's equation. Finite difference methodology has been extensively used to generate solutions of this type for simple two-dimensional airfoils and three-dimensional wings. The analysis of complex three-dimensional configurations using finite difference techniques, however, has not been as extensive, primarily due to the difficulty in generating a computational grid over the flow field of interest, while still being body conforming for application of surface boundary conditions. In contrast, "panel" methods, taking advantage of the linearity of the problem, apply Green's third identity to develop a surface singularity superposition technique. In such methodologies, a computational grid covering the flow field of interest is not required. Geometrical features of individual bodies of multi-component bodies can be accounted for by distributing combinations of vortex, source or doublet singularities over all surfaces. The vortex singularity introduces the effect of thickness or blockage. The effective solution at a point is determined by the net effect of these surface singularities at that point.

An analytical model of the RTE airfoil has been made using two panel code methods: a vortex lattice method developed by D. Mook of VPI and the doublet method (VSAERO) developed by AMI [20], [21]. A practical modeling problem is, however, faced in both analyses, when long thin geometries such as the baseline and RTE airfoils are considered. A typical panel representation for the relatively low thickness-to-chord ratio airfoils of interest would require an extremely dense array of surface singularities to avoid solver instabilities arising from ill-conditioning of the "influence coefficient" matrix. The airfoil surface, therefore, has been modeled in terms of vortex or doublet singularities distributed along the mean camber line. Pressure and suction no-flow surface boundary conditions are imposed along the mean camber line, as in slender body theory. For example, the Mook analysis assumes that the lattices are joined by straight line segments and that each segment can be calculated according to the Biot-Savart law. The induced velocity at any point can be obtained by summing the contribution over all segments. The strength or distribution of the vorticity singularities is determined by imposing a solid wall or no-penetration condition at one point in each element and by imposing

the requirement that the divergence of vorticity be zero (spatial conservation of circulation around all segments intersecting a node).

The lifting or flow turning effect of a wing introduces a singular behavior that can be removed by introducing an inviscid wake of shed vorticity; the strength and position of which is determined by convecting the wake along the streamlines of the calculated flow field. The position of the wake is initially assumed known. The distribution of wake vorticity is then calculated by imposing the no-penetration condition along the sheet. A net pressure discontinuity is produced and the wake is iteratively displaced to produce pressure continuity across the wake.

The rippled trailing edge surface of the RTE airfoil has been generated using a geometry preprocessor that uses a combination of straight line and circular arc segments. Given the lobe height, the lobe period and the ratio of crest to trough widths, the surface coordinate generator constructs a discretized surface for the surface singularity placement. The surface of the highly loaded airfoil case (discussed below) is shown in a four view projection in Figure 10. While the program calculates the solution for a single lobe, the spanwise effect is simulated using a periodic boundary condition, as is shown in a coarse mesh representation in Figure 11. The airfoil surface has been divided into three axial segments, over which an increasingly denser spanwise mesh definition will be used.

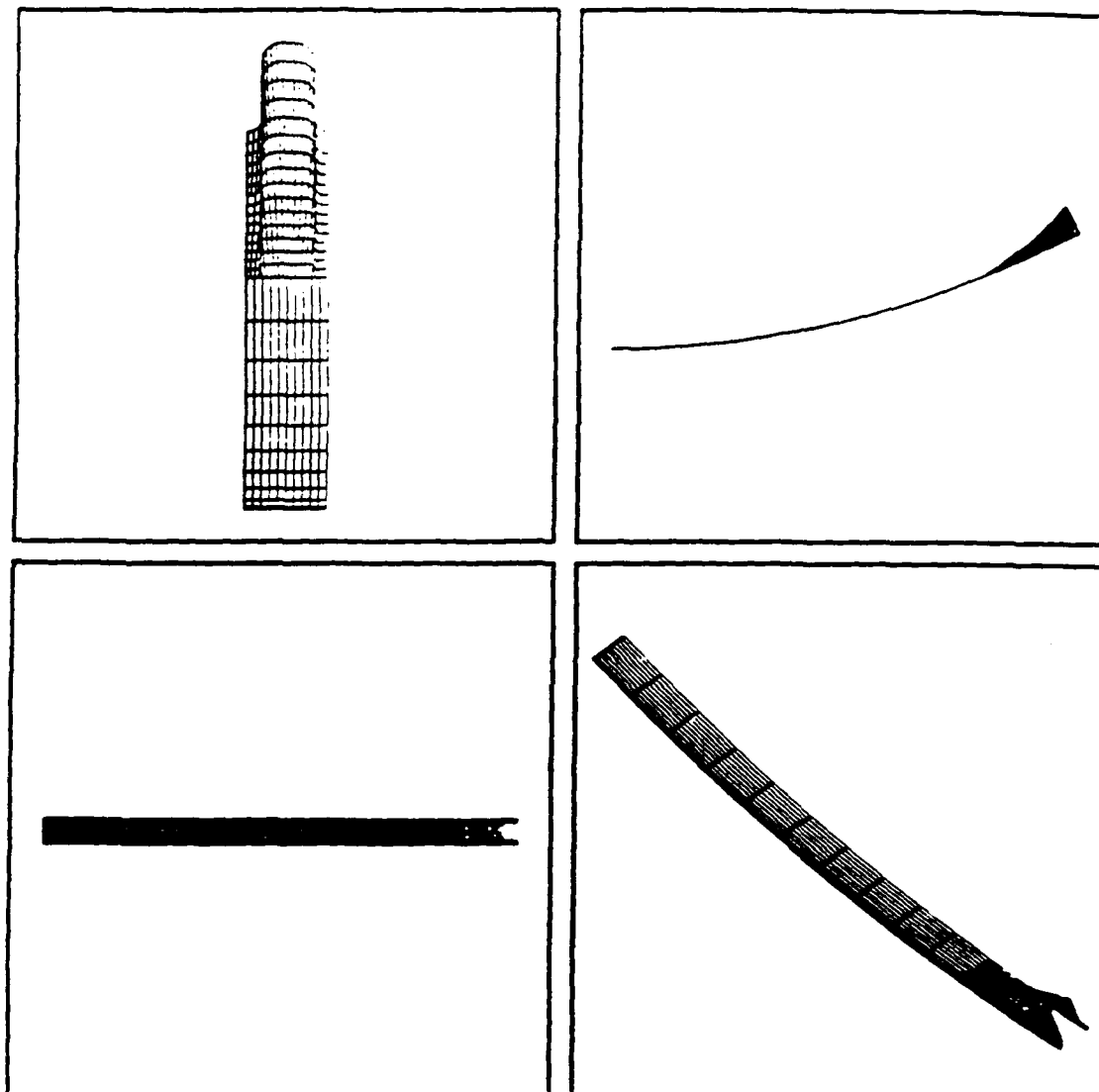


Figure 10. Four View Projection of RTE Spanwise Segment

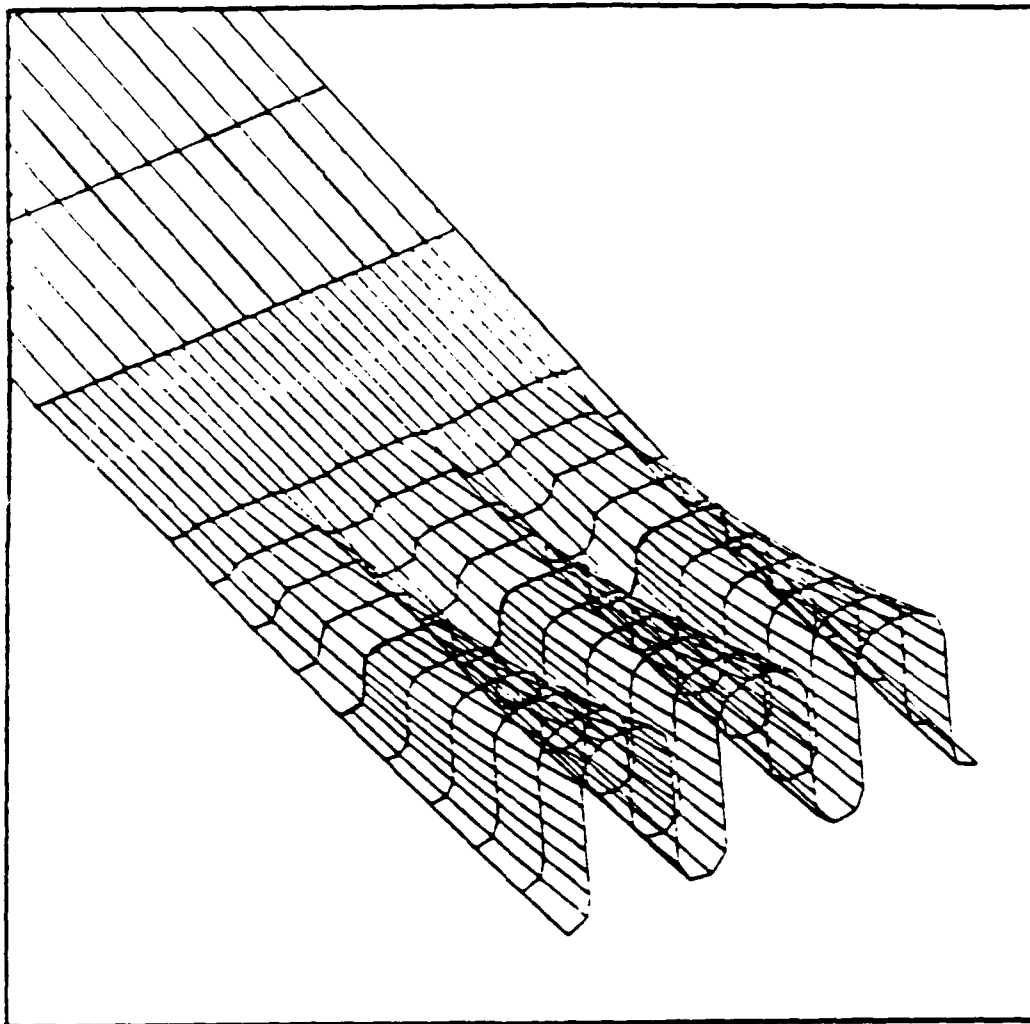


Figure 11. Coarse Mesh Model of RTE Lobe Surface

RESULTS AND DISCUSSION

High Loading Configuration

Baseline Results

Figure 12 compares baseline static pressure distributions obtained in this study to those from Reference [3]. The results are presented as a static pressure coefficient, $(P - P_{ref})/Q_{ref}$ versus axial distance, x/L , measured from the leading edge of the model. Both data sets were obtained with 19.1 cm (7.5 in.) H_2O endwall suction which produced two-dimensional flow over approximately 35% of the tunnel span.

The static pressure distributions obtained in this experiment demonstrate significantly less loading than those of the previous experiment, as indicated by the reduced area between the pressure and suction side curves. In addition, a shorter pressure plateau is observed near the suction side trailing edge of the present baseline suggesting a smaller stall region than in the previous experiment. Surface flow visualization in Figure 13 shows that separation occurred 10.2 cm (4 in.) upstream of the trailing edge compared to 12.7 cm (5 in.) to 15.2 cm (6 in.) upstream of the trailing edge as described in Reference [3]; this result is consistent with the trailing edge pressure distributions.

The discrepancy between the two experiments has been attributed to the inability to exactly match the cascade geometry that was tested in Reference [3]. This is primarily due to the two experiments being performed in different, though similarly designed wind tunnels. Small differences in the midgap streamline positions, the model location relative to the midgap streamlines, and upstream flow uniformity all contributed to the discrepancy.

RTE Results

Figure 14 and 15 compare the model static pressure distributions obtained with the RTE to those obtained with the baseline trailing edge. Section A-A corresponds to the pressure side peak and suction side trough (Figure 14), while section B-B corresponds to the pressure side trough and suction side peak (Figure 15). In both figures, the RTE reduced airfoil loading and increased the length of the pressure plateau on the suction side. Both results suggest that the RTE aggravated suction side

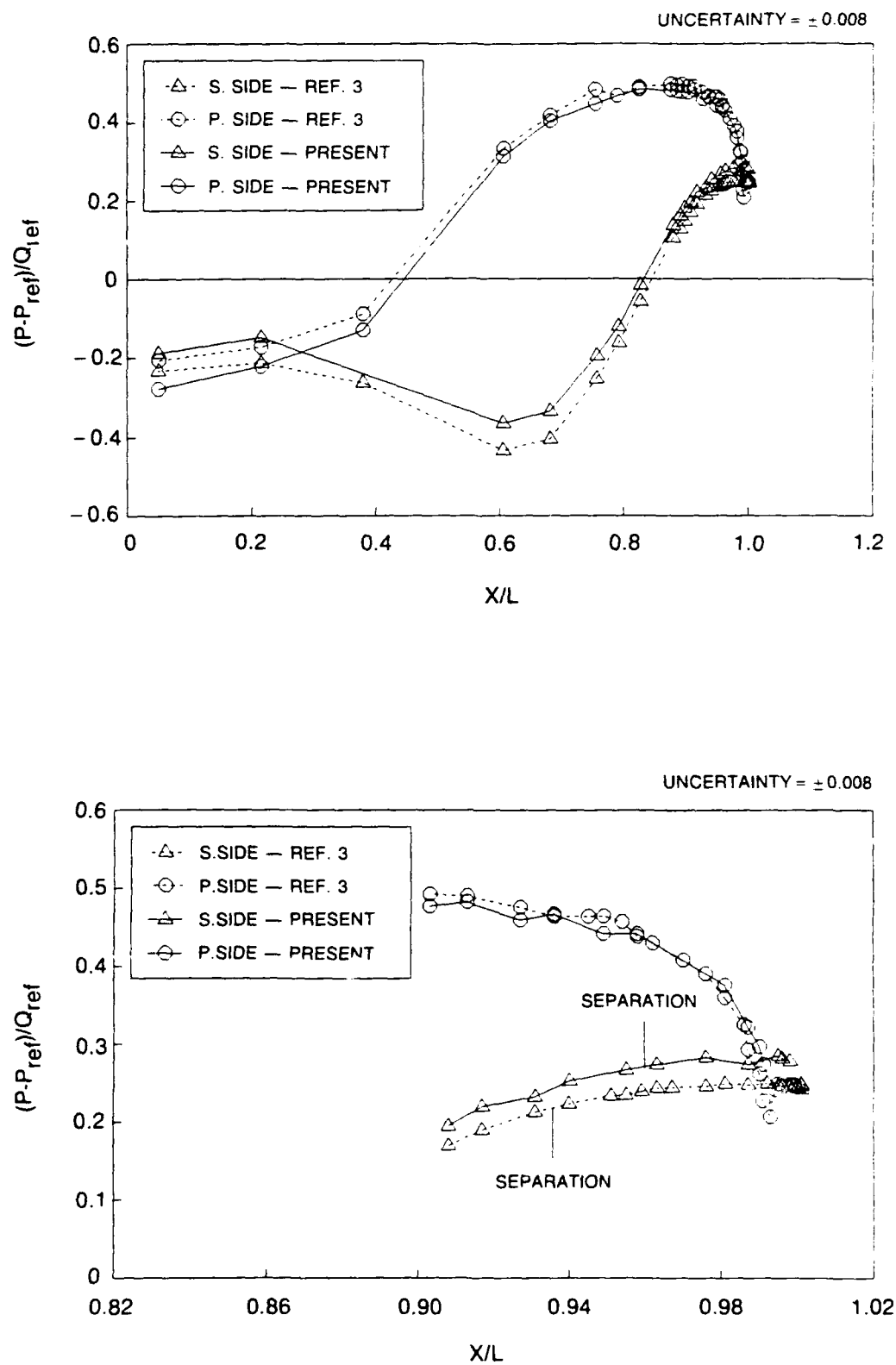


Figure 12. Comparison of Present Baseline to Results of Reference [3]

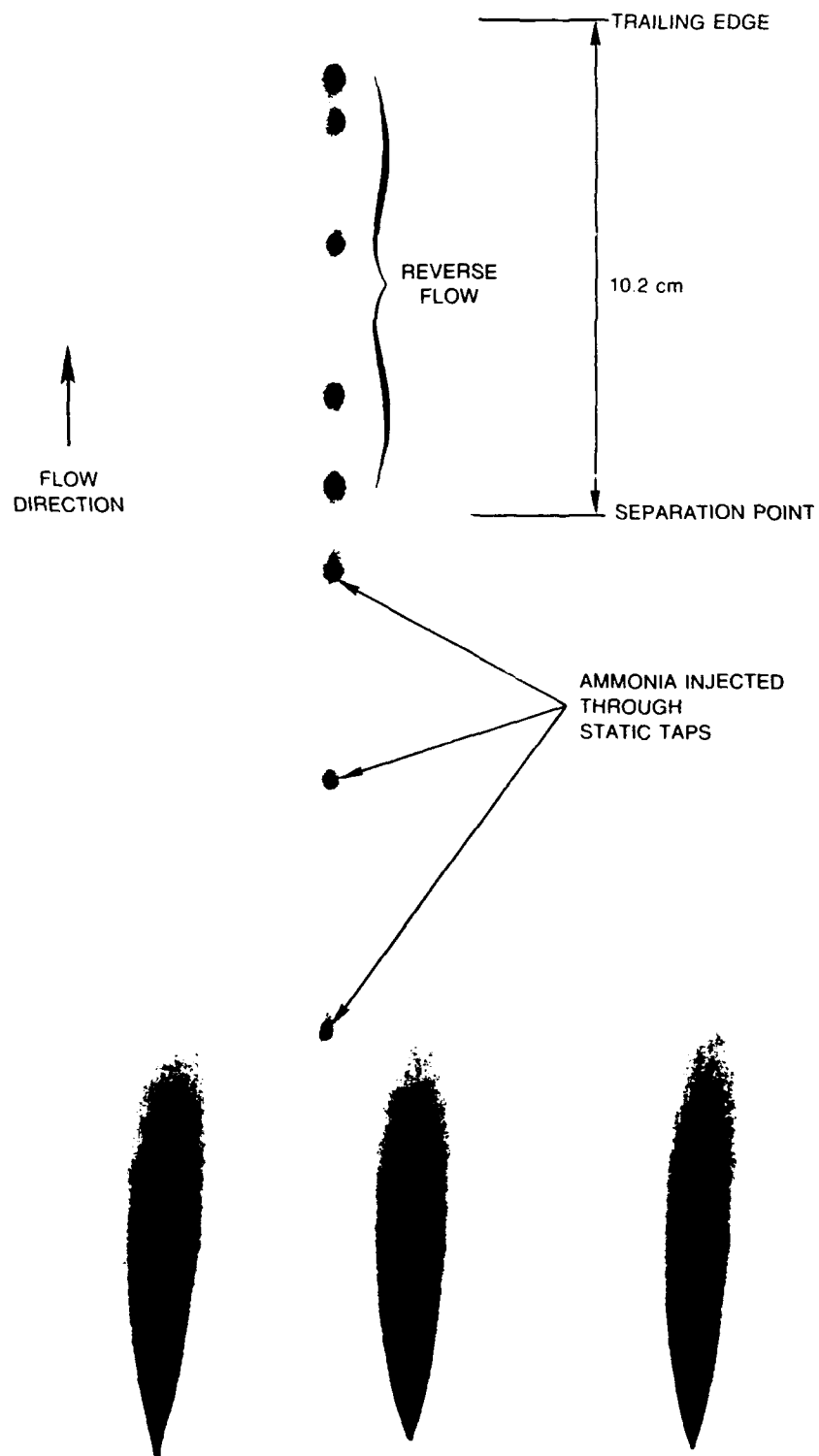


Figure 13. Surface Flow Visualization of Baseline Trailing Edge

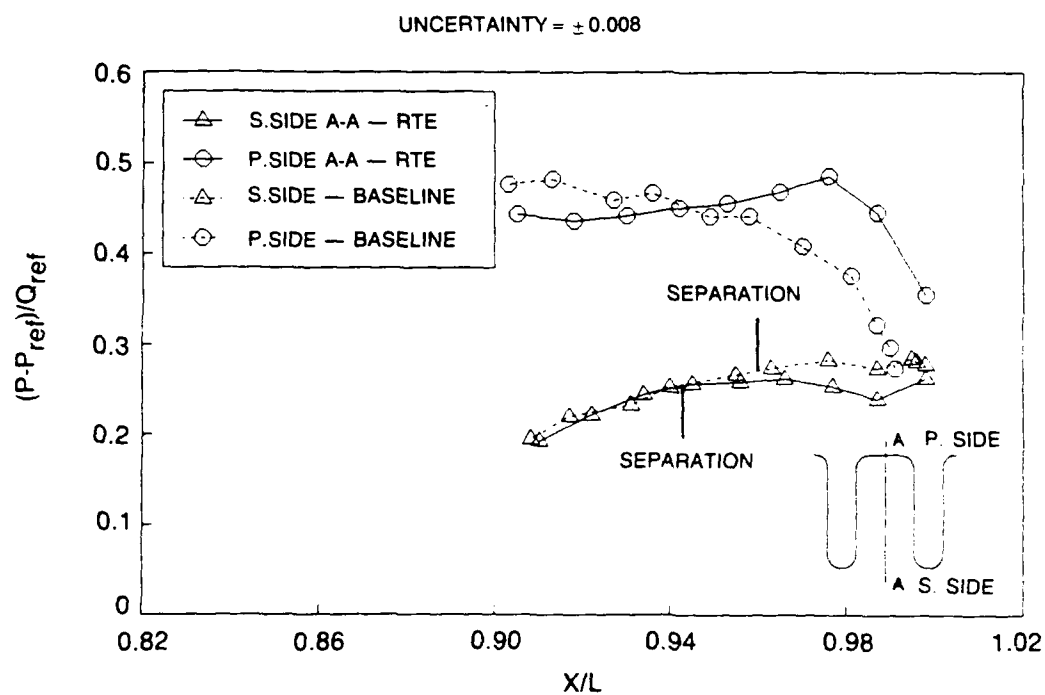
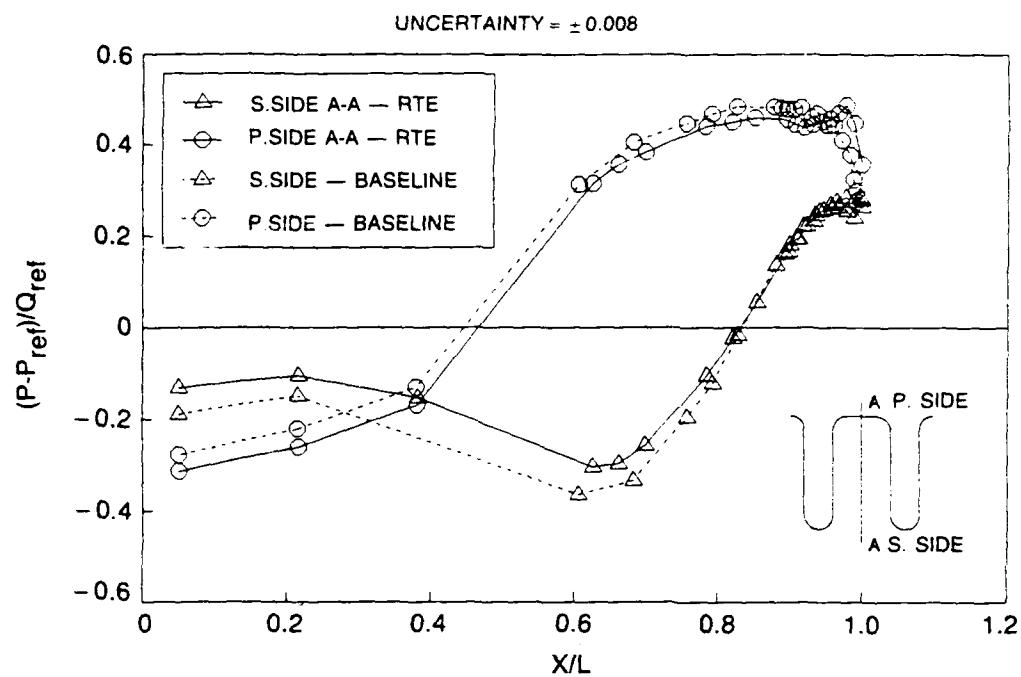


Figure 14. RTE Pressure Distribution Compared to Baseline — Section A-A

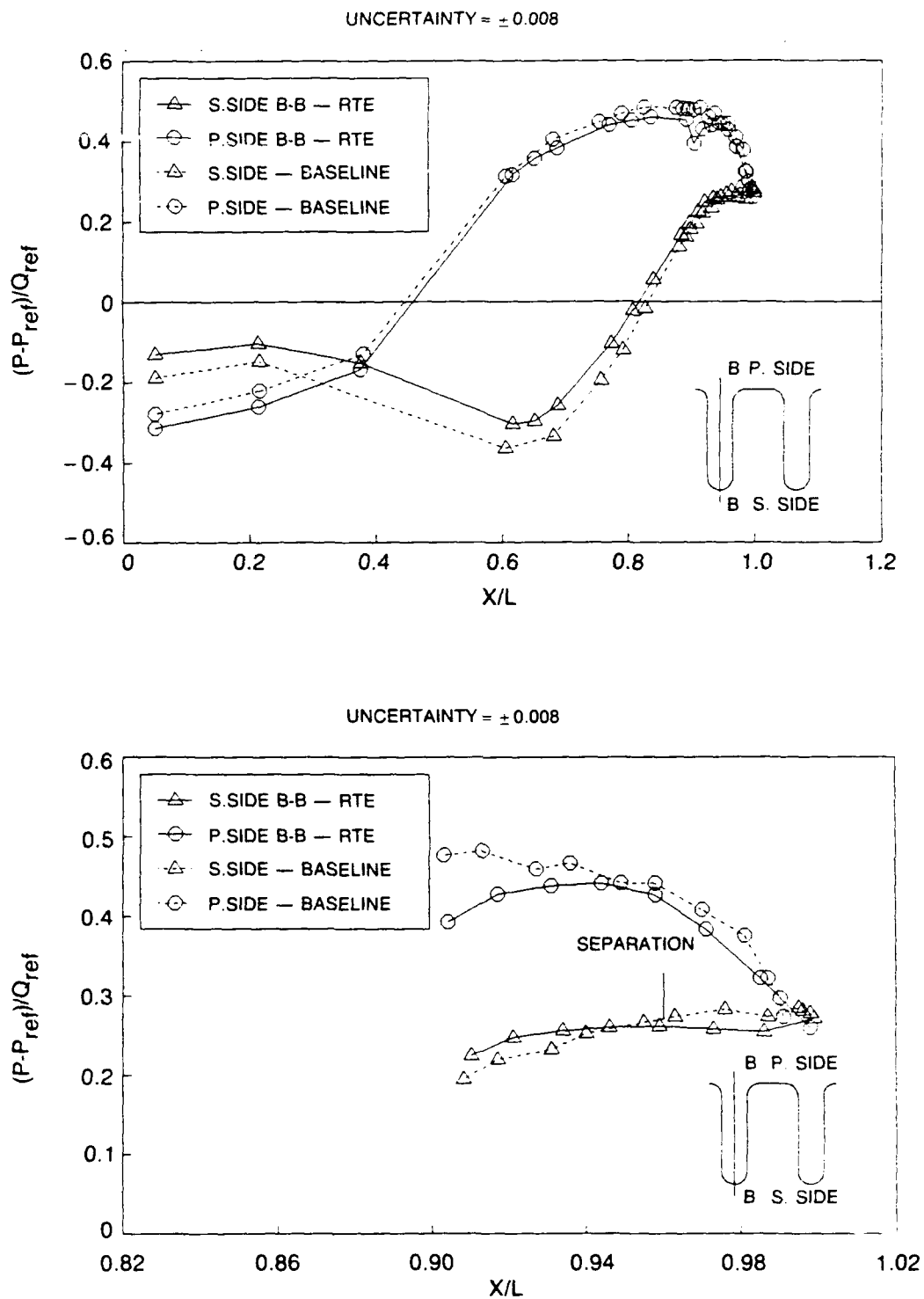


Figure 15. RTE Pressure Distribution Compared to Baseline — Section B-B

separation, which is verified by flow visualization in Figure 16. Reverse flow is observed over approximately 15.2 cm (6 in.) of the RTE compared to 10.2 cm (4 in.) of the baseline trailing edge.

It is interesting to note that even though the trailing edge stall was more severe with the RTE, only 2.54 cm (1.0 in.) H_2O of wall suction was required to obtain two-dimensional flow over 80% of the tunnel span compared to 19.1 cm (7.5 in.) H_2O to obtain two-dimensional flow over 35% of the span for the baseline configuration. The ripples broke the continuous trailing edge separation into isolated stall cells between lobes, thereby reducing the tendency of the sidewall boundary layers to migrate toward the low pressure region created by the separation.

The observed loading reduction shown, in Figures 14 and 15, is partially due to wind tunnel blockage effects. Flow visualization showed that the RTE was more grossly separated than the baseline trailing edge, and therefore, the wake convection angle of the RTE is greater (refer to Figure 17). Since the midgap streamlines were not adjusted to account for the increase in wake convection angle, a restriction is created in the suction side streamtube that would not occur in a true cascade of rippled trailing edge airfoils. This restriction increases the pressure in the suction side streamtube relative to that in the pressure side streamtube causing an apparent loss in airfoil loading. Had the midgap streamlines been adjusted to account for the increase in wake convection angle, the change in loading could be significantly less than the loss that was observed. For this reason, the changes in the measured pressure distributions will be referred to as changes in the "apparent" loading.

Nevertheless, the flow visualization in Figure 16 suggests that the three-dimensional boundary layer relief provided by the ripples did not overcome the adverse pressure gradient imposed on the boundary layer by 40 degrees of turning (30 degrees due to mean camber line turning, and 10 degrees due to the suction side lobe inclination angle). To increase the effectiveness of the ripples, a series of modifications were performed to the RTE. The final configuration (denoted RTE 2) is shown in Figure 18. In this configuration:

1. The suction side troughs were partially filled to produce the same turning in the troughs as the baseline model (i.e., $\alpha_s = 0$ degrees).
2. The suction side lobes were converged to the same width as the pressure side lobes.

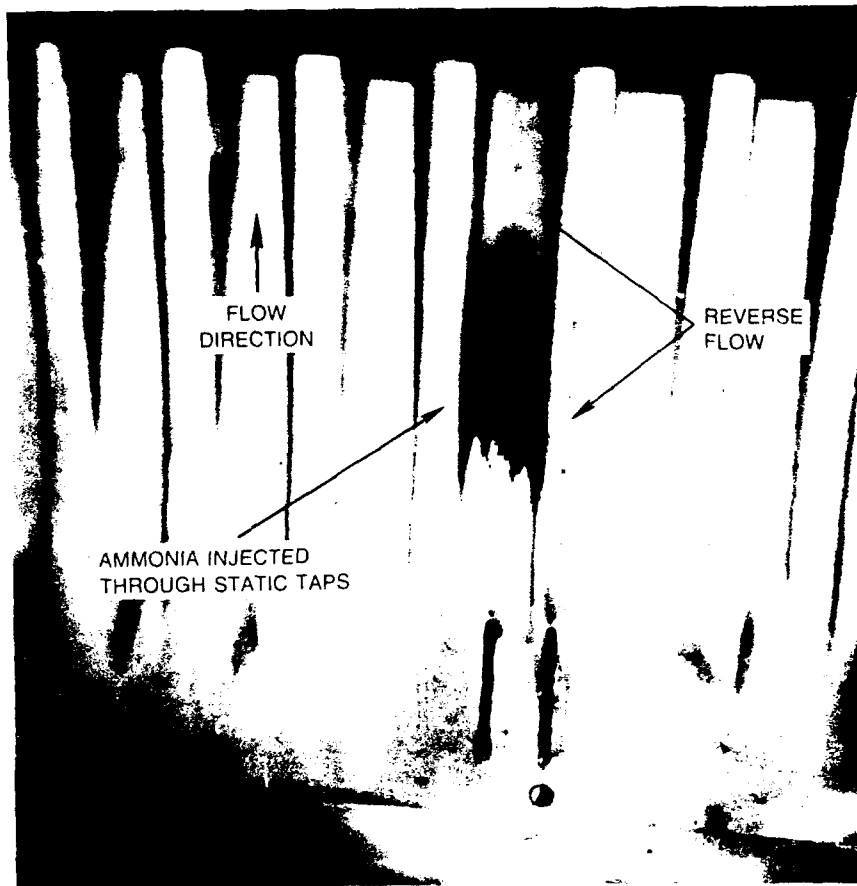


Figure 16. Surface Flow Visualization of RTE

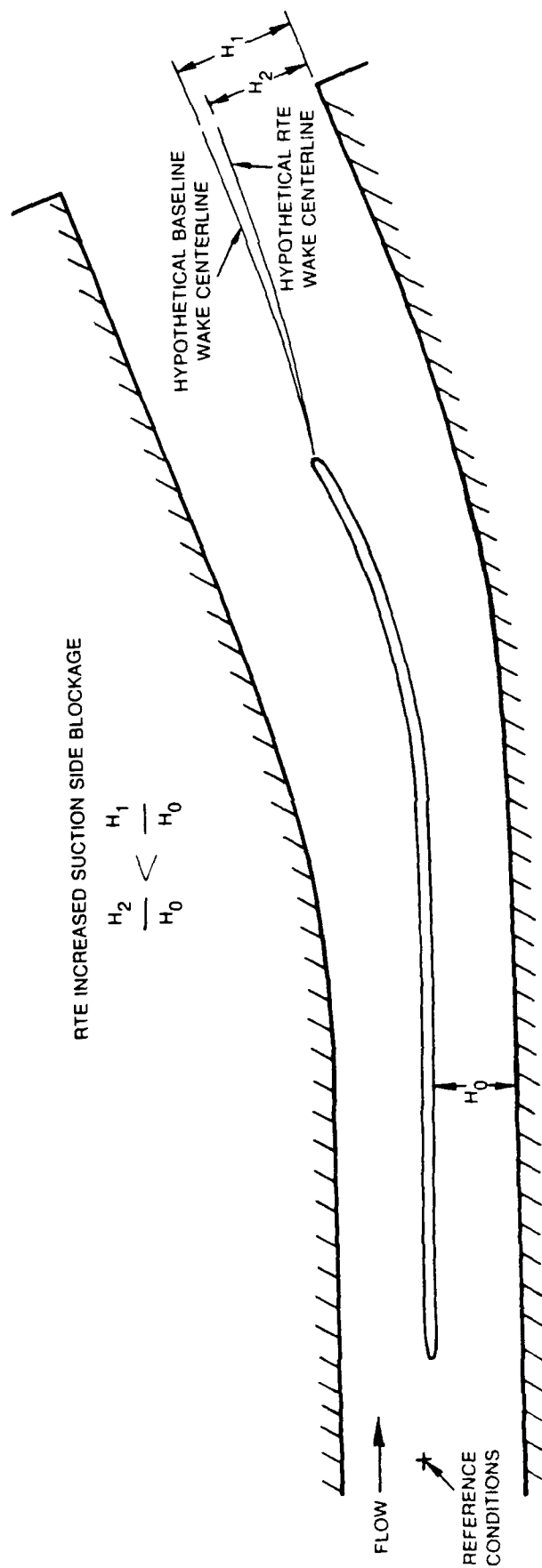
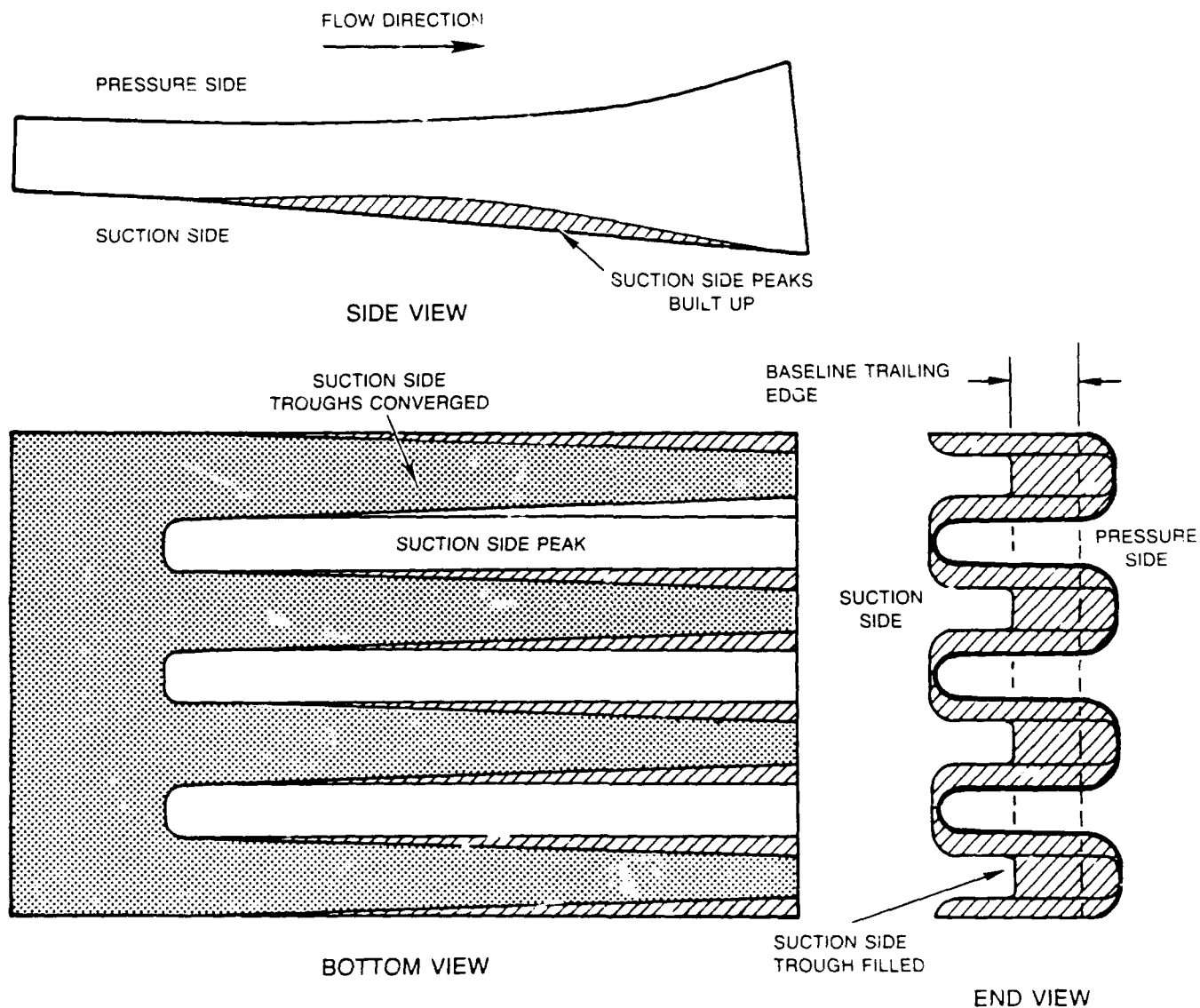


Figure 17. Wind Tunnel Blockage Effect Due to Change in Wake Convection Angle



CROSS-HATCHING SHOWS MODIFICATIONS PERFORMED

Figure 18. Modifications Performed to Obtain RTE 2

3. The suction side peaks were built up to increase penetration into the boundary layer.

These modifications resulted in a blunt trailing edge. Static taps on the suction side peaks were covered but those on the suction side troughs were kept open by extending them through the wax that was used to modify the trailing edge. Due to the time consuming nature of these changes, only five lobes centered around the suction side static pressure taps were modified. The ramifications of modifying only five lobes will be discussed later.

Flow visualization obtained from RTE 2 is presented in Figure 19. Each ammonia streak within the suction side trough is directed downstream indicating attached flow to the trailing edge. A comparison of the pressure distributions obtained with the two RTE models (Figure 20) shows that RTE 2 increased the "apparent" loading significantly, which is consistent with the elimination of separation and the resultant decrease in wake convection angle.

The baseline pressure distribution is compared to that of RTE 2 in Figure 21. Since the flow remained attached on RTE 2, an increase in the "apparent" loading was expected. However, the static pressure distribution in Figure 21 shows a small loss in "apparent" loading. This loss is partially due to modifying only five lobes rather than the entire span of 15 lobes. The loading distribution toward the leading edge is affected by the five unseparated lobes and the remaining separated lobes. As a result, the "apparent" loading is less than it would be if the entire trailing edge were unseparated.

Another possible cause for the drop in "apparent" loading is the empirical RTE design procedure which matches the suction side and pressure side penetration areas to maintain the same geometric centerline as the baseline. Since the transverse momentum on the pressure side is considerably greater than that on the suction side (due to a healthier boundary layer), matching the areas may shift the wake's mean centerline toward the suction side, increasing suction side blockage. This is further aggravated by filling in the suction side lobes as shown in Figure 18. The increased restriction due to three-dimensional contouring could negate the blockage reduction which results when separation is alleviated. As a result, the "apparent" loading could be reduced even though separation was alleviated.

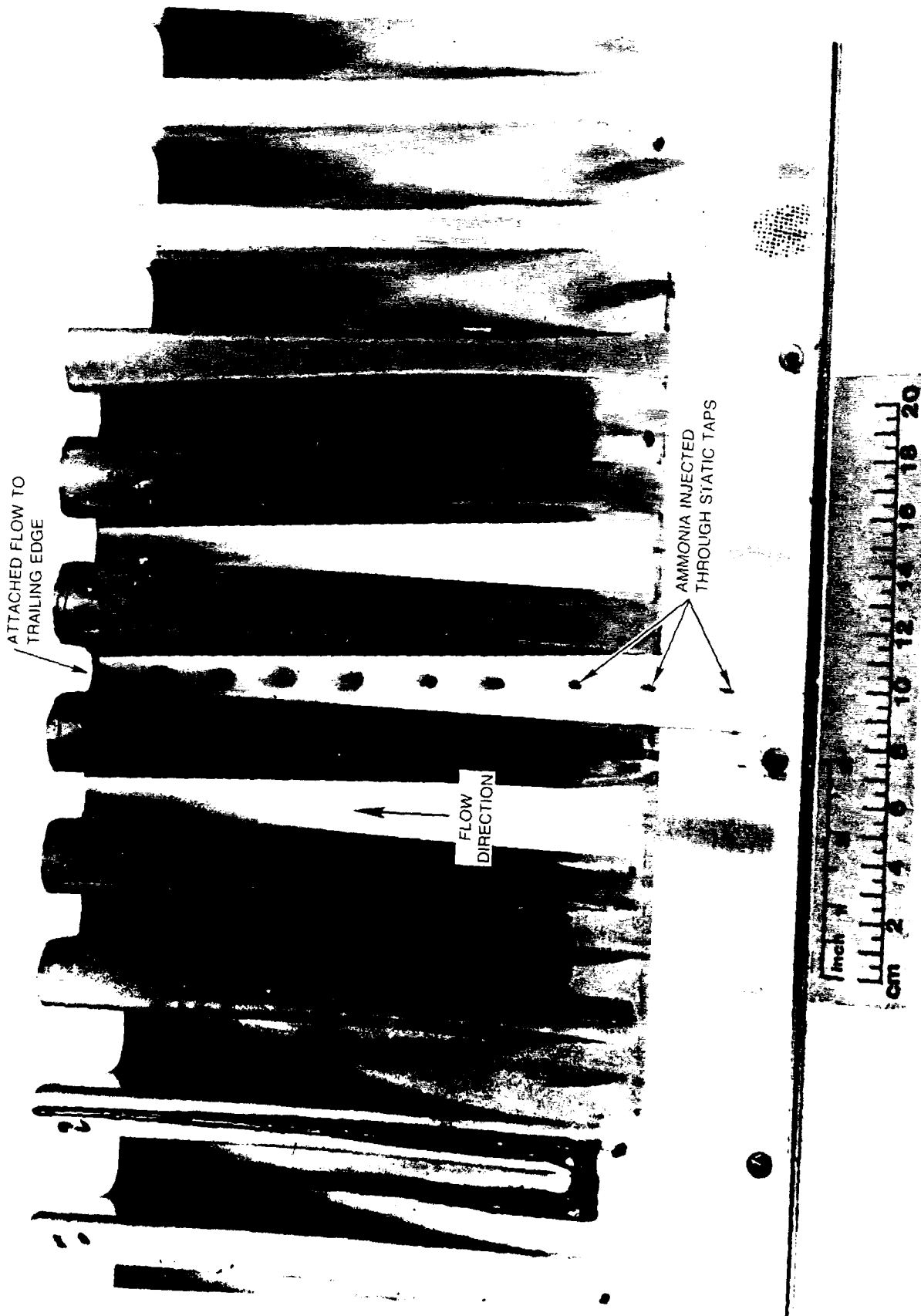


Figure 19. Surface Flow Visualization of RTE 2

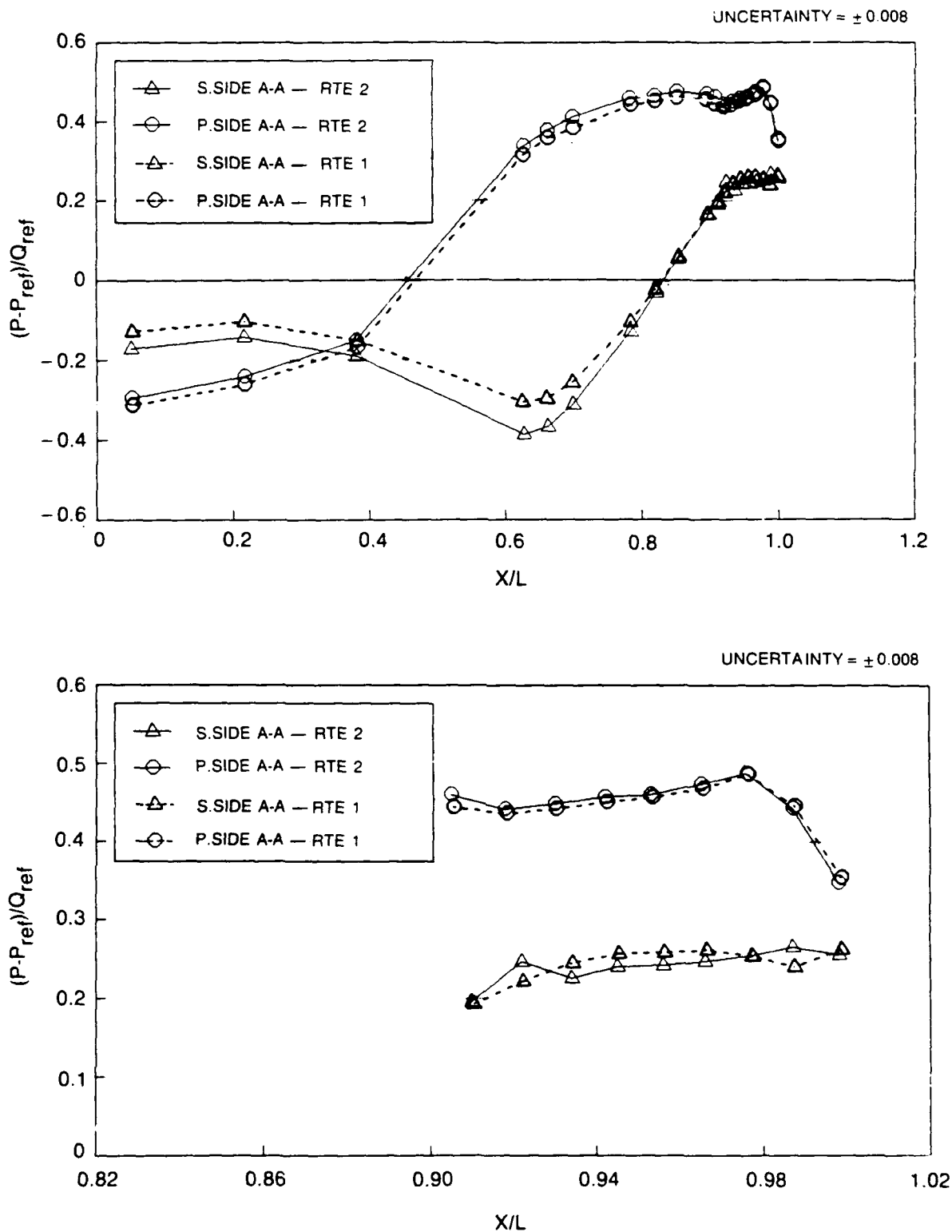


Figure 20. Comparison Between RTE Configurations

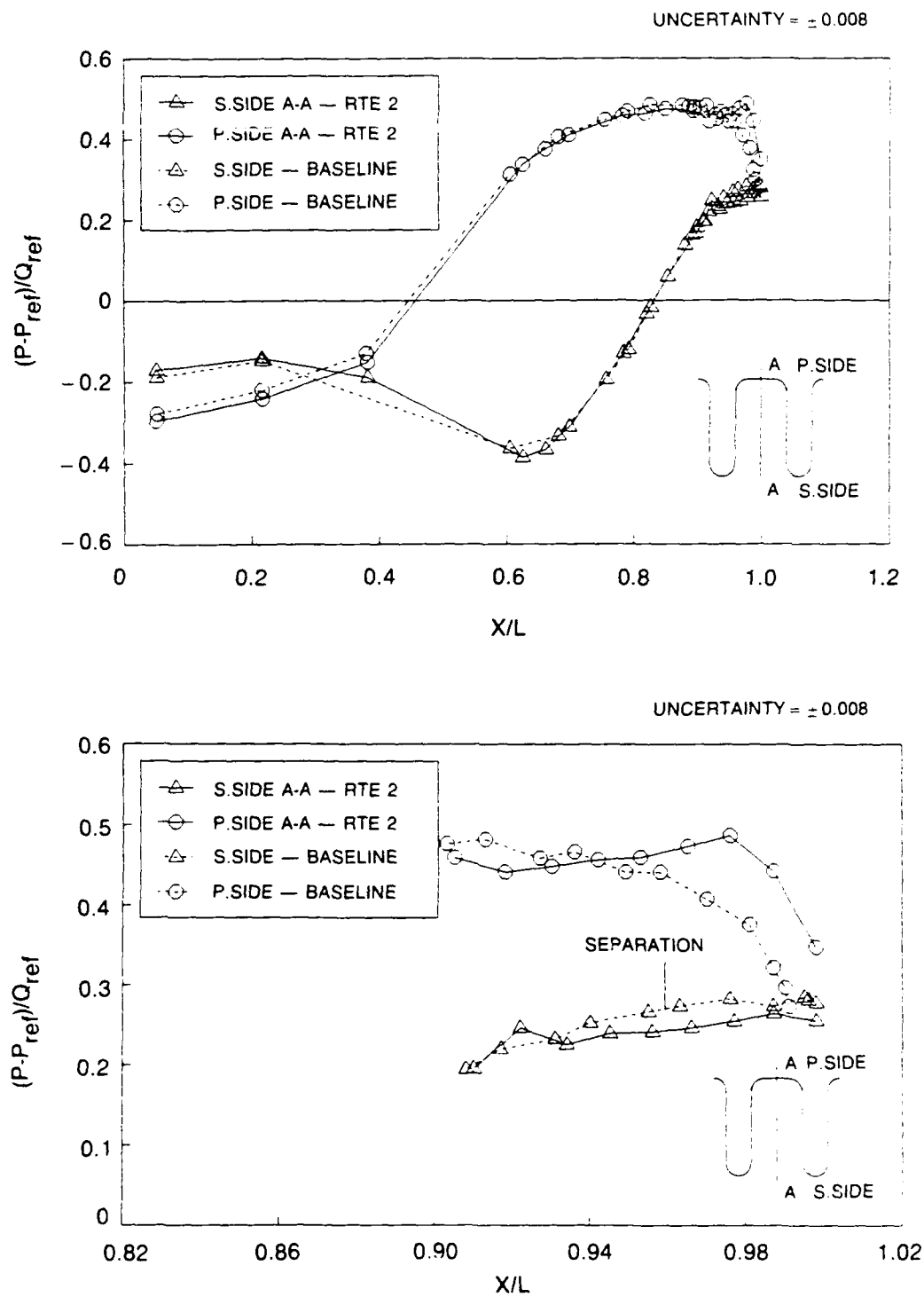


Figure 21. RTE 2 Pressure Distribution Compared to Baseline — Section A-A

Note that the suction side pressure distribution (section A-A) still flattens toward the trailing edge, even though the flow is attached. This flattening is attributed to local boundary layer relief within the converging lobe. It is likely that the suction side pressure distribution over section B-B rises continuously to the trailing edge; however, this distribution could not be measured due to the modifications performed.

To summarize the results from the high loading configuration, the original RTE design aggravated suction side boundary layer separation. This resulted in an increase in the wake convection angle which produced a large reduction in the "apparent" airfoil loading. The term "apparent" is used because the midgap streamlines were not adjusted to account for the increase in the wake convection angle. Modifications were performed on the original RTE to come up with a second design (RTE 2). This design eliminated the large scale separation that was present with both the circular trailing edge and the original RTE. However, this design also showed a small "apparent" loading reduction which was attributed to a combination of modifying only five lobes, and a possible increase in the wake convection angle due to the three-dimensional contouring of the trailing edge. It is unknown what effect the RTE 2 contouring would have on the actual airfoil loading if it were tested in a two-dimensional cascade of multiple RTE airfoils.

Analytical Results

The analytical procedures described in the previous section have been applied to a series of simpler but relevant unit problems to demonstrate the applicability of the methodology to highly loaded airfoils and to the generation of streamwise vorticity through surface contouring. While our initial intent was to apply both the Mook and VSAERO analyses to the same problems, development problems and time limitations necessitated using the more mature VSAERO analysis exclusively.

For the first unit problem, a calculation of the highly loaded baseline cascade configuration was made. The cascade was modeled in a similar fashion to the experimental setup, i.e., only a single airfoil was analyzed. The periodic effect of adjacent airfoils has been simulated, as in the actual experiment, by placing contoured tunnel walls at the calculated midgap streamline locations. A two-dimensional inviscid finite-difference calculation was performed for the actual cascade. The midgap streamline was then determined and was used to define the wall contours. The effect of boundary layer growth

on the airfoil and tunnel walls was simulated as a displacement effect of the midgap streamline location. Figure 22 illustrates the analytical representation of the baseline configuration. The experimental tunnel sidewall spacing was further modified to correct for the airfoil blockage not included in the present camber line representation. The airfoil surface was modeled using 20 axial segments, however the entire tunnel/model simulation required 592 panels. A three-dimensional representation was used even though no lateral geometrical variation was present. The predicted VSAERO analysis surface static pressure distribution and the corresponding measured data are shown on Figure 23. The agreement is quite good over a majority of the surface, but the inviscid analysis does not predict the suction side trailing edge separation, and therefore also indicates an overloading on the pressure side. A two-dimensional strip boundary layer analysis was performed using the VSAERO surface velocity distribution and a laminar leading edge start. Transition to fully turbulent flow was induced at a location corresponding to the location of the physical trips used in the experiment.

In the second unit problem, a calculation of a generic symmetric lobed configuration installed axially in a "tunnel" of constant cross-section was considered. The intent of this calculation was to verify that lateral periodicity could be simulated. The lobe surface was constructed from sinusoidal cross-sectional contours and a largely straight ramp surface. A side view and rear view of the lobe geometry and a three-quarter paneled view of the entire lobed "airfoil" and "wind tunnel" is shown in Figure 24. The airfoil surface was defined using 44 axial segments, with the lobed portion using 20 spanwise segments to define a complete period of the lobe. The entire simulation (without the wake) required 904 panels. An examination of the surface velocity components verified that both periodicity and local surface flow tangency were being satisfied. A display of the calculated surface pressure coefficient, C_p , is shown in Figure 25. The effect of the strong adverse pressure gradient from the lobe crest on the top surface (pressure $\theta = 0$ deg) to the lobe trough on the top surface (suction $\theta = 0$ deg) is clearly seen in the lobe crest and mid-lobe C_p distributions. The code imposes a Kutta condition forcing the pressure and suction surface trailing edge C_p to be equal, however, the last axial data point displayed in Figure 25 is axially located a half panel from the trailing edge. The irregular lobe crest suction surface pressure distribution does indicate some modeling problems that will be dis-

R89-957707

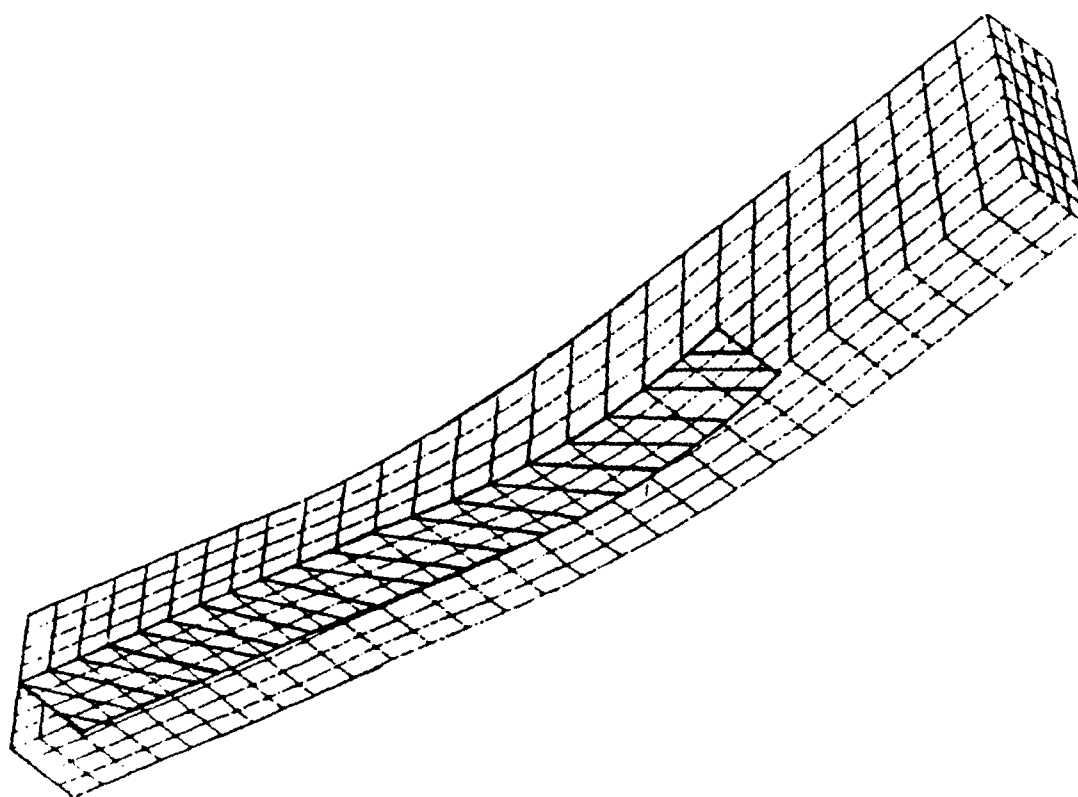
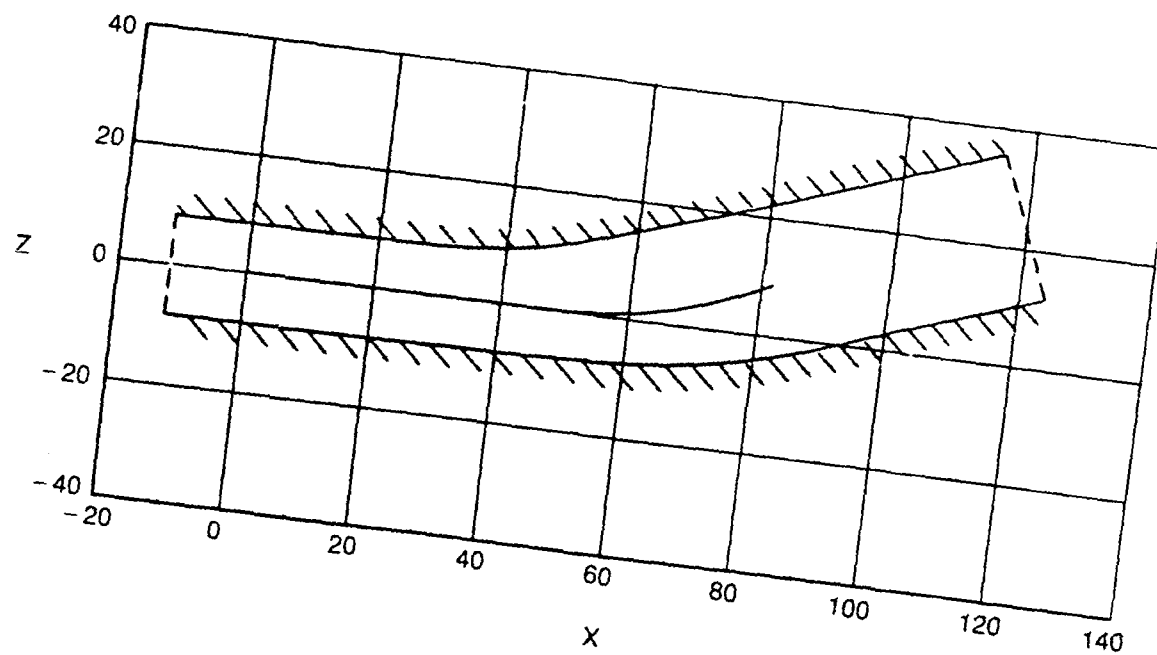


Figure 22. Geometric Model of Baseline High Loaded Vane/Wind Tunnel Using VSAERO

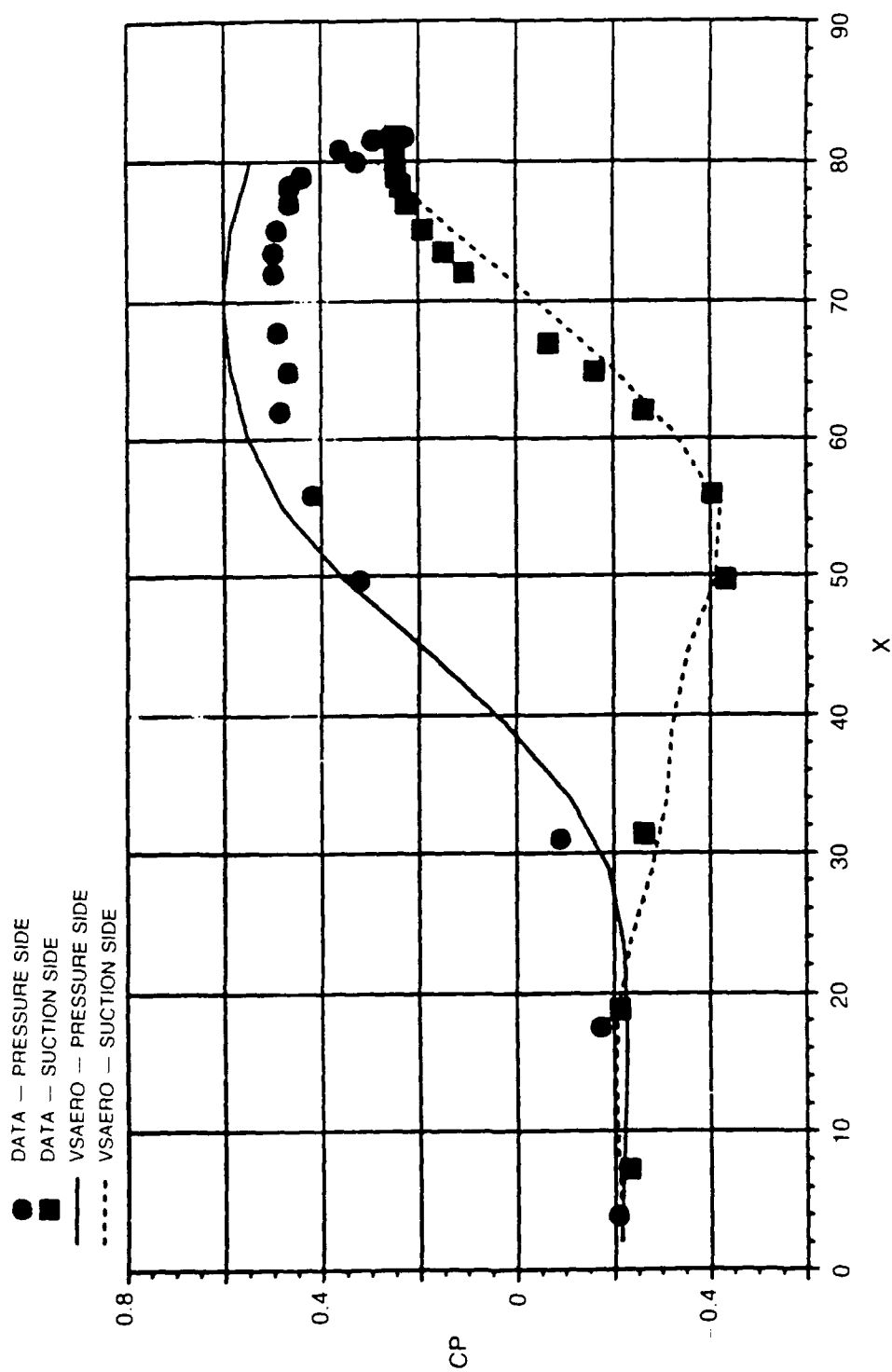


Figure 23. VSAERO Predicted Surface Pressure Loading Compared to Baseline High Loaded Vane Data

R89-957707

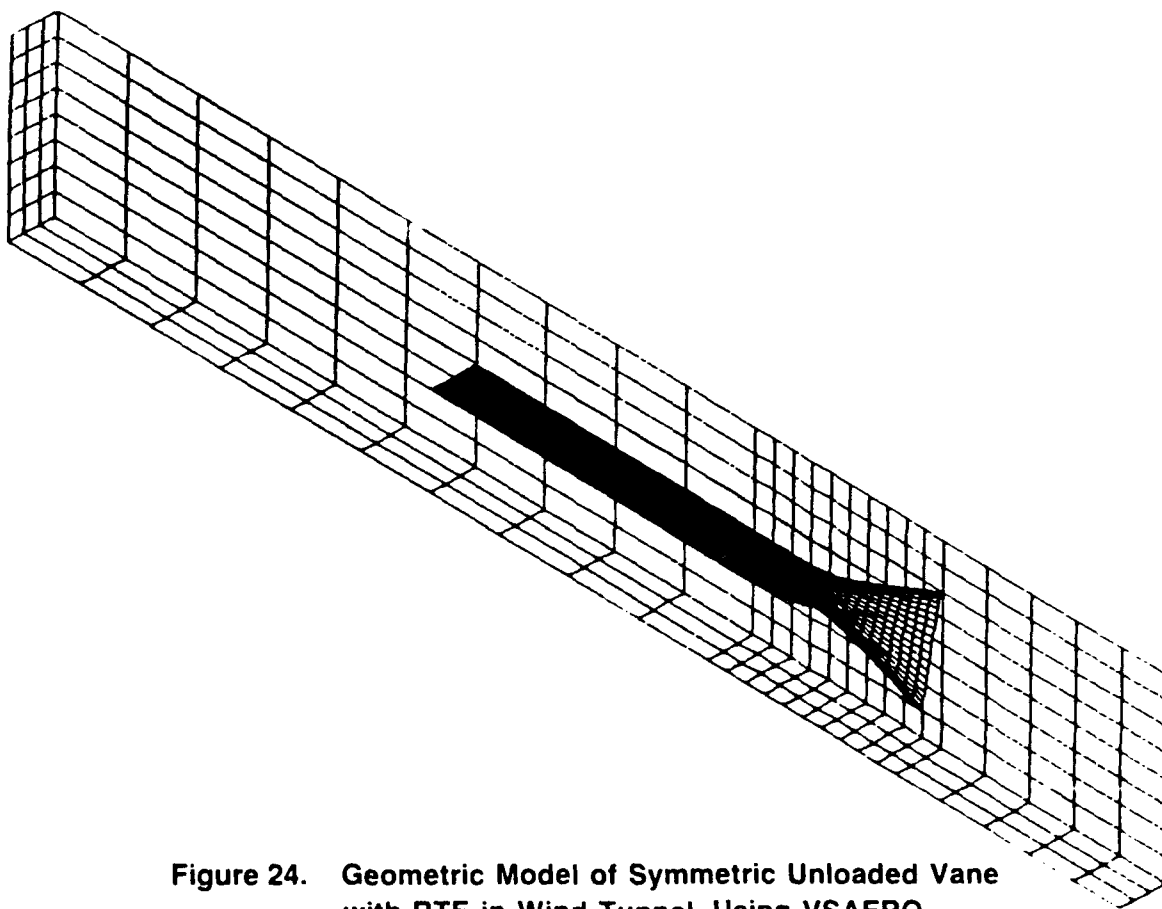
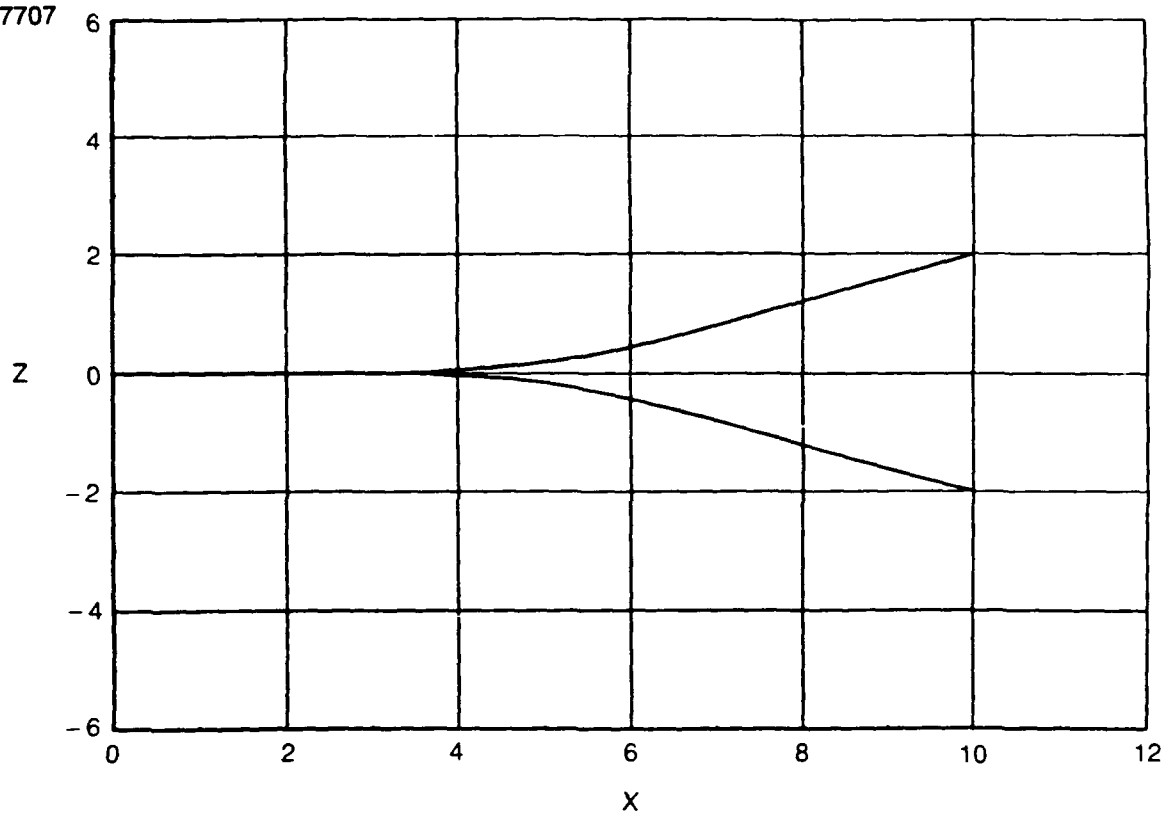


Figure 24. Geometric Model of Symmetric Unloaded Vane with RTE in Wind Tunnel Using VSAERO

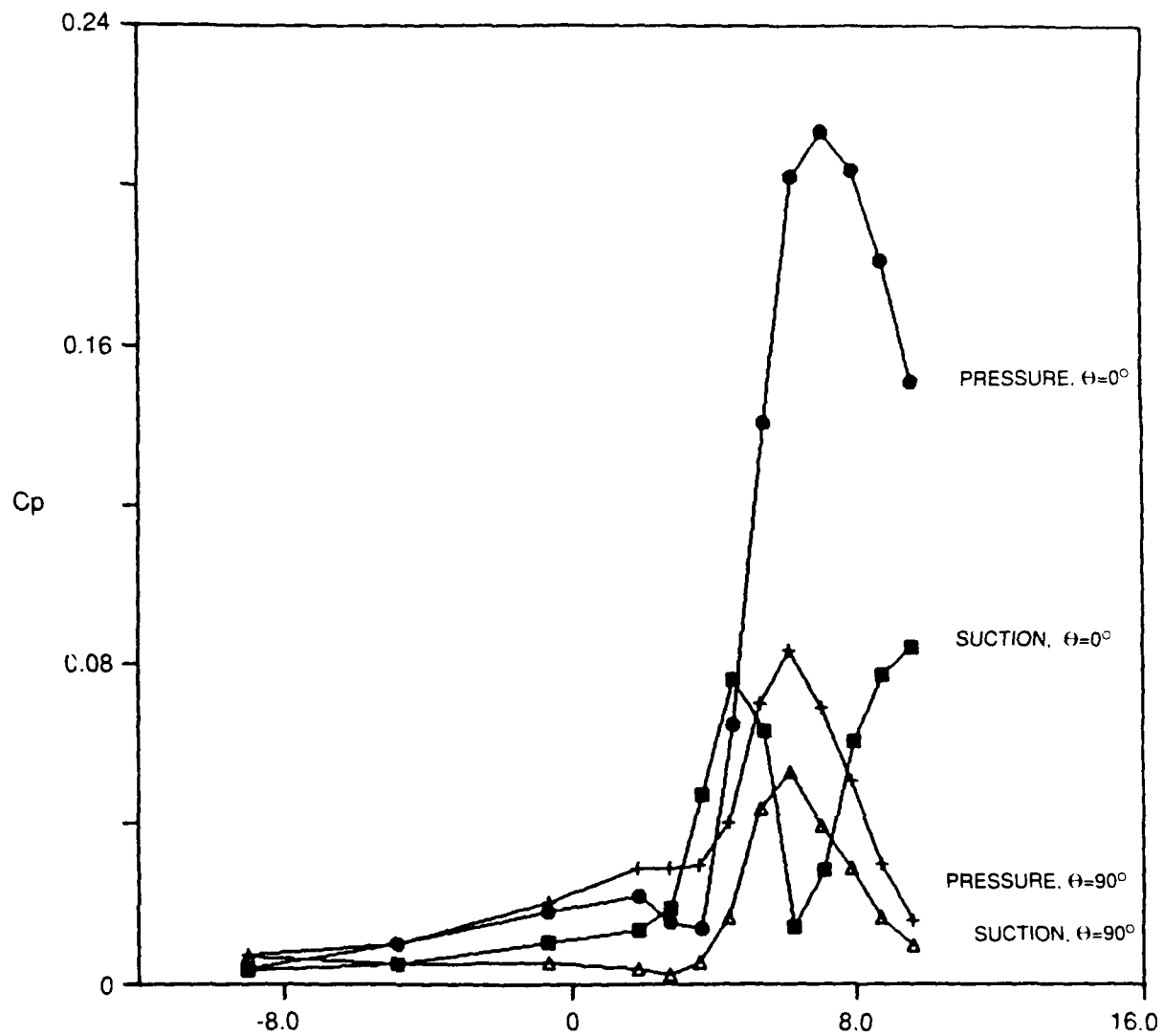


Figure 25. VSAERO Predicted Surface Pressure Loading for Unloaded Vane with RTE

cussed shortly. While surface flow solutions are directly obtained from the solver, flow field definition at other points is possible using "off body" calculations, where the effect of all surface singularities are summed at each point of interest. The spanwise pressure gradient, symmetric about each crest induces a counter-rotating vortical pattern.

In the final calculation, the complete high loading RTE airfoil configuration was analyzed. The tunnel sidewall contour was the same used in the initial or baseline simulation. No attempt was made to modify the midgap streamlines (tunnel sidewalls) to account for the effect of the rippled trailing edge on the midgap streamline (tunnel wall) contour. The RTE airfoil surface, as seen in Figure 26, was modeled using the same 20 axial segments as used in the baseline calculation, with an additional 15 axial segments to define the rippled trailing edge. A complete period of the lobe was modeled using 15 spanwise segments. The entire simulation (without the wake) required 1132 panels. The VSAERO predicted surface loading for the high loading RTE airfoil, as seen in Figure 27, showed a significant change from the baseline calculation. A study of the experimental data, however, indicates the lobe surface causes only a localized effect on the vane pressure loading. A color contour display of the pressure and suction side lobe surface loading patterns is shown in Figure 28 to illustrate the global features of the lobe surface loading. While the analysis predicts a lower trailing edge loading on the pressure surface, as in the experiment, the suction surface loading is also decreased, in contrast to the observed experimental behavior. Similar anomalous predictions have been previously noted in other internal flow calculations using the thin surface approximation. In those instances, no solution improvement was observed when the number of panels was substantially increased. An alternative approach would be to model the actual surface with finite thickness, however, such a configuration would require many more panels than the 5000 panel maximum currently found in the VSAERO code.

An alternative zonal analysis approach would be to assume that the effect of the rippled trailing edge would be localized and only affect the trailing edge region. In such a scenario, a two-dimensional finite thickness baseline solution would be evaluated and flow profiles determined at the three-quarter chord location. These profiles would then be used as boundary conditions for a full three-dimensional, finite thickness analysis of the trailing edge region. Such an approach however, is beyond the scope of the current program.

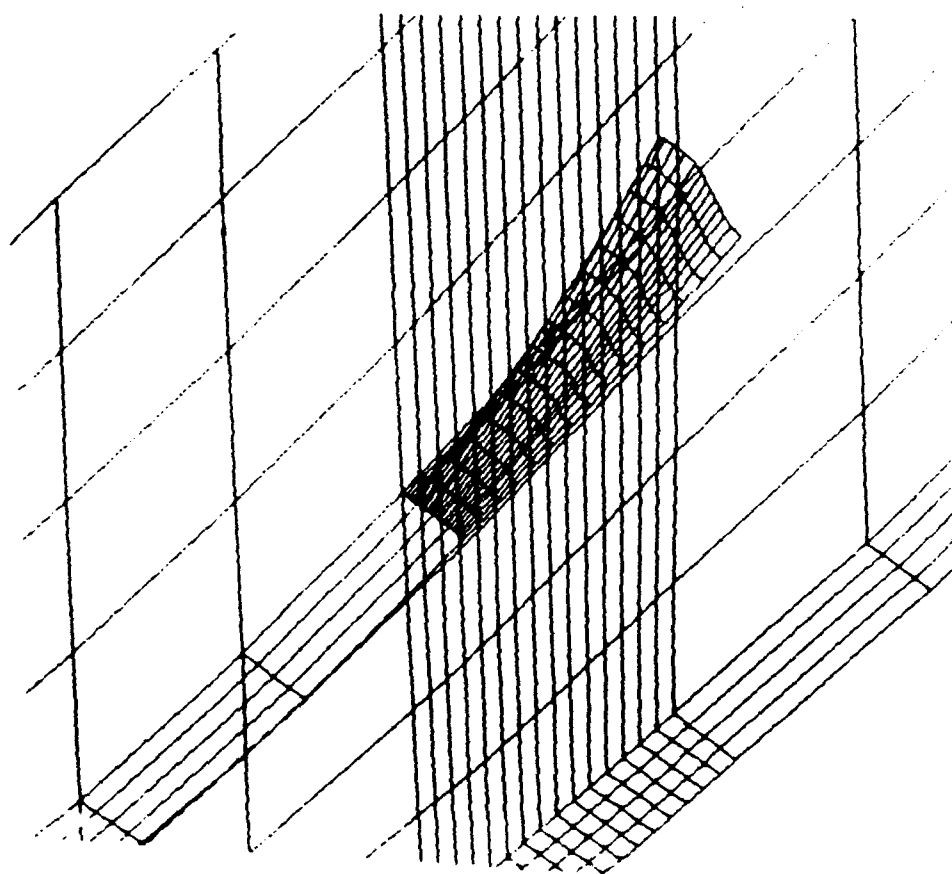
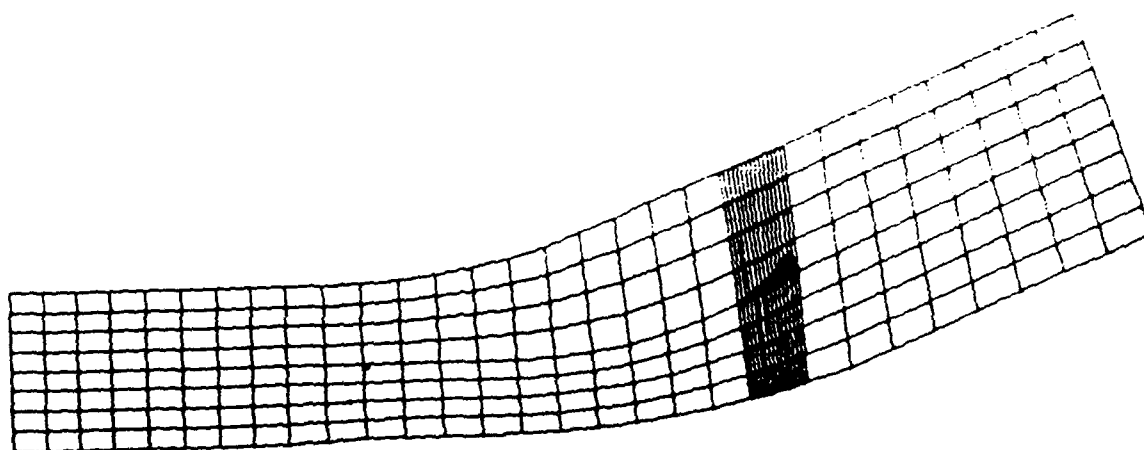


Figure 26. Geometric Model of High Loaded Vane with RTE/Wind Tunnel Using VSAERO

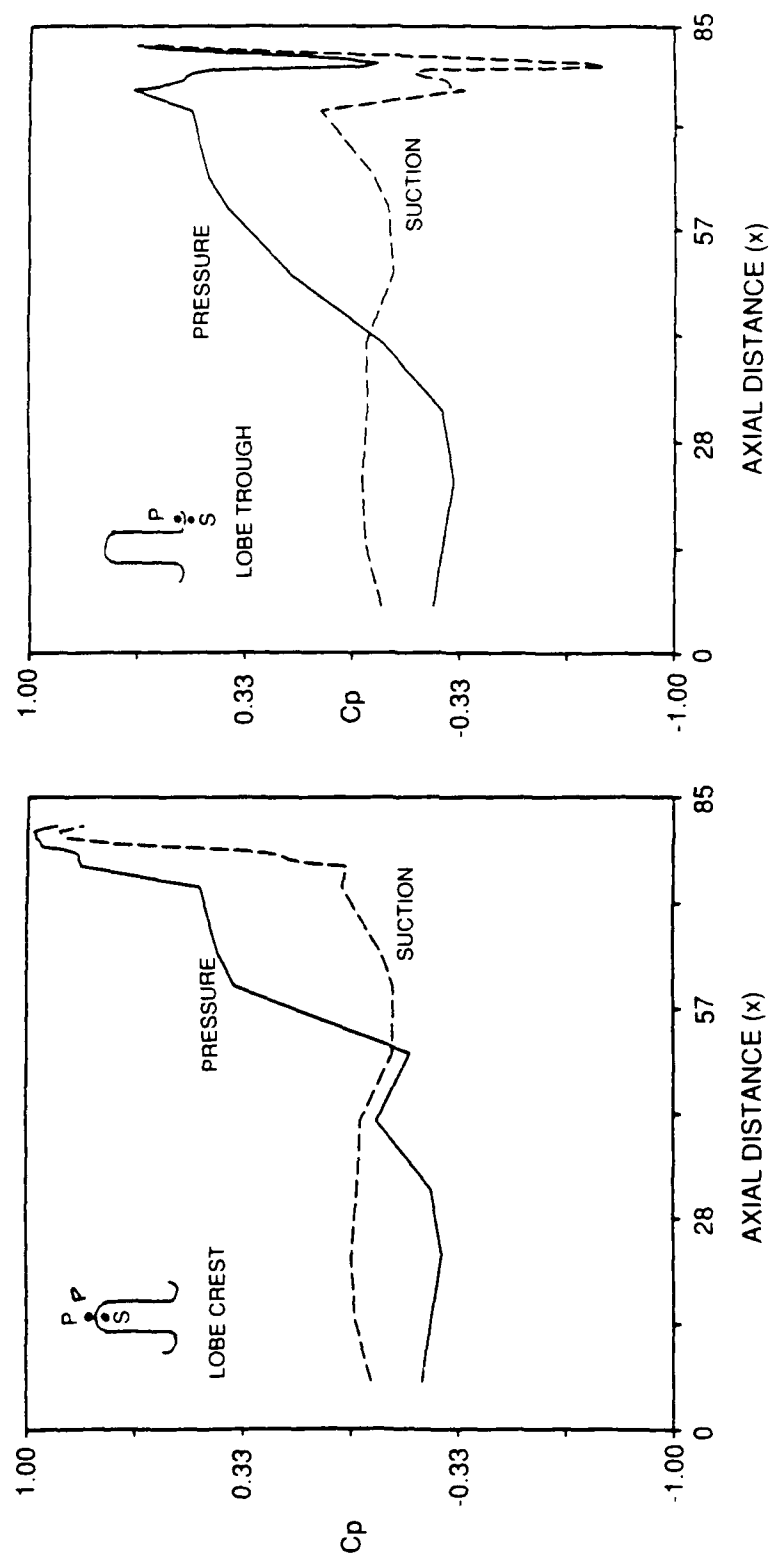


Figure 27. VSAERO Predicted Surface Pressure Loading for High Loaded Vane
with RTE

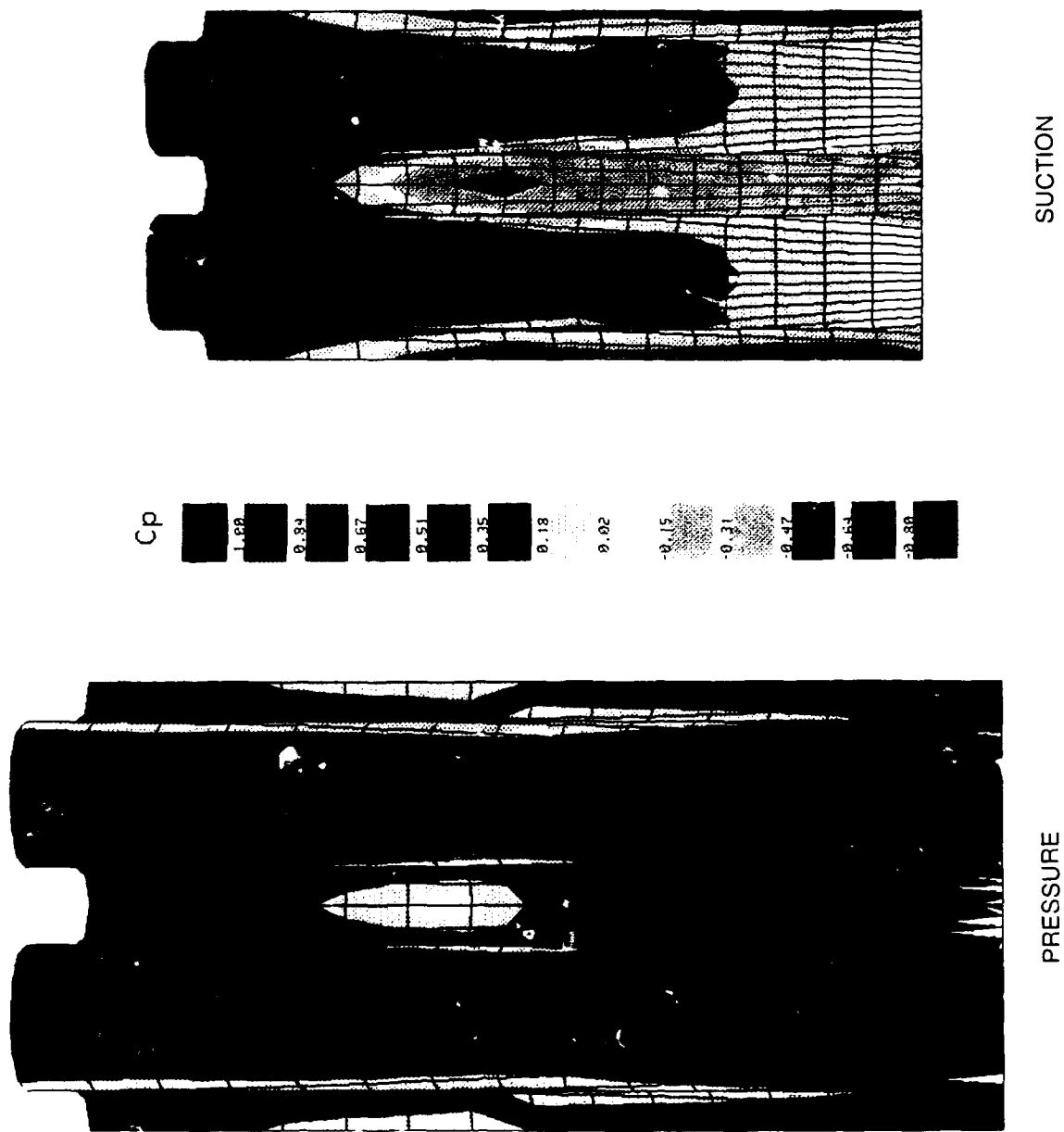


Figure 28. VSAERO Predicted Loading Contours for High Loaded Vane with RTE

Low Loading Configurations

Static pressure distributions from the low loading configurations are presented in Figures 29 through 31. The overall loading distributions are normalized to the upstream reference conditions, P_{ref} and Q_{ref} , while the distributions near the trailing edge are normalized to the cascade exit conditions, P_e and Q_e , which were measured at approximately $x'/t = 35$. This latter scaling is used to obtain the base pressure coefficients for each model as described in Reference [3].

Each grooved trailing edge reduced the "apparent" airfoil loading relative to the baseline circular trailing edge. This effect is due to the three-dimensional trailing edge variation which tends to shift the wake's centerline due to vectoring of the healthier pressure side boundary layer toward the suction side. The "apparent" loading reduction observed from Model 4 with the shallowest grooves suggests that the wake centerline is very sensitive to three-dimensional perturbations in the trailing edge contour.

Based on the trailing edge pressure distributions, grooving the trailing edge has a significant impact on base pressure. Base pressure coefficients, $(P_b - P_e)/Q_e$, are presented in Table 1 for each configuration. The base coefficients increased with groove depth except of Model 4 which showed a small decrease, though it was well within the measurement uncertainty shown in Figures 30 through 32.

TABLE 1
BASE PRESSURE COEFFICIENT

Model	Groove Depth (cm)	C_{pb}
1	0.00	-0.193
2	1.43	-0.134
3	1.11	-0.165
4	0.64	-0.198

In terms of base pressure recovery, the best configuration was Model 2 which increased C_{pb} from -0.193 to -0.134. This increase was attributed to the elimination of vortex shedding and the reduction in base area. A hot film spectrum (see Figure 32) obtained at $x'/t = 2.5$ downstream of the baseline trailing edge showed vortex shedding to occur at a frequency of 131 Hz, consistent with results from Reference [3]. The corresponding spectrum obtained downstream of Model 2 showed no indication

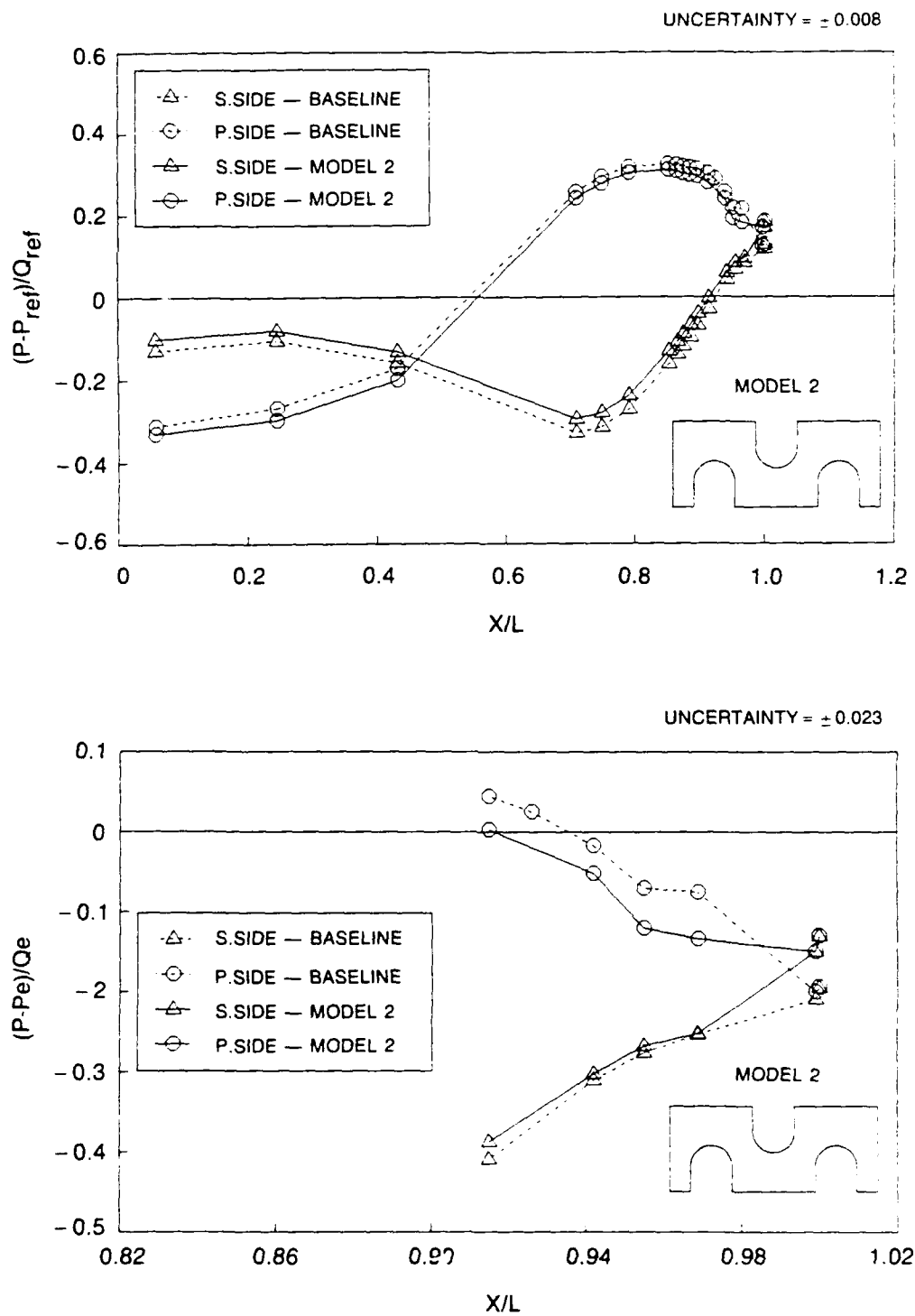


Figure 29. Model 2 Pressure Distribution Compared to Baseline

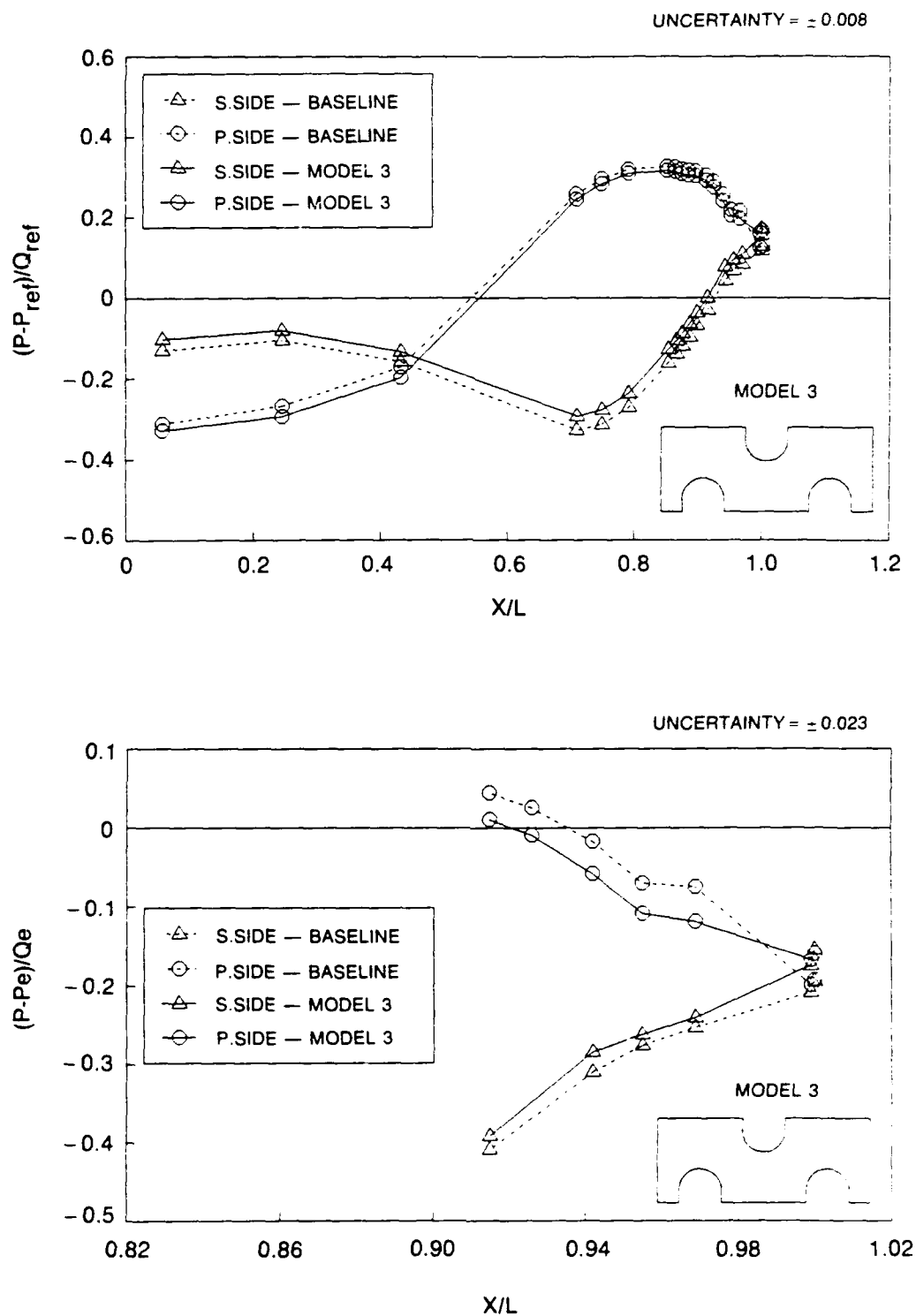


Figure 30. Model 3 Pressure Distribution Compared to Baseline

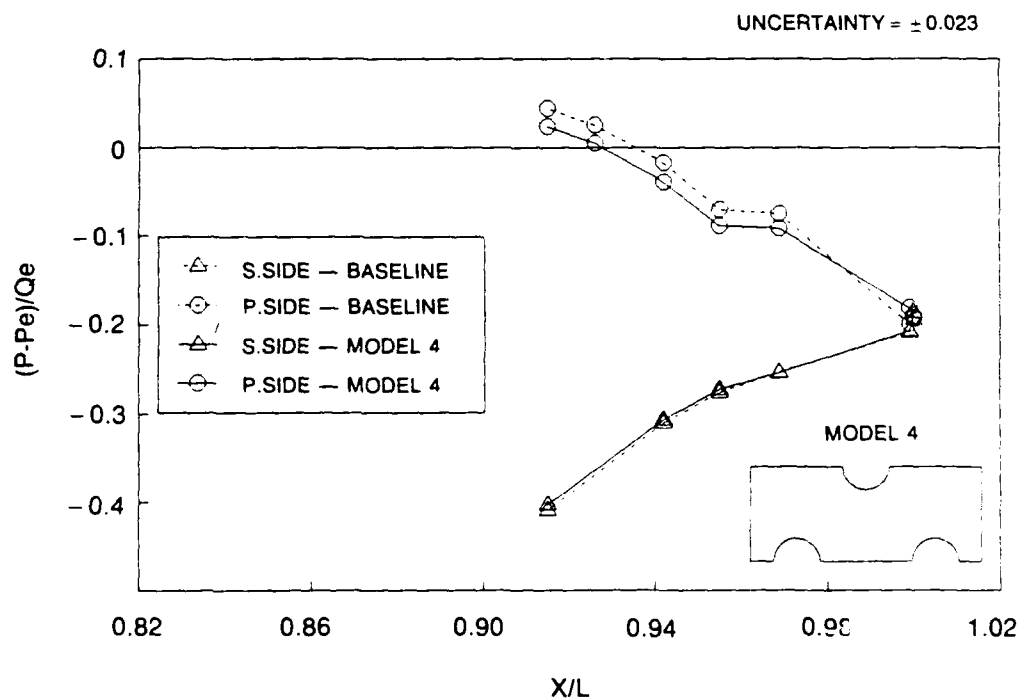
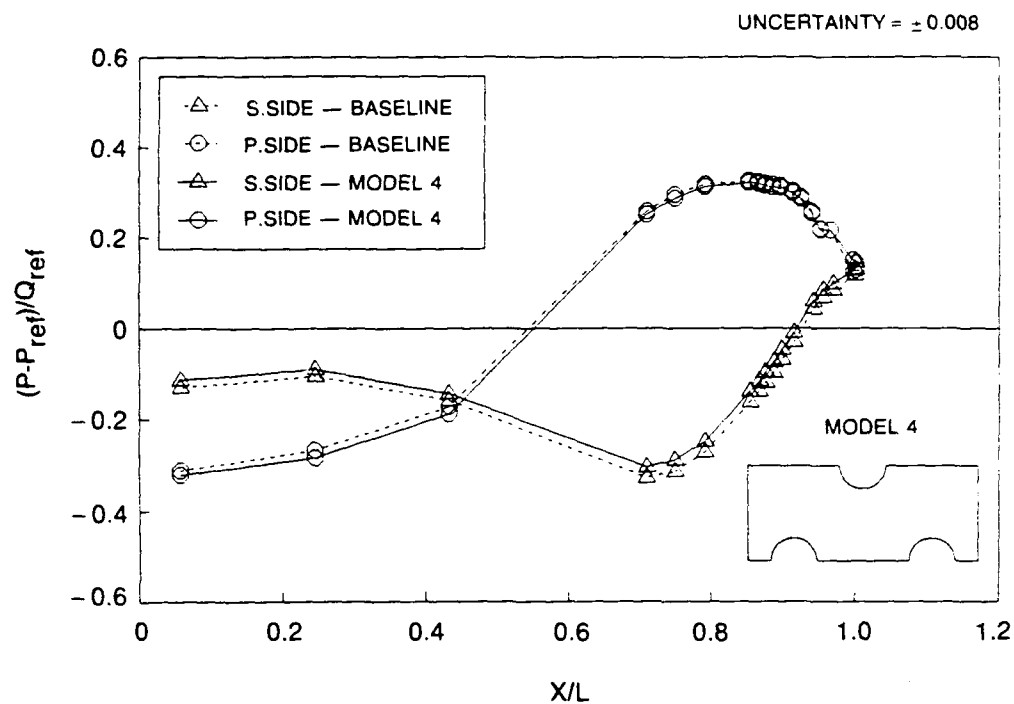
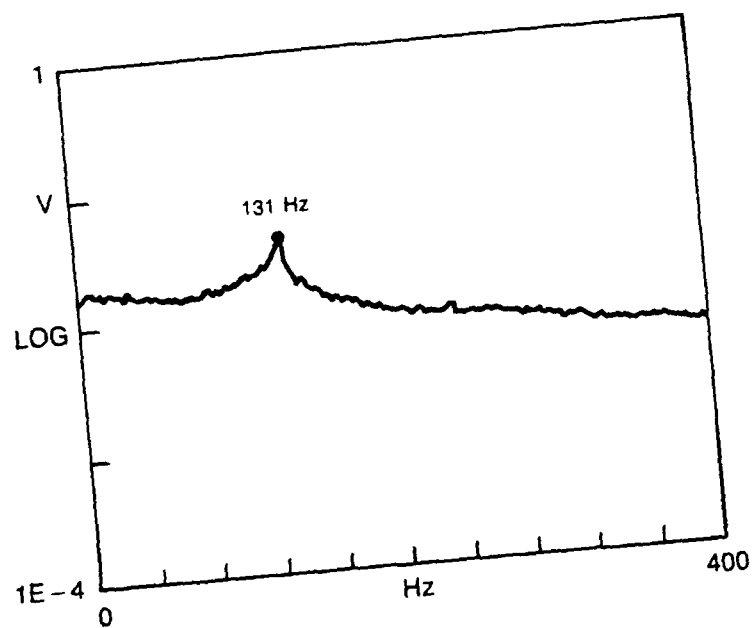
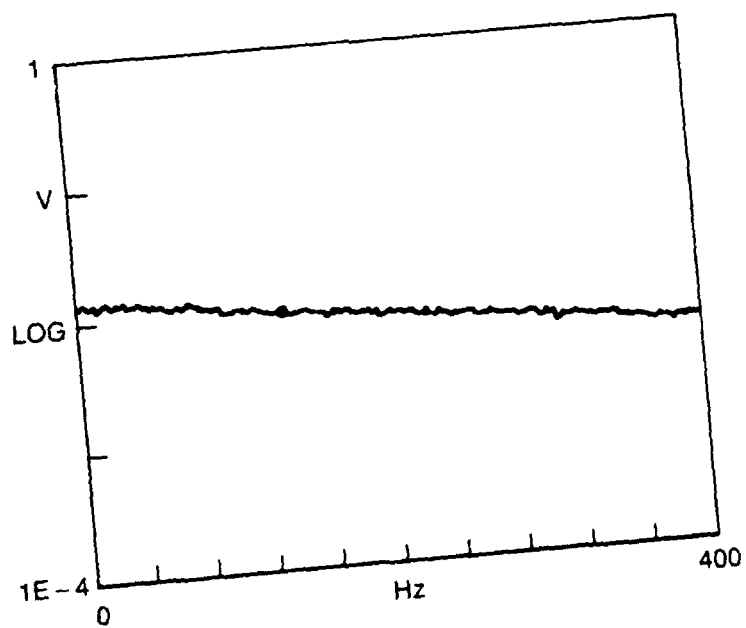


Figure 31. Model 4 Pressure Distribution Compared to Baseline



a) BASELINE



b) MODEL 2

Figure 32. Hot Film Spectra Downstream of Model 1 and Model 2

of vortex shedding. A similar result is described in Reference [22] in which the blunt trailing edge of a flat plate was segmented to break up its coherence. Such configurations were shown to eliminate vortex shedding and increase the base pressure coefficient from -0.44 to -0.16 . However, results from Reference [19] suggest that the elimination of vortex shedding from Model 2 may have resulted from the reduction in base area rather than the discontinuous trailing edge. The grooves in Model 2 reduced the base area by roughly 36%, giving an effective trailing edge thickness of 1.64 cm (0.64 in.). Results from Reference [19] show that a 1.27 cm (0.5 in.) diameter circular trailing edge tested in the same facility, with the same flow conditions and upstream model geometry as Model 2, did not shed vortices. That trailing edge had a base pressure coefficient of -0.109 , which is a significantly higher base pressure recovery than that of Model 2.

Total pressure profiles obtained at $x'/t = 11.25$ downstream of each model are presented in Figures 33 through 36, and velocity profiles are presented in Figure 37 through 40. The velocity profiles were calculated from the total pressure profiles and the measured wall static pressure, assuming that there was no static pressure gradient across the wake. This assumption is quite valid at this far downstream location. Due to the three-dimensionality of the grooved trailing edges, profiles were obtained at ten spanwise locations: five to the left of the tunnel centerline ($z < 0$), and five to the right of the tunnel centerline ($z > 0$). For the circular trailing edge, only four profiles were obtained, two on either side of the centerline. The abscissa is presented as $y' - y'_{P_{t-\min}}/t$, where $y'_{P_{t-\min}}$ is the y' -location at which the minimum P_t was measured at a given spanwise location. Presented in this manner, the profiles for a given model are very similar at each spanwise location. With that in mind, the profiles were arithmetically averaged to obtain the profiles in Figures 41 and 42. The average profiles show that the grooves increase the total pressure defect from 42% to 46% of Q_{ref} , increased the velocity defect from 34% to 39% of V_{fs} , but substantially reduced the wake width.

The total pressure and velocity distributions were used to calculate overall cascade head loss.

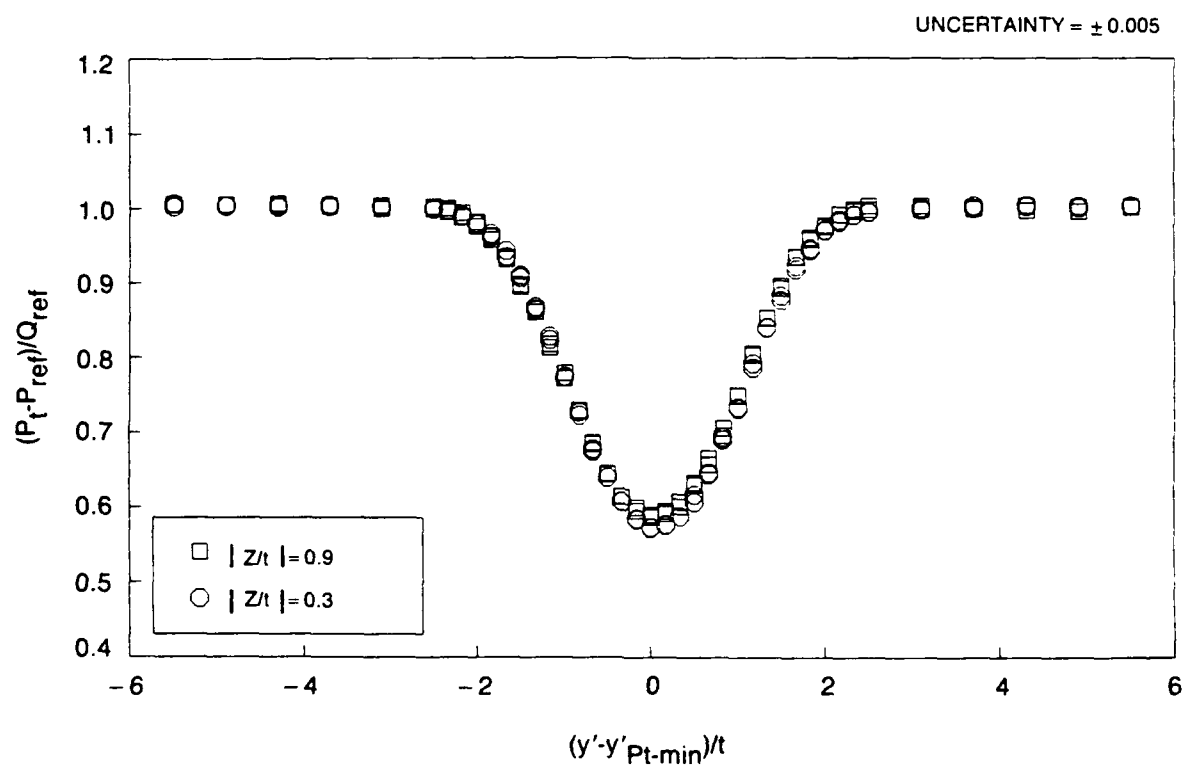


Figure 33. Total Pressure Profiles Downstream of Model 1

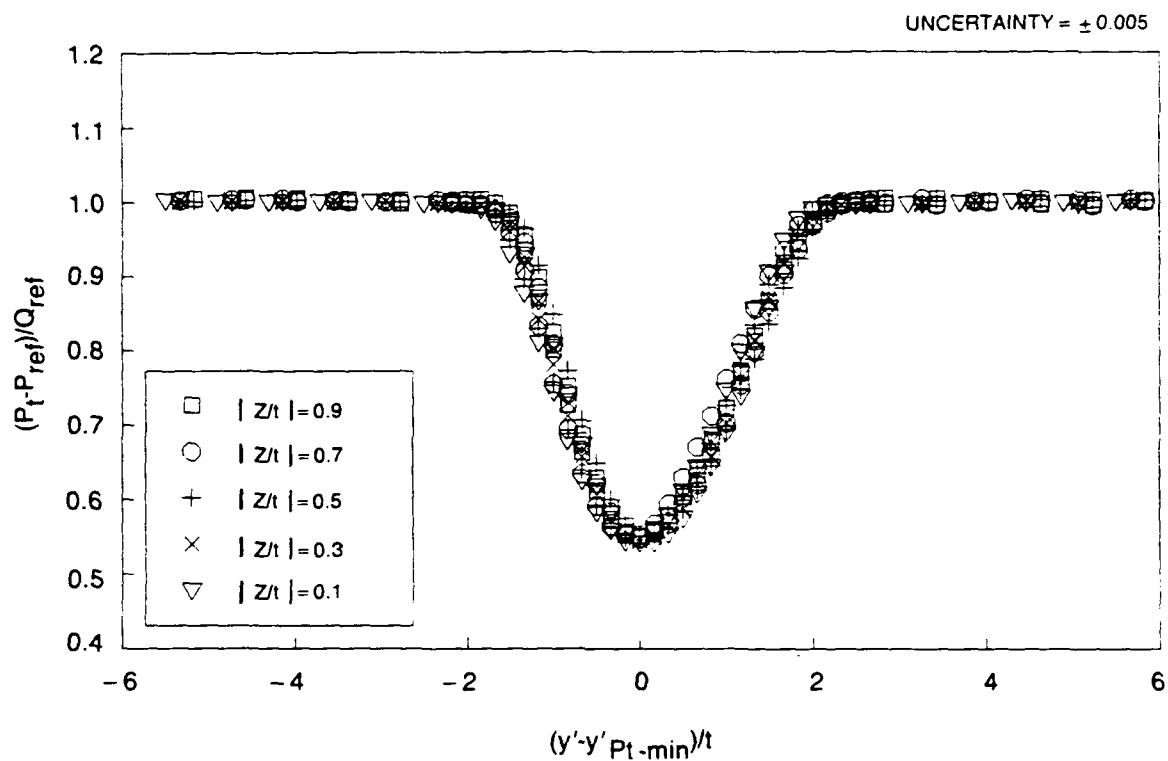


Figure 34. Total Pressure Profiles Downstream of Model 2

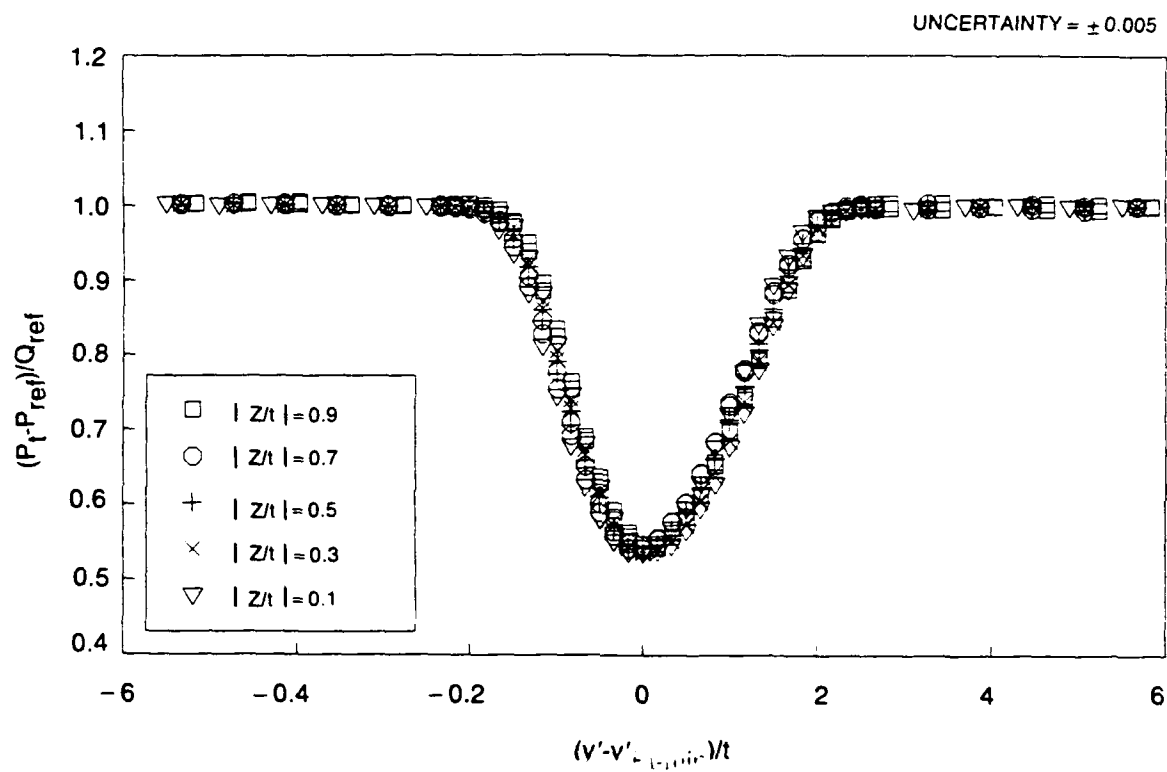


Figure 35. Total Pressure Profiles Downstream of Model 3

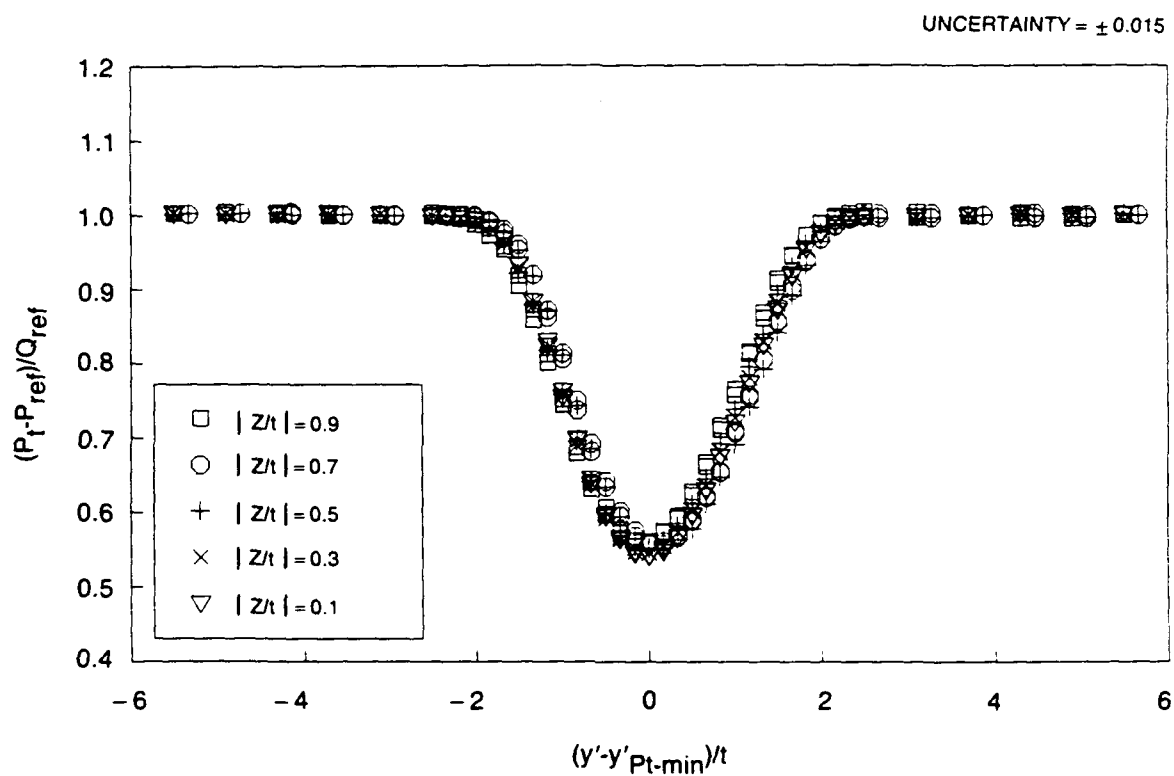


Figure 36. Total Pressure Profiles Downstream of Model 4

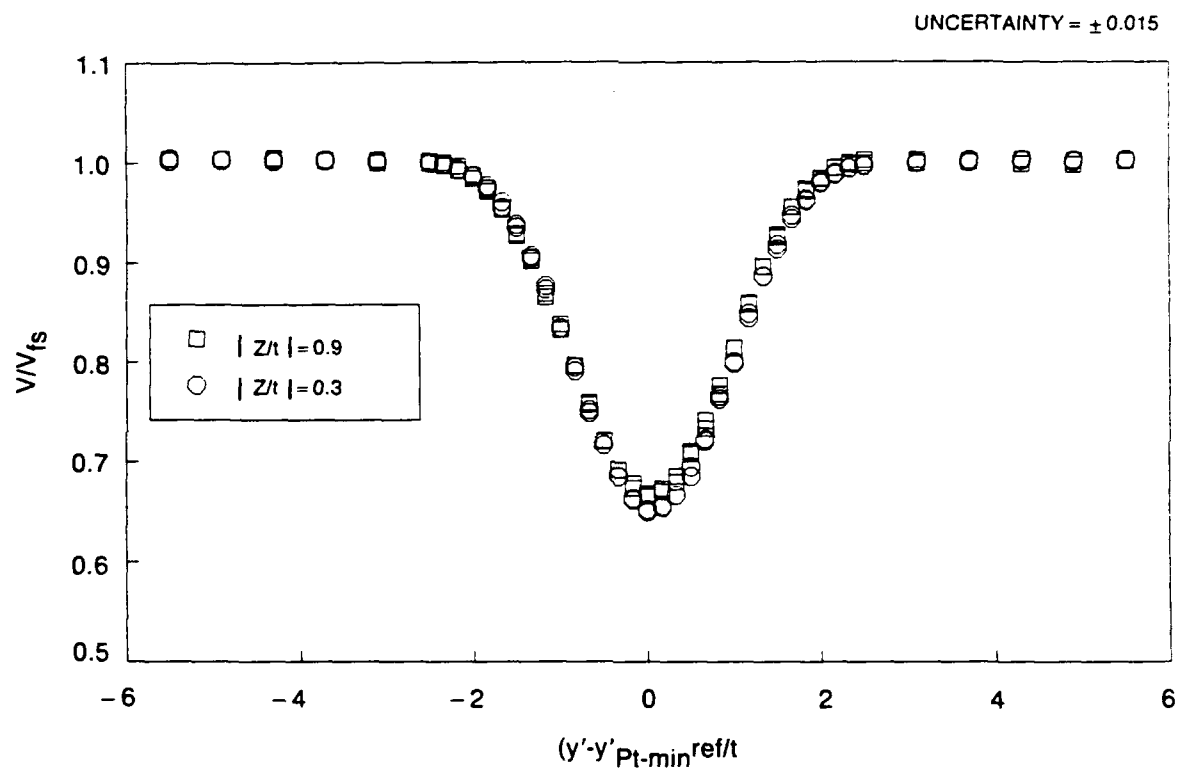


Figure 37. Velocity Profiles Downstream of Model 1

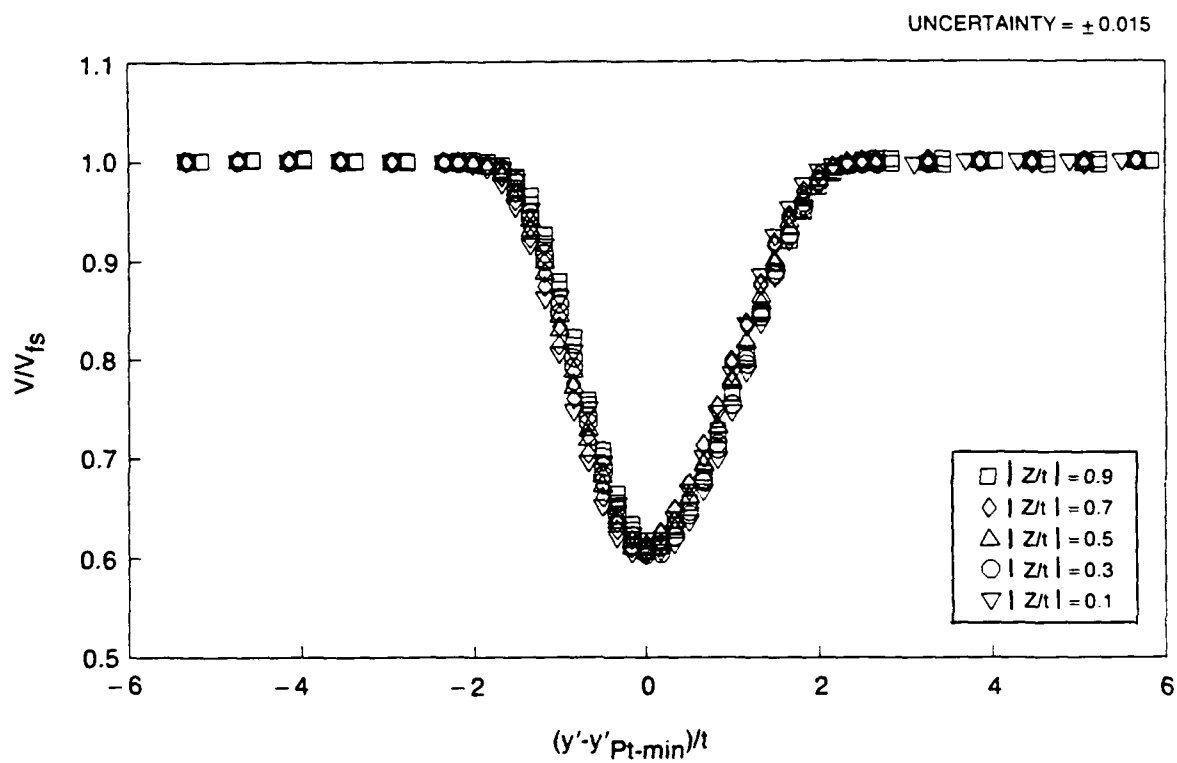


Figure 38. Velocity Profiles Downstream of Model 2

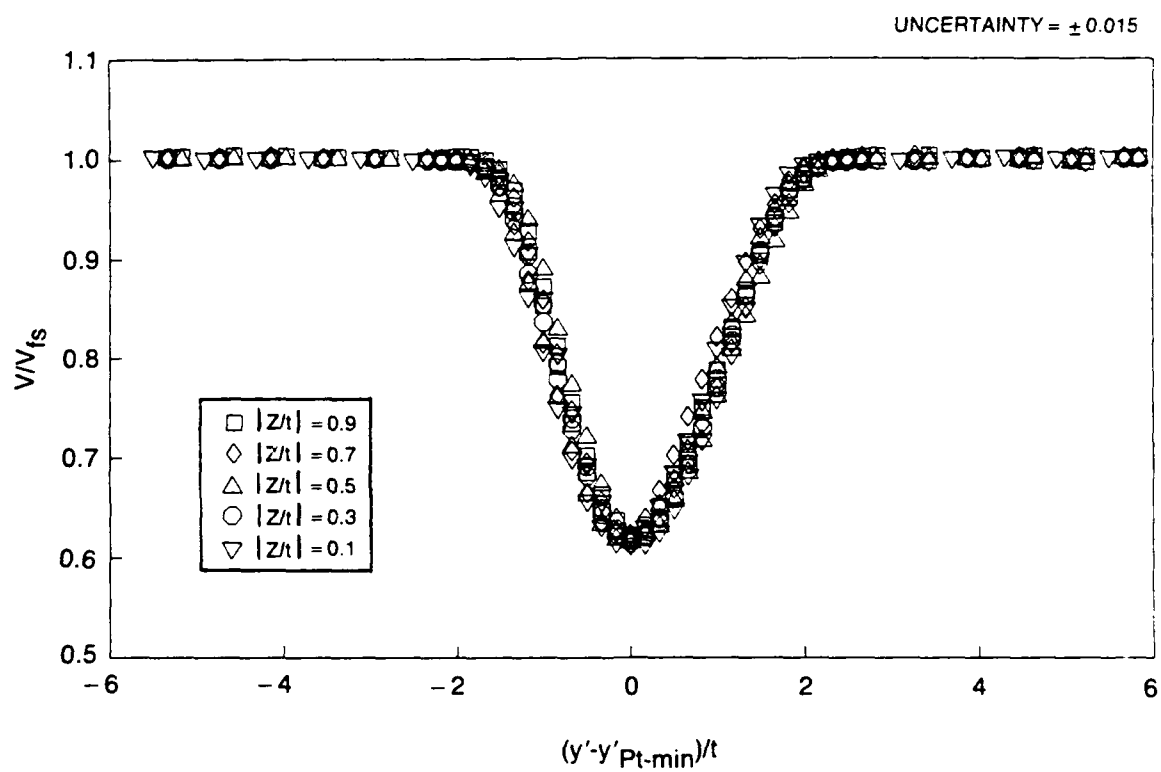


Figure 39. Velocity Profiles Downstream of Model 3

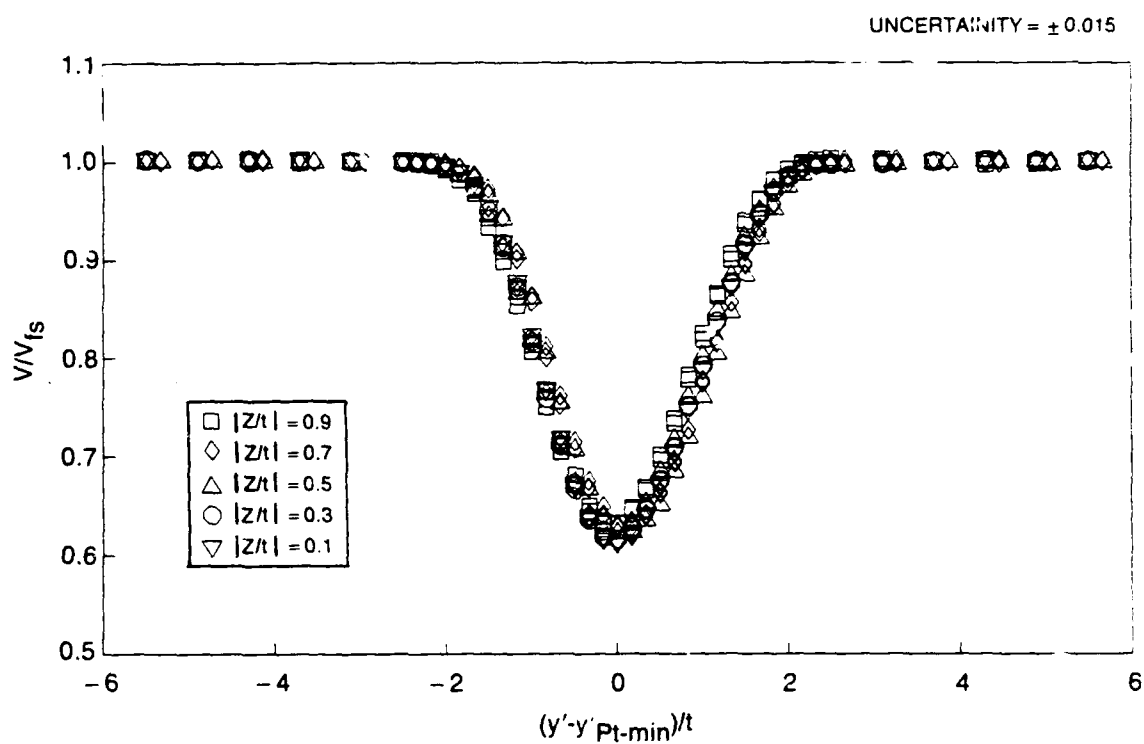


Figure 40. Velocity Profiles Downstream of Model 4

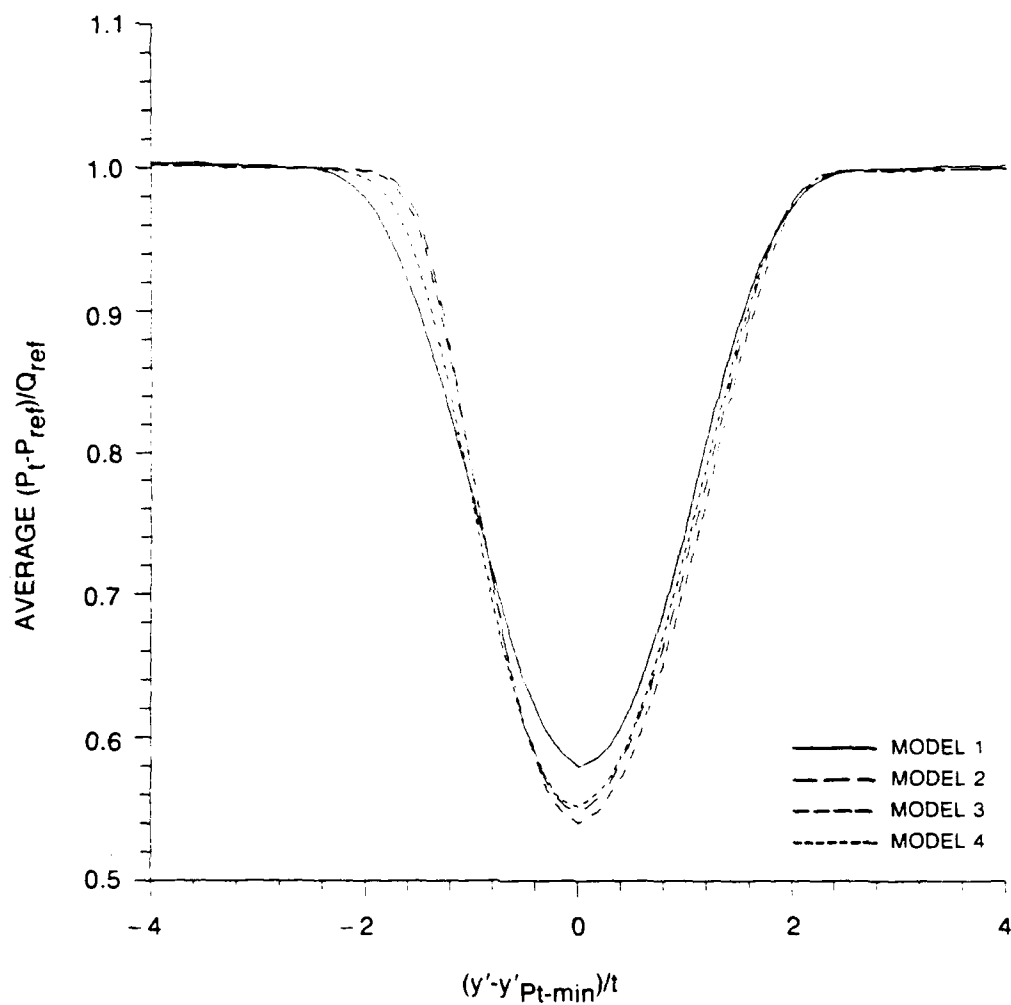


Figure 41. Average Total Pressure Profiles at $x'/t = 11.25$

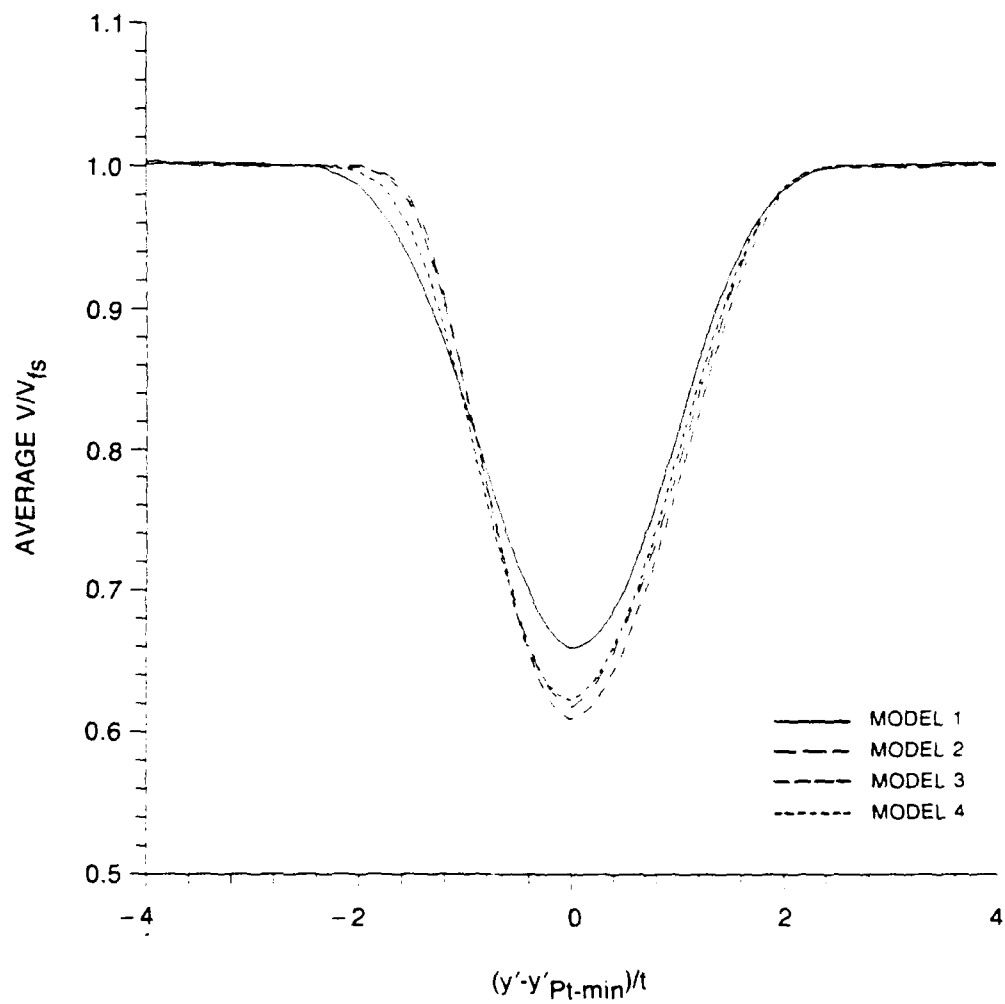


Figure 42. Average Velocity Profiles at $x'/t = 11.25$

The cascade losses up to the measurement station ($x'/t = 11.25$) were calculated from:

$$(LOSS)_{x'/t=11.25} = Q_{ref} V_{ref} \int_{y'=\delta^-}^{y'=\delta^+} \int_{z=z_{min}}^{z=z_{max}} \left(\frac{P_T - P_{Tref}}{Q_{ref}} \right) \left(\frac{V}{V_{ref}} \right) dz dy$$

where $Q_{ref} = 3.43$ cm (1.35 in.) H_2O and $V_{ref} = 24.0$ m/s (78.8 ft/s). This integrated quantity includes friction and mixing losses up to $x'/t = 11.25$. Since the profiles at this station are not uniform, the potential loss from mixing out the wake to a uniform profile must be included in the overall loss. This potential loss was accounted for by analytically mixing the measured total pressure and velocity distributions to a uniform state in a constant area control volume. The procedure is presented in Appendix A. The sum of the friction loss, mixing loss up to $x'/t = 11.25$, and potential loss beyond $x'/t = 11.25$ represents the overall cascade loss.

To determine mixing loss, the friction loss was subtracted from the overall cascade loss. The loss due to skin friction was determined by measuring the boundary layer profiles on the pressure and suction sides near the trailing edge of the baseline configuration. These profiles are presented in Figure 43. Also shown on that plot are the integral quantities calculated from the boundary layer profiles. The boundary layer characteristics are very similar to those of a CDA airfoil tested in cascade in Reference [23].

The skin friction loss was calculated from the boundary layer profiles from:

$$(LOSS)_{FRICTION} = Q_{ref} V_{ref} \int_{y'=\pm t/2}^{y'=\pm t/2 \pm \delta} (z_{max} - z_{min}) \left(\frac{P_T - P_{Tref}}{Q_{ref}} \right) \left(\frac{V}{V_{ref}} \right) dy$$

This equation assumes that there is no pressure gradient across the boundary layer and that the boundary layer is two-dimensional. Note also that this quantity includes only the skin friction loss up to the measurement station, which was taken at approximately 99% of the axial chord. The friction loss beyond the measurement station was assumed to be negligible. Also, it was assumed that the friction loss was the same for each configuration, since the pressure distributions were fairly similar, suggesting similar boundary layer characteristics. The overall cascade loss, the individual loss contributions, and the wake integral quantities are presented in Table 2 for each configuration. Skin

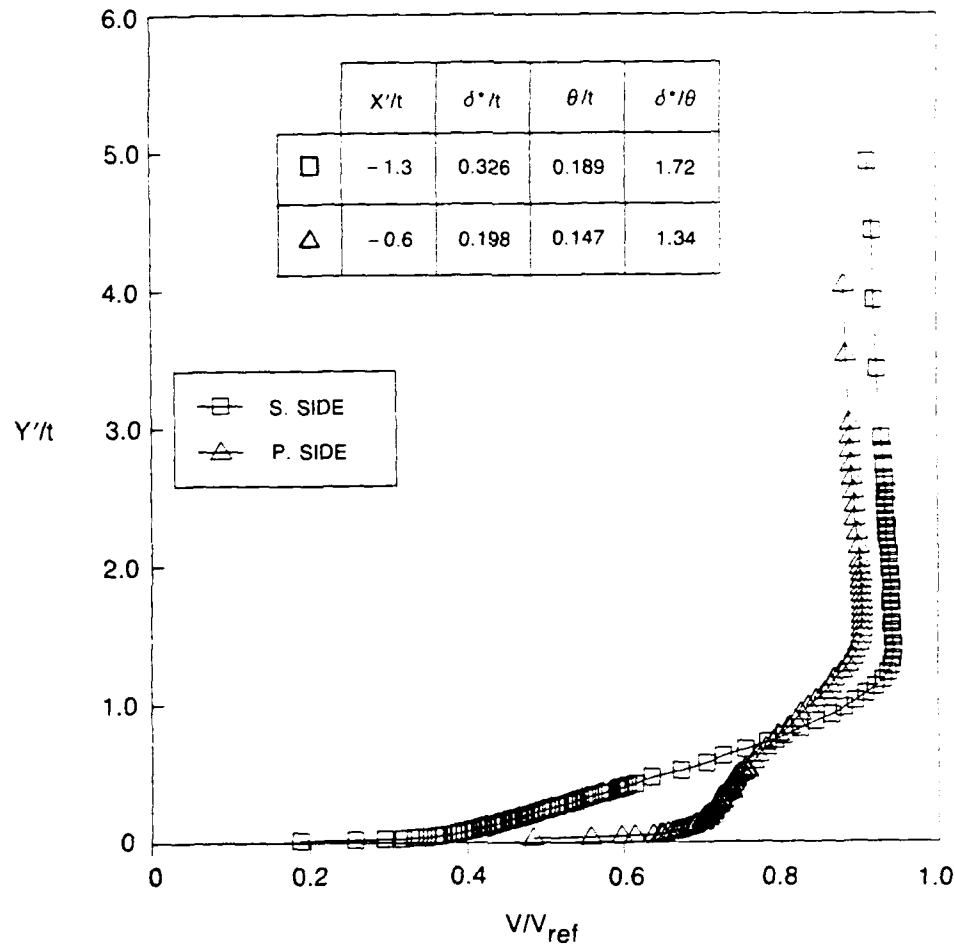


Figure 43. Boundary Layer Profiles Approaching Trailing Edge

friction was found to account for approximately 75% of the overall loss, with the remaining loss due to mixing. The best configuration was Model 2, which reduced the overall losses and mixing losses by 2% and 6%, respectively. This improvement is a direct result of increasing the base pressure and eliminating vortex shedding. It should be noted that in Reference [19], a circular trailing edge with a 23% smaller effective thickness as Model 2 had 7% less overall loss than Model 2. This result is consistent with the 1.27 cm (0.5 in.) circular trailing edge having more base pressure recovery than Model 2, as was described earlier.

TABLE 2
LOSS COMPARISON - LOW LOADING

Model	Friction Loss per Unit Span (Watts/m)	Mixing Loss per Unit Span (Watts/m)	Total Loss per Unit Span (Watts/m)	δ^*/t	θ^*/t
1	94.6	47.8	142.4	0.735	0.552
2	94.6	44.9	139.5	0.769	0.551
3	94.6	48.4	143.0	0.799	0.568
4	94.6	48.2	142.8	0.781	0.563

To observe wake development, total pressure distributions were obtained at three locations downstream of Model 1 and Model 2. Color contours of these distributions are presented in Figure 44 and 45, with violet representing the greatest loss, and red representing inviscid flow. For the purpose of comparing the two wakes, the wake width has been defined as the width of the region between the red (inviscid) contours on the pressure and suction sides of the wake.

At $x'/t = 2$, the baseline wake appears quite two-dimensional except for two perturbations on the pressure side which were attributed to longitudinal (Taylor-Gortler) vortices which develop in the boundary layer along surfaces with concave curvature (see References [24] and [25]). At this same location, Model 2 has introduced a small periodic perturbation into the baseline wake due to the inviscid pressure field set up by the convolutions. The width of the wake was not affected by the trailing edge grooves, however, the wake defect was reduced. The fact that the wake width was nearly the same for both configurations supports the previous assumption that both had similar trailing edge boundary layers. Farther downstream at $x'/t = 4.1$, the periodic perturbation is still present downstream of Model 2, and the wake defect and wake width are approximately the same for both trailing edges.

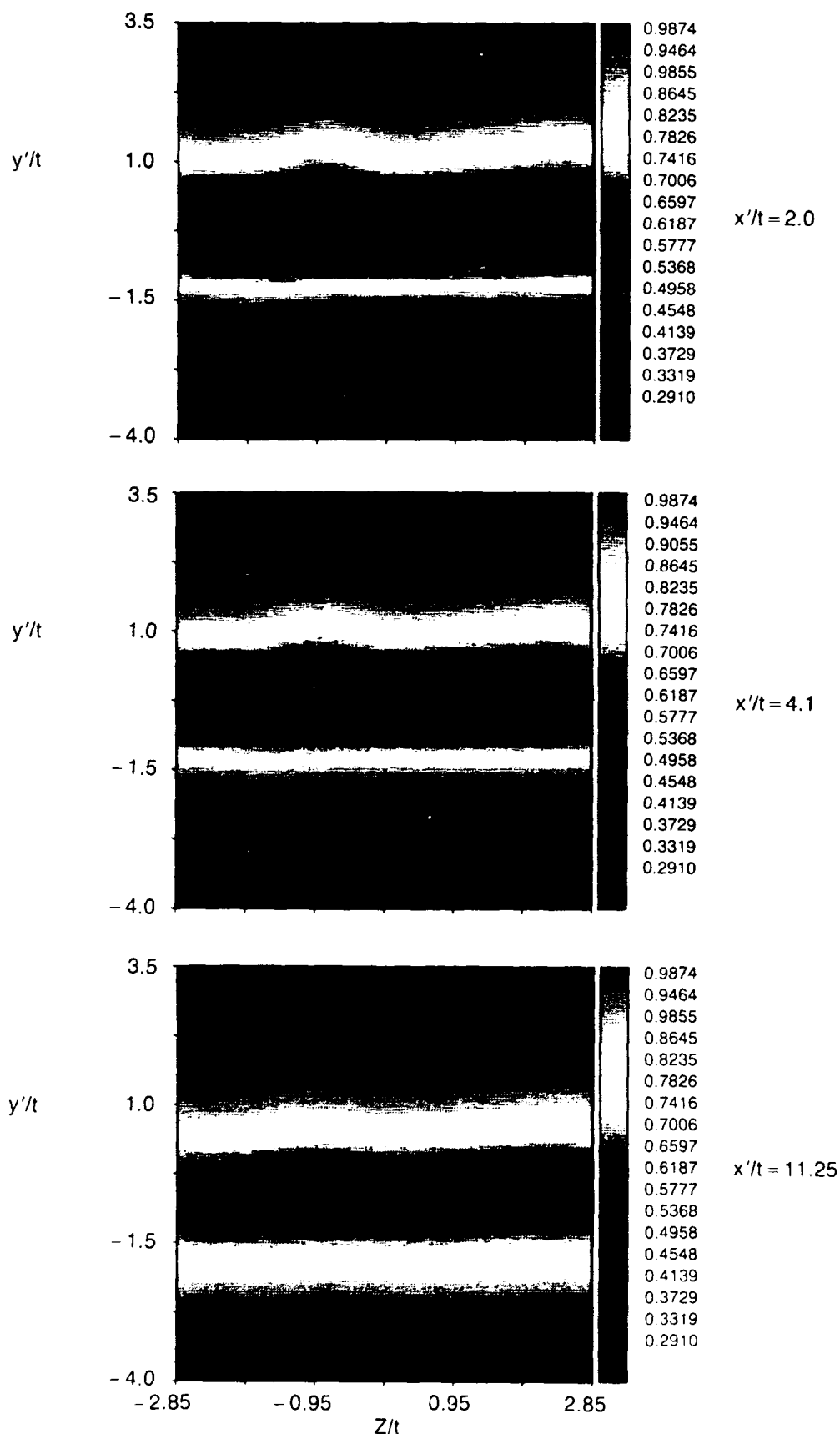


Figure 44. Total Pressure Distributions Downstream of Model 1

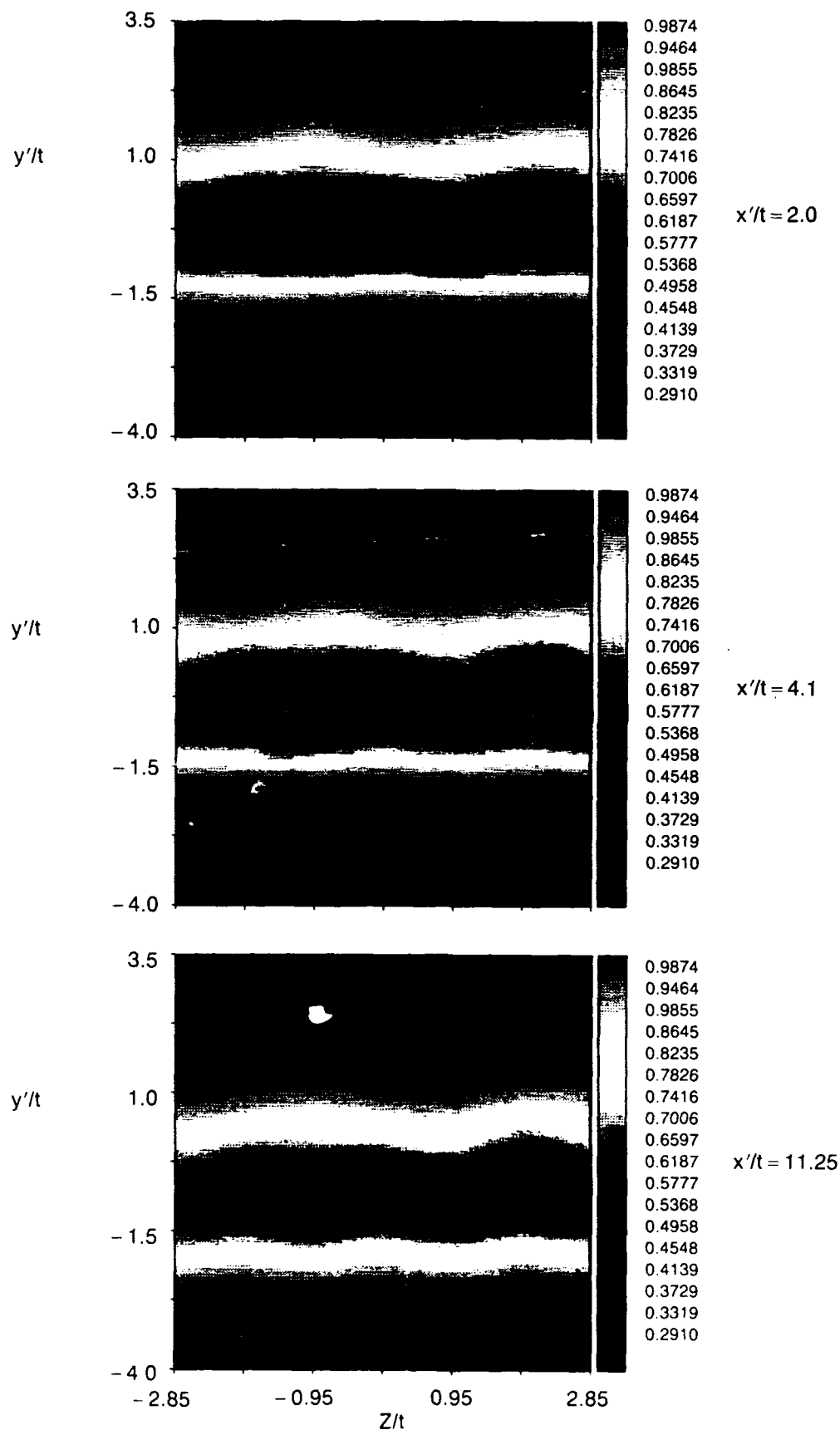


Figure 45. Total Pressure Distributions Downstream of Model 2

Finally, at $x'/t = 11.25$, the perturbations imposed by Model 2 are no longer periodic, suggesting that viscous forces are damping the inviscid pressure field set up by the grooved trailing edge. In addition, the wake defect downstream of Model 2 is greater than that in the baseline wake. However, Model 2 has reduced the wake width from 3.9 trailing edge diameters to 3.6 trailing edge diameters, with all of the reduction occurring on the suction side of the wake. The reduction in wake width offsets the increase in wake defect, resulting in Model 2 having less loss than the baseline trailing edge.

To summarize the results discussed above, Model 2 eliminated vortex shedding, resulting in a significant increase in base pressure recovery. The increase in base pressure recovery reduced the mixing loss by 6% compared to the circular trailing edge. Model 3 demonstrated a smaller increase in base pressure recovery, while Model 4 showed a decrease, though it was within the measurement uncertainty. The mixing loss changes from Models 3 and 4 were small, both being within the measurement uncertainty. Since Model 2 was the best performer, additional total pressure surveys were obtained downstream of Models 1 and 2. Those surveys showed that in the near wake of the airfoil, Model 2 had a smaller wake defect as a direct result of increasing base pressure recovery. However, in the far wake, Model 2 had a larger wake defect, indicating a slower far wake mixing rate than the circular trailing edge. This finding is shown more clearly in Figure 46 which plots $(P_{t-\min} - P_e)/Q_e$ versus x'/t . The values at $x'/t = 0$ were obtained by assuming the flow in the trailing edge region to be stagnant, with the total pressure equal to the static pressure. The rate at which $(P_{t-\min} - P_e)/Q_e$ approaches one (fully mixed) is a measure of the wake decay rate. Immediately downstream of the trailing edge, Model 2 has a smaller wake defect (i.e., a larger value of $(P_{t-\min} - P_e)/Q_e$) and a larger wake decay rate than the baseline trailing edge, but farther downstream, the baseline wake is smaller and has a larger decay rate.

Also shown in Figure 46 are results from Reference [19] for a 1.27 cm (0.5 in.) circular trailing edge tested in the same facility, with the same flow conditions and upstream model geometry as Model 2. It is interesting to note that the 1.27 cm (0.5 in.) thick trailing edge initially had a smaller wake defect than the 2.54 cm (1.0 in.) thick trailing edge, but beyond $x'/t = 2$, the wakes are essentially equal. This

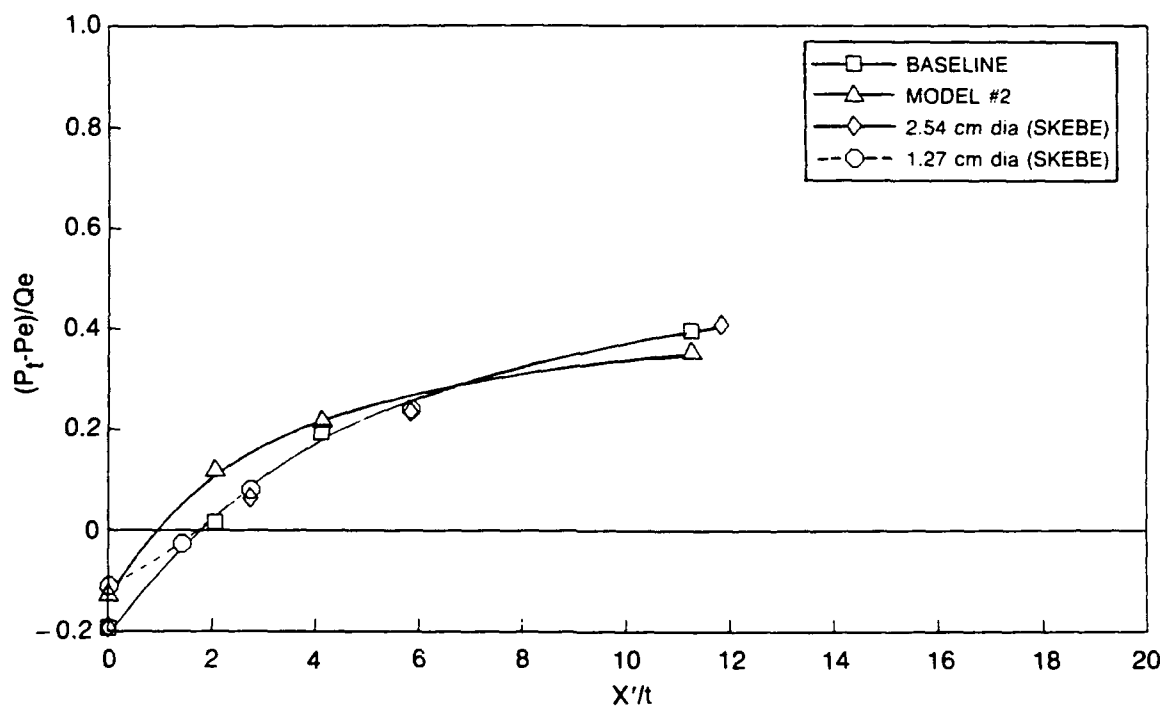


Figure 46. Comparison of Wake Decay Rates

result suggests that the far wake behavior is primarily determined by the trailing edge boundary layers rather than the trailing edge diameter.

Though Model 2 has more loss and less base pressure recovery than the 1.27 cm (0.5 in.) thick circular trailing edge, Figure 46 shows it to have a smaller wake defect up to approximately $x'/t = 7$. However, beyond $x'/t = 7$, both circular trailing edges have smaller wakes than Model 2 in addition to a faster wake decay rate. Since blade rows are typically spaced more than 10 trailing edge diameters apart, the grooved trailing edge would thus impose a larger wake defect on the subsequent blade row.

The increase in the wake defect and the slower wake mixing rate in the far wake were unexpected, since all prior work with forced mixers and convoluted surfaces showed them to generate intense mixing that extends far downstream of their trailing edge, due to the large scale vortices that they generate. These large scale vortices are developed by the inviscid pressure field set up at the trailing edge by the convolutions. In this study, it appears that the thick suction side and pressure side boundary layers relative to the groove width and depth inhibited the formation of this inviscid pressure field, thereby limiting the production and strength of the stirring vortices. Similar results are described in Reference [11] where it was shown that boundary layer buildup within the troughs of an advanced mixer lobe reduced the effective lobe amplitude and, consequently, the lobe circulation.

To further examine the effect of boundary layer thickness on wake mixing downstream of grooved trailing edges, 109 cm (43 in.) of the straight section of the model were removed to reduce the boundary layer thickness. The resultant Reynolds number based on nominal operating conditions and axial chord length was $1.1(10^6)$. The elliptical leading edge was still used with this shortened chord configuration. Boundary layer profiles, presented in Figure 47 show that removal of the straight section reduced the suction side displacement thickness and momentum thickness by 61% and 57%, respectively, and reduced the pressure side displacement thickness and momentum thickness by 76% and 78%, respectively. Since both the pressure side and suction side boundary layers were tripped near the leading edge, the velocity profiles remained turbulent, as indicated by the suction side and pressure side shape factors of 1.57 and 1.41, respectively.

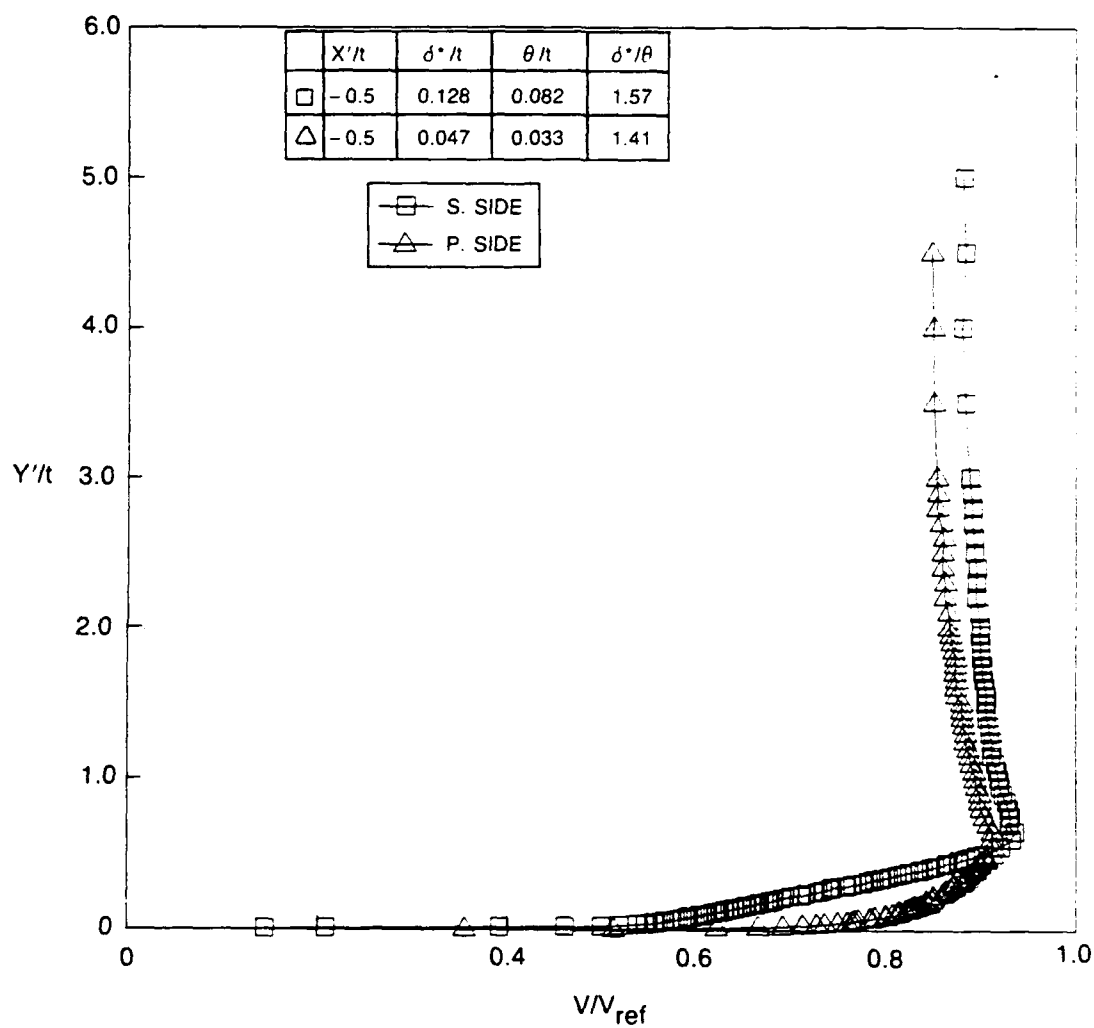


Figure 47. Boundary Layer Profiles Approaching Trailing Edge with Flat Section of Model Removed

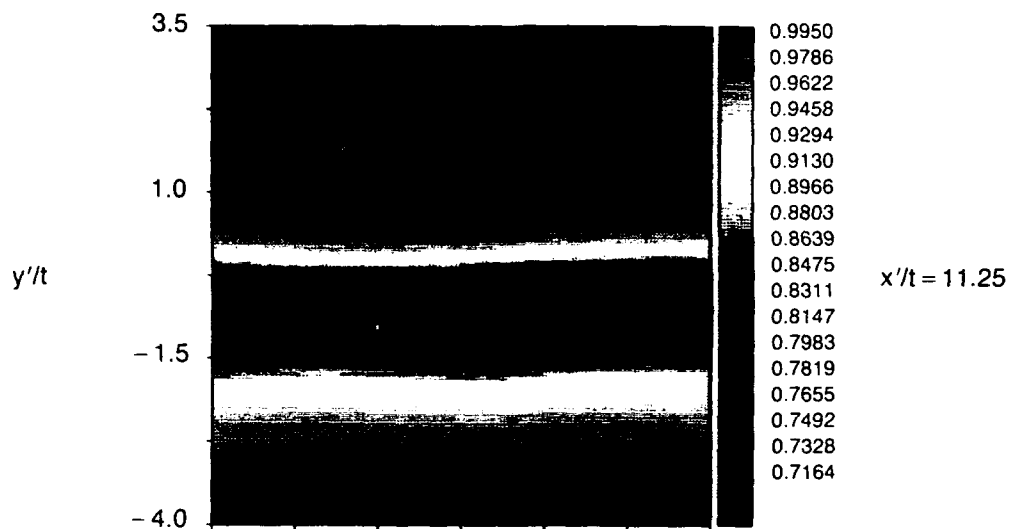
TABLE 3
LOSS COMPARISON - LOW LOADING, THIN BOUNDARY LAYER

Model	C_{pb}	Friction Loss per Unit Span (Watts/m)	Mixing Loss per Unit Span (Watts/m)	Total Loss per Unit Span (Watts/m)	δ^*/t	θ/t
1	-0.328	33.3	28.4	61.7	0.324	0.277
2	-0.155	33.3	24.1	57.4	0.308	0.263
5	-	33.3	27.1	60.4	0.322	0.277

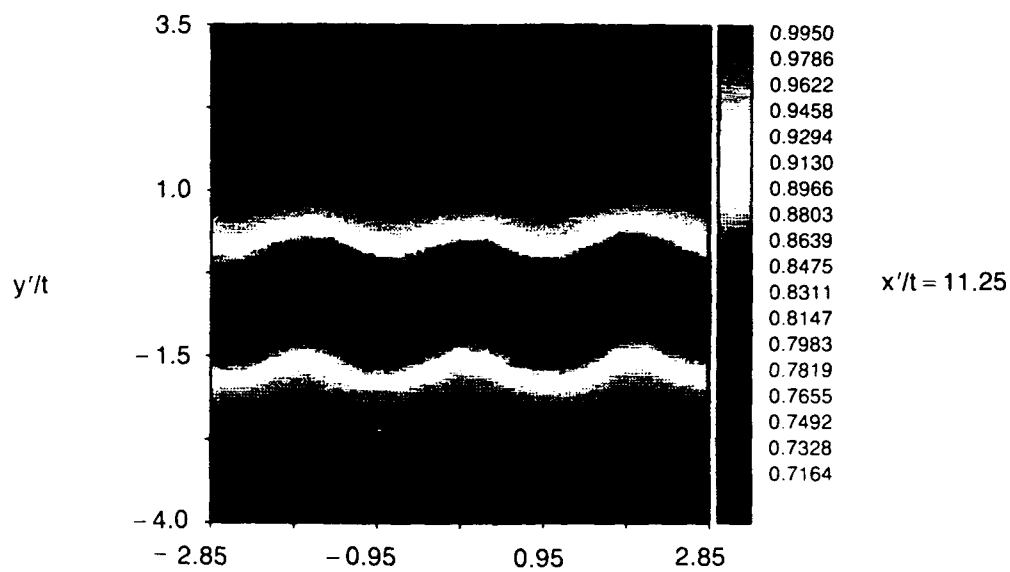
Base pressure coefficients, cascade losses, and wake integral quantities are presented in Table 3 for the thin boundary layer configuration. Results are presented for Model 1, Model 2 (which performed the best with the thicker boundary layer), and Model 5 which was not previously tested. Model 5 was not instrumented and therefore, a base pressure coefficient could not be determined. Relative to the previously described thick boundary layer configuration, the base pressure coefficients and losses were reduced. In addition, the contribution of skin friction to the overall cascade loss dropped from 75% to 54%.

With the thinner boundary layer, grooving the trailing edge had significantly more benefit in terms of increased base pressure recovery and reduced mixing losses. With the thinner boundary layer, Model 2 increased C_{pb} from -0.328 to -0.155 compared to -0.193 to -0.134 for the thick boundary layer. Likewise, the mixing losses were reduced by 15% with the thin boundary layer compared to 6% with the thick boundary layer. Model 5 was found to be less effective than Model 2, reducing the mixing loss by only 5%.

Color contours of the total pressure distributions at $x'/t = 11.25$, downstream of Models 1 and 2, are presented in Figure 48. Once again, violet represents the highest loss region, while inviscid flow is red. In this configuration, the wake defect of each trailing edge is approximately equal at $x'/t = 11.25$. In addition, Model 2 reduced the wake width from 3.4 to 2.8 trailing edge diameters, with the entire reduction occurring on the suction side of the wake. A similar, though less pronounced, result was observed with the thicker boundary layer. Also, the perturbation on the wake is more periodic compared to that with the thicker boundary layer (Figure 45). This result supports the previous claim that the thick trailing edge boundary layers described earlier damped out the inviscid pressure field that



a) BASELINE



b) MODEL 2

Figure 48. Downstream Total Pressure Distributions — Thin Boundary Layer

is set up by the trailing edge convolutions. Note, however, that even with the thinner boundary layer, the large scale structures which are usually evident downstream of mixers still are not observed. It is furthermore shown in Figure 49 that the trends in the wake decay rate observed with the thin boundary layer is consistent with that observed with the thicker boundary layer (i.e., the effect of the grooves is felt mainly near the trailing edge).

To summarize the low loading results, grooving the trailing edge of a simulated compressor airfoil, with loading conditions and boundary layer characteristics typical of on-design operation, increased base pressure recovery and eliminated vortex shedding. The elimination of vortex shedding was attributed to the breakup of the trailing edge coherence and the reduction of the base area. As a result of the increased base pressure recovery, mixing loss was reduced by 6%, and overall loss was reduced by 2%. Wake surveys showed that between $x'/t = 0$ and $x'/t = 7$, the grooved trailing edge had a smaller wake defect than the baseline trailing edge; however, beyond $x'/t = 7$, the mixing rate slowed, resulting in the grooved trailing edge having a larger wake defect, though smaller wake width. With much thinner (and less realistic) boundary layers, the grooved trailing edge's wake defect was smaller than the baseline's wake defect to beyond $x'/t = 11.25$. In addition, with the thinner boundary layer, the grooved trailing edge reduced mixing loss by 15% and overall loss by 6%. This dependence on boundary layer thickness suggests that the ratio of the boundary layer characteristics (δ^* and θ) to the groove depth and height plays an important role in the development of the inviscid pressure field that generates the stirring vortices downstream of convoluted surfaces. This result is consistent with findings in Reference [11].

When compared to a circular trailing edge with 23% less effective base area as the grooved trailing edge, the grooved trailing edge had less base pressure recovery and more loss. The grooved trailing edge had a smaller wake defect out to $x'/t = 7$, but had a larger wake defect effect farther downstream. In the far wake, both the 1.27 cm (0.5 in.) and 2.54 cm (1.0 in.) diameter circular trailing edges demonstrated the same wake behavior.

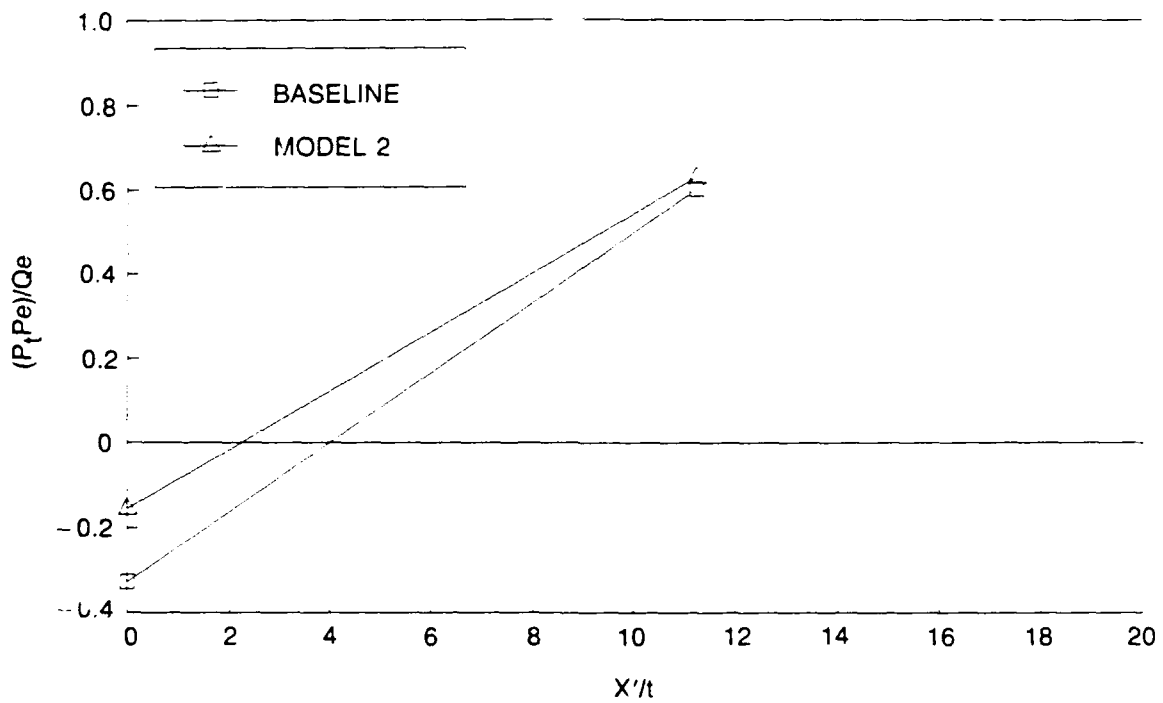


Figure 49. Comparison of Wake Decay Rates — Thin Boundary Layer

SUMMARY OF RESULTS

1. Under a high loading condition, typical of off-design compressor operation, a baseline circular trailing edge demonstrated flow separation approximately four trailing edge diameters upstream of the trailing edge. Under a low loading condition, typical of on-design compressor operation, a baseline circular trailing edge demonstrated flow separation only at the trailing edge circle.
2. The original RTE design, at the high loading condition, resulted in approximately a 50% increase in the chordwise extent of the separated flow observed on the baseline trailing edge. This increase was attributed to the 10 degree increase in turning in the suction side trough ($\alpha_s = 10$ degrees), and insufficient three-dimensional boundary layer relief.
3. Even though the original RTE was more grossly separated, it required significantly less endwall suction to obtain two-dimensional flow over 80% of the tunnel span compared to 35% of the tunnel span for the baseline trailing edge. This effect was attributed to the ripples breaking up the continuous trailing edge separation into isolated stall cells, thereby reducing the tendency of the sidewall boundary layers to migrate toward the low pressure region created by the separation.
4. A modified RTE (RTE 2) with converging suction side lobes, and with $\alpha_s = 0$ degrees, eliminated the large scale separation that was present with both the circular trailing edge and the original RTE.
5. The modified RTE (RTE 2) showed a small "apparent" loading reduction compared to the baseline circular trailing edge, even though RTE 2 was unseparated. This result was attributed to a combination of modifying only five lobes, and a possible increase in wake convection angle due to the three-dimensional contouring of the trailing edge. This "apparent" loading reduction is not necessarily indicative of what would occur in a two-dimensional cascade of multiple RTE airfoils.
6. For the low loading condition, grooving the circular trailing edge increased base pressure recovery (which varied inversely with groove depth), and eliminated vortex shedding. As a result, with realistic compressor trailing edge boundary layer characteristics, mixing loss was reduced by 6% and

overall loss was reduced by 2% compared to the baseline trailing edge. With thinner, less realistic boundary layers, the grooved trailing edge reduced mixing loss by 15% and overall loss 6%.

7. For the configuration with realistic boundary layers, the grooved trailing edge had a smaller wake defect out to seven trailing edge diameters from the trailing edge. Beyond that, the mixing rate slowed, and the baseline trailing had a smaller wake defect. For the thinner boundary layer configuration, the grooved trailing edge had a smaller wake defect out to 11.25 trailing edge diameters from the trailing edge. This dependence on boundary layer thickness suggests that the ratio of the boundary layer characteristics (δ^* and θ) to the groove depth and height plays an important role in the development of the inviscid pressure field that generates the stirring vortices which help to mix out the wake. This result agrees with results in Reference [11].
8. When compared to a circular trailing edge tested in Reference [19] with 23% less effective base area as the grooved trailing edge, the grooved trailing edge had less base pressure recovery and more loss. However, the grooved trailing edge had a smaller wake defect out to $x'/t = 7$. In the far wake, both the 1.27 cm (0.5 in.) diameter trailing edge tested in Reference [19] and the 2.54 cm (1.0 in.) diameter trailing edge tested in the present study had the same wake behavior.
9. An analytical treatment of rippled surface geometries requires a zonal analysis approach, wherein the salient surface features can be locally modeled without resorting to either computationally intensive calculations or approximate calculations that incorrectly model the problem.

CONCLUDING REMARKS

A research program was conducted to assess the potential benefits of using the Rippled Trailing Edge (RTE) concept on compressor airfoils for separation alleviation and wake mixing enhancement. A large scale cascade simulation was performed on a simulated compressor airfoil under two loading conditions; a high loading condition typical of off-design operation and a low loading condition typical of on-design operation. Both loading conditions were tested with a baseline circular trailing edge, and with various rippled trailing edges.

Results from the high loading study showed that the original RTE design increased the chordwise extent of the separation by 50% compared to the circular trailing edge. Modifications performed to the RTE to increase three-dimensional boundary layer relief resulted in a trailing edge that eliminated separation. The effect on airfoil loading could not be evaluated since the cascade facility employed did not exactly simulate a two-dimensional periodic, compressor cascade.

From the experimental results, it is concluded that the RTE concept has potential for separation alleviation on highly loaded compressor airfoils. However, the failure of the first design shows that many unknowns still exist regarding the three-dimensional boundary layer relief concept, and that non-optimal geometries can adversely affect separation. Further testing of ripples on more basic, isolated airfoils is suggested in order to develop further understanding of the three-dimensional boundary layer relief mechanism, without having to consider the inherent problems associated with the cascade testing described herein. After developing such a data base, Rippled Trailing Edges can then be evaluated for application to the more complex case of a cascade where curvature and three-dimensional effects are significant.

Results from the low loading study showed that grooving a simulated circular compressor trailing edge increased base pressure recovery and eliminated vortex shedding. As a result, mixing loss was reduced by 6%, and overall loss was reduced by 2%. However, beyond seven trailing edge diameters downstream of the airfoil, the grooved trailing edge had a larger wake defect, through smaller wake width, than the baseline trailing edge. Since blade rows are typically spaced more than 10 trailing edge diameters apart, the grooved trailing edge would thus impose a larger wake defect on the subsequent

blade row. It is concluded that for compressor applications, grooving the trailing edge of a circular airfoil is not an effective method of reducing trailing edge loss, since it imposes a larger wake defect on the subsequent blade row. For thinner boundary layer applications, a *grooved trailing edge* did show enhanced wake mixing, with a reduced wake defect beyond 11 trailing edge diameters downstream of the airfoil.

RECOMMENDATIONS

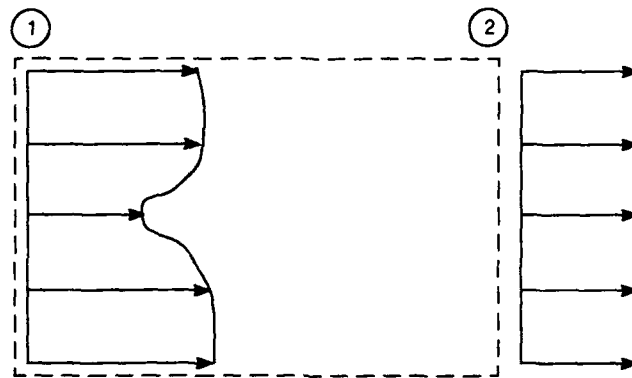
The results of this study show that the RTE concept has potential for separation alleviation on highly loaded compressor airfoils. However, the cascade simulation that was employed was not truly two-dimensional, and thus could not provide airfoil loading information. In addition, the effect of the RTE on airfoil performance at design point operation is still unknown. Further testing of ripples on more basic, isolated airfoils is suggested in order to develop further understanding of the three-dimensional boundary layer relief concept, without having to consider the inherent problems associated with cascade testing as described in this report. After developing such a data base (including the effect of the RTE on unseparated airfoil performance), Rippled Trailing Edges can then be evaluated for application to the more complex case of a cascade where curvature and three-dimensional effects are significant.

REFERENCES

- [1] Hobbs, D.E., and Weingold, H.D., "Development of Controlled Diffusions Airfoils for Multi-stage Compressor Application," *ASME Journal of Engineering for Gas Turbines and Power*, Vol. 106, No. 4, 1984, pp. 271-278.
- [2] McCormick, D.C., Paterson, R.W., and Weingold, H.D., "Experimental Investigation of Loading Effects on Simulated Compressor Airfoil Trailing Edge Flowfields," AIAA Paper 88-0365, January 1988.
- [3] McCormick, D.C., Paterson, R.W., and Weingold, H.D., "Experimental Investigation of Loading Effects on Simulated Compressor Airfoil Trailing Edge Flowfields," UTRC Report 87-14, United Technologies Research Center, May 1987.
- [4] Paterson, R.W., and Weingold, H.D., "Experimental Investigation of a Simulated Compressor Trailing Edge Flowfield," *ALAA Journal*, Vol. 21, No. 5, 1985, pp. 768-775.
- [5] Taylor, H.D., *Summary Report on Vortex Generators*, United Aircraft Research Report on Vortex Generators, R-05280-9, March 1950.
- [6] Grose, R.M., "Theoretical and Experimental Investigations of Various Types of Vortex Generators," United Aircraft Corp., East Hartford, CT, Research Rept. R15362-5, 1954.
- [7] Kimball, S., "Vortex Generators," *Road and Track*, Vol. 36, No. 1, 1985, pp. 122-124.
- [8] Shubauer, G.B., and Spangenberg, W.G., "Forced Mixing in Boundary Layers," *Journal of Fluid Mechanics*, Vol. 8, No. 5, 1960, pp. 10-32.
- [9] Werle, M.J., Paterson, R.W., and Presz, W.M., "Trailing Edge Separation/Stall Alleviation," *ALAA Journal*, Vol. 25, No. 4, 1987, pp. 624-626.
- [10] Paterson, R.W., "Turbofan Mixer Nozzle Flow Field - A Benchmark Experimental Study," *Transactions of the ASME*, Vol. 106, No. 7, 1984, pp. 692-698.
- [11] Skebe, S.A., Paterson, R.W., and Barber, T.J., "Experimental Investigation of Three-Dimensional Forced Mixer Lobe Flow Fields," AIAA Paper 83-3785, 1988.
- [12] Blair, M.F., Bailey, D.A., and Schlinker, R.H., "Development of a Large-Scale Wind Tunnel for the Simulation of Turbomachinery Airfoil Boundary Layers," *Trans. ASME, Journal of Engr. for Power*, Vol. 103, No. 10, 1981, pp. 678-687.
- [13] Hama, F.R., "An Efficient Tripping Device," *Journal of the Aeronautical Sciences*, Vol. 24, No. 3, 1957, pp. 236-237.

- [14] Andorn, J.D., "Aerodynamic Considerations of an Advanced Sports Car," Western New England College Senior Project Report, May 1984.
- [15] Croteau, P., "Investigation Into the Use of a Rippled Trailing Edge Airfoil to Improve Airfoil Characteristics," Western New England College Senior Project Report, May 1985.
- [16] Presz, W.M., Morin, B.L., and Gousy, R.G., "Forced Mixer Lobes in Ejector Designs," *Journal of Propulsion and Power*, Vol. 4, No. 4, 1988.
- [17] Presz, W.M., Morin, B.L., and Blinn, R.F., "Short Efficient Ejector Systems," AIAA Paper 87-1837, July 1987.
- [18] Presz, W.M., Russell, W.D., and Tongue, S.E., "Rippled Afterbody Performance Study," UTRC Report 87-27, United Technologies Research Center, September 1987.
- [19] Skebe, S.A., and Patrick, W.P., "An Investigation of Advanced Compressor Trailing Edge Shapes," UTRC Report 89-17, United Technologies Research Center, May 1989.
- [20] Maskew, B., "Prediction of Subsonic Aerodynamic Characteristics: A Case for Low-Order Panel Methods," *Journal of Aircraft*, Vol. 19, No. 2, 1982, pp. 157-163.
- [21] Clark, D.R., Maskew, B., and Dvorak, F.A., "The Application of a Second Generation Low-Order Panel Method-Program VSAERO to Powerplant Installations," AIAA 84-0122, AIAA 22nd Aerospace Sciences Meeting, January 1984.
- [22] Tanner, M., "New Investigations for Reducing the Base Drag of Wings with a Blunt Trailing Edge," AGARD Paper No. 134, *Proceedings of the Conference on 'Aerodynamic Drag'*.
- [23] Hobbs, D.E., Wagner, J.H., Dannenhoffer, J.F., and Dring, R.P., "Experimental Investigation of Compressor Cascade Wakes," ASME 83-GT-299, 1982.
- [24] Hoffman, P.H., Muck, K.C., and Bradshaw, P., "The Effect of Concave Surface Curvature on Turbulent Boundary Layers," *Journal of Fluid Mechanics*, Vol. 161, pp. 371-403, 1985.
- [25] Meroney, R.N., and Bradshaw, P., "Turbulent Boundary-Layer Growth Over a Longitudinally Curved Surface," *AIAA Journal*, Vol. 13, No. 11, 1975.

APPENDIX A



89-6-22-33

Constant area: $A_1 = A_2 = A$

Incompressible: $\rho_1 = \rho_2 = \rho$

let overbar denote area average

Conservation of mass:

$$\int V_1 dA = \int V_2 dA$$

$$V_2 = \frac{1}{A} \int V_1 dA$$

$$V_2 = \bar{V}_1$$

Conservation of momentum (axial):

$$\int (P_1 + \rho V_1^2) dA = \int (P_2 + \rho V_2^2) dA$$

$$P_1 A + \int \rho V_1^2 dA = P_2 A + \rho V_2^2 A$$

$$(P_2 - P_1) A = \int \rho V_1^2 dA - \rho (\bar{V}_1)^2 A$$

$$(P_2 - P_1) A = \int \rho (V_1^2 - (\bar{V}_1)^2) dA$$

$$P_2 A = P_1 A + \int \rho (V_1^2 - (\bar{V}_1)^2) dA$$

$$P_2 A = P_1 A + \rho (\bar{V}_1^2) A - \rho (\bar{V}_1)^2 A$$

$$P_2 = P_1 + \rho (\bar{V}_1^2) - \rho (\bar{V}_1)^2$$

$$P_{T2} = P_2 + \frac{1}{2} \rho V_2^2$$

$$= P_2 + \frac{1}{2} \rho (\bar{V}_1)^2$$

$$P_{T2} = P_1 + \rho (\bar{V}_1^2) - \frac{1}{2} \rho (\bar{V}_1)^2 \quad \text{uniform}$$

$$P_{T1} = P_1 + \frac{1}{2} \rho V_1^2 \quad \text{nonuniform}$$

$$P_{T2} - P_{T1} = \rho (\bar{V}_1^2) - \frac{1}{2} \rho (\bar{V}_1)^2 - \frac{1}{2} \rho V_1^2$$

$$\text{Loss} = \int (P_{T2} - P_{T1}) V_1 dA$$

$$\text{Loss} = \rho (\bar{V}_1^2) \bar{V}_1 A - \frac{1}{2} \rho (\bar{V}_1)^3 A - \frac{1}{2} \rho (\bar{V}_1^3) A$$